PERMEABILITY CHARACTERIZATION AND MICROVOID PREDICTION DURING IMPREGNATION OF FIBER TOWS IN DUAL-SCALE FABRICS

by

Nina (Kuentzer) Barnett

A thesis submitted to the Faculty of the University of Delaware in partial fulfillment of the requirements for the degree of Master of Science in Mechanical Engineering.

Fall 2005

UMI Number: 1430754

UMI®

PERMEABILITY CHARACTERIZATION AND MICROVOID PREDICTION DURING IMPREGNATION OF FIBER TOWS IN DUAL-SCALE FABRICS

by

Nina (Kuentzer) Barnett

Approved: _____
Suresh G. Advani, Ph.D.
Professor in charge of thesis on behalf of the Advisory Committee

Approved: _____
Thomas S. Buchanan, Ph.D.
Chair, Department of Mechanical Engineering

Approved: _____
Eric W. Kaler, Ph.D.
Dean, College of Engineering

Approved: _____
Conrado M. Gempesaw II, Ph.D.
Vice Provost for Academic and International Programs

ACKNOWLEDGMENTS

TABLE OF CONTENTS

LIST OF TABLES

LIST OF FIGURES

ix

x

NOMENCLATURE

Symbol	Description	Units
∇	Gradient	
$\nabla\bullet$	Divergence	
δ	Partial derivative	
ϕ	Fabric porosity ($1-V_f$)	%
μ	Fluid viscosity	Pa s
π	Pi (3.14)	
A	Cross-sectional area of mold	m^2
A^{tow}	1D element default cross-section ($h = l/2$)	m^2
$A^{tow-adj.}$	1D element adjusted cross-section	m^2
d	Ordinary derivative	
dx	Length of elemental volume in mass balance	m
$\bar{\bar{K}}$	Fabric permeability tensor	m^2
K	Scalar fabric permeability	m^2
K_{bulk}	Permeability of macro regions between fiber tows	m^2
K_{tow}	Permeability of micro regions within fiber tows	m^2
K_{tow}/h^2	Fiber tow permeability fitting parameter	1
K_{DM}	Permeability of distribution media	m^2
K_{flow}	Permeability in flow direction	m^2
K_{micro}	Permeability of micro regions within fiber tows	m^2
K_{trans}	Permeability in direction transverse to flow	m^2

K_{vent}	Permeability of resistance tubing	m^2
K^*	Permeability ratio ($K_{bulk} / [K_{tow} / h^2]$)	m^2
K^{**}	Non-dimensional permeability ratio (K_{tow} / K_{bulk})	1
$\hat{K}$	Non-dimensional resistance ratio (K_{vent} / K_{bulk})	1
l	1D element length	m
l_{flow}	Length of 2D element	m
l_{trans}	Thickness of 2D element	m
L_{flow}	Length of panel	m
L_{trans}	Thickness of panel	m
Ls	Partially-saturated length	m
m	Slope of pressure plot as a function of time	psi/s
p	Fluid pressure	psi
p^{num}	Pressure data points generated by LIMS	psi
p^{exp}	Pressure data points experimentally collected	psi
$\bar{Q}$	Fluid flow rate vector	cc/min
Q	Fluid flow rate	cc/min
R	Radius of resistance tubing	m
s	Degree of saturation of fiber tows	%
t_{exp}	Experimental data time step	s
t_f	Time macro flow takes to reach end of fabric	s
t_{macro}	Time needed for last 2D element of bulk preform to fill	s
t_{micro}	Time needed for last 1D tow element to fill	s
t^*	Non-dimensional time ratio (t_{micro} / t_{macro})	1

$t*_{baseline}$	Non-dimensional time ratio for baseline K_{tow} (t_{micro}/t_{macro})	1
$\hat{t}$	Normalized non-dimensional time ratio ($t*/t*_{baseline}$)	1
$\langle \overline{v}_d \rangle$	Darcy fluid velocity vector	m/s
$\langle v_d \rangle$	1D Darcy fluid velocity	m/s
v_{ff}	1D flow front fluid velocity	m/s
V^{bulk}	2D element volume	m^3
V_f^{bulk}	Volume fraction of fiber tows in mold	%
V_f^{tow}	Volume fraction of fibers in fiber tow	%
$V_f^{tows\ in\ EV}$	Volume fraction of fiber tows in elemental volume	%
x	Initial position on which mass balance is performed	m

ABSTRACT

Accurate characterization of the permeability of fabrics used as reinforcement materials in liquid composite molding (LCM) processes is necessary to realistically model the flow through these porous preforms. When dual-scale preforms are employed, not just the macro permeability values are of interest; the micro-scale permeability of the fiber tows inherent to the fabric must additionally be determined. These permeability values can then be used in LCM simulations in which standard two- or three-dimensional (2D or 3D) mesh elements are combined with one-dimensional (1D) elements. The 1D elements are attached at each node and represent the fiber tows in preforms that exhibit dual scale porosity. This implementation allows for the interactions between the macro and micro flow, and can predict the saturation of the fiber tows, along with the movement of the macroscopic resin flow front. Consequently, the time it will take to fill the mold and saturate all regions can be accurately predicted and any void formation sites can be forecasted.

A methodology is proposed, which can determine the macro permeability along with a simulation fitting parameter that is closely associated to the micro permeability. The inlet pressure profile of a single 1D constant flow rate resin transfer molding (RTM) experiment is evaluated experimentally and numerically in order to determine the two values. The methodology is validated analytically and in a simulation environment to demonstrate the versatility and limitations, and to reinforce the trends and tendencies. Characterizations for four different fabrics are performed.

Additionally, the percentage and distribution of voids in a composite are evaluated. The voids are usually a function of the fiber preform architecture, the infusion scheme, and the processing method, in addition to the inherent variations in the preform and the hand lay-up technique. For preforms that are woven or stitched, the fiber tows have a much lower permeability as compared to the permeability between the fiber tows. For this reason, processing methodology has converged on letting the resin bleed out of the vent to allow sufficient time for the low permeability fiber tows to fully saturate. The impact of this processing methodology is explored, along with an alternative process in which flow resistance is added. The influence of these modifications is characterized in terms of void content in the composite. Samples are machined from each of the manufactured panels and analyzed using image analysis techniques, so that a relative void content comparison can be made.

The permeability results show that as the fabric layers become less pliable, more deviations result in the macro permeability, since the layers are not able to mesh together as consistently. For all fabric cases, the macro permeability decreases as the micro-permeability parameter increases. For each fabric, as the disparity in the value of the macro permeability and micro-permeability parameter grows, a parameter established as the partially-saturated length additionally increases.

The void distribution results show that if resin is not allowed to bleed, the void content over the length of the part is not uniform; the percentage of voids is much higher near the vent side of the part. When no resistance is used at the vent, the voids increase through the thickness of the part; this trend levels out when resistance is added. When bleeding is allowed and if a resistance at the vent is added, all void levels are reduced.

Chapter 1

INTRODUCTION

In composites processing, many individual components must be considered independently, yet must then be coupled to assure they can all work together to form a sound overall system, which achieves a defect-free part. The type of processing technique that is chosen is clearly an integral aspect of the overall system, and two of the key liquid composite molding (LCM) techniques are introduced and discussed. The type of fabric that is used within the process also plays a crucial role. Two of the main categories of fibrous media are discussed and the differences between them are emphasized, especially regarding the flow progression through them. The typical characterization methods of these fabrics are covered and the need for a new method is exposed. The processing issues that arise are highlighted, and the proposed techniques to overcome such concerns are explained. The need to visualize the system becomes clear, which is why mold filling simulations are warranted and implemented, and the abilities the simulations have are uncovered.

1.1 Liquid composite molding (LCM) processes

LCM techniques utilize thermosetting resin to impregnate stationary fibrous preforms. The fabric is the reinforcing component, which carries the load, while the resin is the matrix component of the composite, which binds the fibers together. These LCM methods implement either a matched mold or a single-sided mold, depending on the application of the part being fabricated.

1.1.1 Resin transfer molding (RTM)

RTM is a matched mold process in which resin is injected into a dry fabric preform at either a constant pressure or constant flow rate. The fabric is contained within the cavity of the closed mold and the chosen injection scheme displaces the air from the cavity and impregnates the preform [1]. Once the mold is filled and the part is infused with resin, the injection is discontinued and the part is allowed to cure. The finished part hardens during the cure cycle, in which the polymer monomers crosslink and form networks solidifying the resin. The part is then demolded by separating the mold halves. A schematic of the RTM process is shown in Figure 1.1.
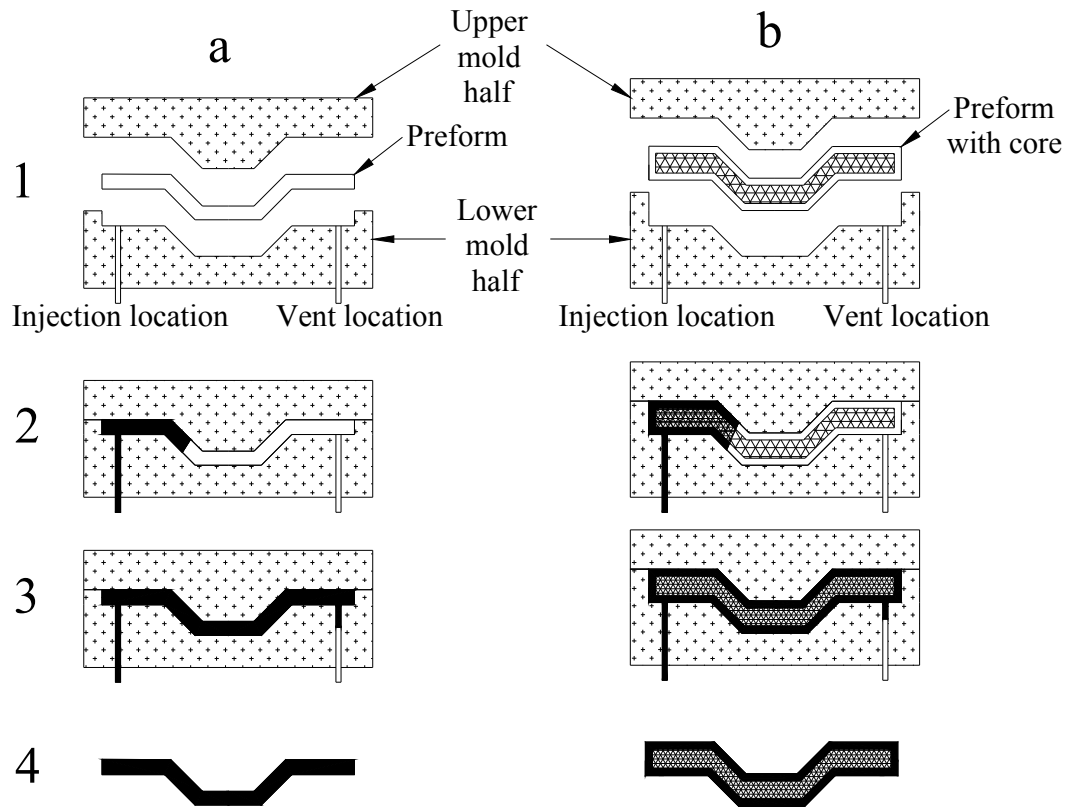
Figure 1.1: **A cross-section of RTM, a matched mold process, is shown along the length of a preform. The molding scenarios depict either pure fabric layers (a) or layers containing a core (b). The preform is first (1) cut and placed into the mold cavity, then (2) the mold is closed and injection is initiated, next (3) the resin injection is completed and the part is allowed to cure, and finally (4) the part is demolded.**

RTM is a composites manufacturing technique with many advantages. Large, complex parts, which may include inserts or cores to increase the stiffness of the part, can be fabricated relatively quickly. Well consolidated parts with a good surface finish and tight tolerances can also be achieved, due to the fixed distance and clamping pressure of the mold cavity. The volume fraction of fibers can be controlled based on how many layers of fabric are compressed into the mold as it is closed and

held together by clamps or bolts. The method used to stack the fabric layers can also be adapted to achieve the best mechanical properties. Also, since the chemicals and the fabric are contained within a closed mold, there is less exposure to volatiles [2].

Some of the inherent disadvantages with RTM arise from the variations in the fabric itself. These disparities result from how that fabric is cut, placed, and stacked and the fabric inconsistencies lead to parts that are not reproducible. The design of the mold is also critical to ensure no dry spots, or macro regions without resin, remain. The proper placement of vents and gates reduces the formation tendency of these dry spots. The presence of any voids leads to unfavorable mechanical properties such as interlaminar shear strength, tensile strength and modulus, flexural strength and modulus, and impact, to name a few [1]. The fabric within the mold must additionally refrain from any type of movement; this fabric movement is either caused by having a resin pressure that is too high, or not having sufficient fabric compaction [2].

1.1.2   Vacuum assisted resin transfer molding (VARTM)

VARTM is a single-sided mold process in which thermosetting resin is driven through a dry fabric preform by a gradient created due to the application of vacuum pressure. The empty regions that are within the fabric preform, which is found between a rigid mold tooling and a flexible plastic vacuum bag, are thereby filled. The desired fabric is positioned between two layers of porous release film. These layers are cut larger than the preform to allow for easy release from the mold tool and to assure all components used for the process do not remain permanent features of the cured part. Below the bottom layer of release film, a release interface is used on the mold tool to enable the removal of the part from the surface. Above the

top layer of release film, a distribution media (DM) is introduced to aide the advancement of the flow along the face of the preform. This DM is a very permeable layer placed on top of the layers being infused, in order to quickly move resin along the top surface of the part. The DM is cut smaller than the preform in both the width and the length direction. This is done to prevent the resin from racing along the sides of the part and reaching the vent before the flow along the tool surface has had time to catch up with the flow along the top surface of the part.

Tubing is used to inject the mold with prepared resin contained outside of the lay-up. The inlet and vent line are connected to omega tubes, which provide a line injection and flat contact surface on the actual part. This tubing is cut to length based on the width dimension of the DM, since the DM is the network of channels that advances the flow and the surface on which the injection occurs. A breather cloth can be optionally implemented at different locations of the lay-up, either under the injection and/or vent line or along the entire length of the DM. This cloth slows the flow, so parts, especially when thicker, have the chance to be infused through the thickness without a huge discrepancy in the lead length. The lead length is defined as the distance that exists between the flow front along the DM at the top of the part and the flow front along the tooling surface that occurs at the bottom of the part. If the lead length is reduced, resin has the ability to infiltrate all areas before resin reaches the vent line.

All of the components are surrounded by a sealant tape and covered by a plastic film that adheres to the tape, so a vacuum can be drawn on the entire lay-up. The vacuum pulls the resin along the DM and enables the preform to be transversely impregnated with resin. A schematic of the VARTM process is shown in Figure 1.2.
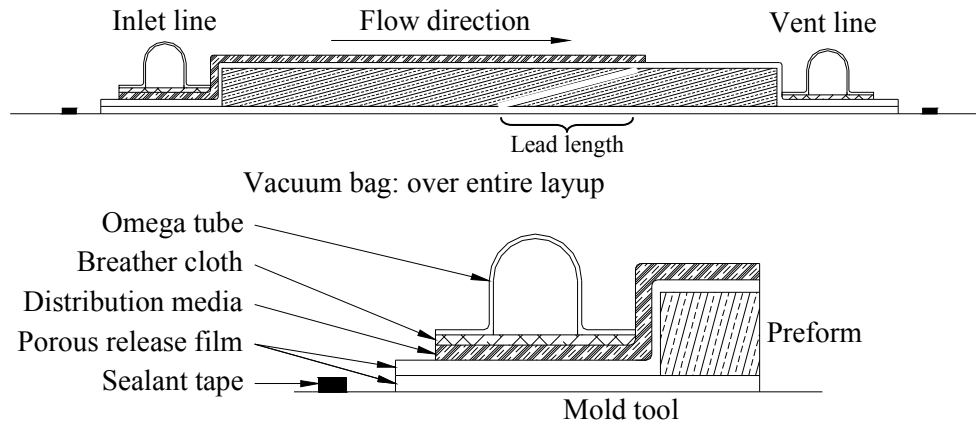
Figure 1.2: **A cross-section of VARTM, a single-sided mold process, is shown along the length of a preform. The overview schematic highlights an example of a flow front (in white) and the corresponding lead length. The close-up view of the inlet-line region highlights the different components needed for the process.**

The advantages of VARTM include a simple injection scheme and one-sided mold tools. Very large parts can be manufactured at a relatively low initial cost, since only a mold tool, which can be a simple table top for flat panels, fabric, resin, bagging materials, and a vacuum line are needed. Due to the clear plastic bagging film, the flow can additionally be visually inspected as filling progresses [2].

However, many hurdles and disadvantages exist. Since VARTM only uses one atmospheric pressure to both compact and inject a preform, lower fiber volume fractions and longer filling times can be anticipated. The volume fraction of fibers may vary locally, since the part thickness can not be exactly controlled as in RTM, where the layers are compressed into a cavity with a set thickness. The technique to bag the mold also takes skilled labor; if the bagging is not done correctly, leaks will introduce air in the part. Additionally, the amount of materials wasted in the

process is high. Moreover, the surface finish and tolerances of the parts are low, since the parts are not sandwiched between two smooth mold halves [2].

1.2   Fibrous porous media and permeability implications

Both RTM and VARTM are composites manufacturing processes that utilize fabrics which are considered either single-scale or dual-scale fibrous porous media. The differentiation in the type of media stems from the actual architecture of the fabric. The implementation of one fabric over another is based on the preferential properties that are required for the application of the part being manufactured. Certain applications need increased strength properties in one or even multiple directions, and must necessarily incorporate oriented fabrics into the manufacturing process; but, other applications hope to take advantage of the random and thus isotropic nature of non-oriented fabrics.

1.2.1   Single-scale porous media

Random mat fabrics, of which a close-up image is shown in Figure 1.3, are comprised of randomly oriented fibers that have no preferred direction. Small bundles of approximately one hundred individual fibers are randomly sprayed to form a fabric mat. Such fabrics are the most cost effective and easy to form and process; but, due the low fiber volume fraction, random mat fabrics cannot be used for high performance applications in terms of strength and stiffness [2].
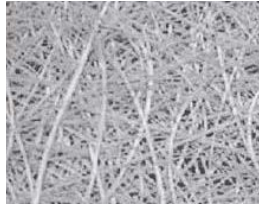
Figure 1.3:   Random mat fabric [2], which has no preferred orientation, is a type of single-scale porous media.

Because of the isotropic nature of such fiber mats, random mat fabrics have only one length scale. As fluid fills the regions that are found between the small fiber bundles, the bundles simultaneously fill. The bundles are loosely packed and the diameters of the bundles, which are only tens of microns, are of the same order as the space between the bundles. As the diameter of the bundles become significant and thus no longer consist of hundreds, but of thousands of aligned individual fibers, the bundles are termed fiber tows.

When flow progresses through single-scale porous media, the flow front coincides with the fully-saturated fluid front. This type of flow phenomenon is an important distinction. In such a flow, only one length scale is inherent to the fabric and the fabric is accordingly characterized by one permeability value.   The permeability value represents the ease through which a fluid can flow through a fabric. The number of permeability values that must be determined for a fabric is associated with the number of significant length scales that comprise the fabric.

1.2.2   Dual-scale porous media

Oriented fabrics are comprised of fiber tows; thousands of individual fibers that have a diameter on the order of a few microns are bundles together to form a tow that has a diameter on the order of millimeters. These bundles are then stitched,

woven, or braided together, as shown in Figure 1.4. A preform architecture that has a preferred layout can thereby be achieved, which is easy to handle in the form of a textile roll. The ordered fabric that is created enables for packing of more fibers, which increases the performance, though the ease of processing is reduced [2].
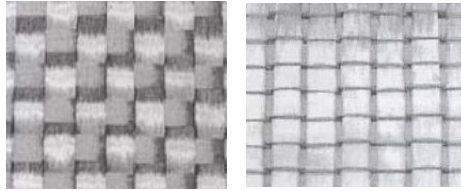
Figure 1.4: **Woven and stitched fabrics [2], which are comprised of fiber tows and thus have a preferred orientation, are examples of dual-scale porous media.**

Due to the large fiber tows, two length scales exist in such fabrics. The inter-tow regions between the fiber tows are on the order of millimeters, while the intra-tow regions between the individual fibers within the tows are on the order of microns. The tows are tightly packed and the diameter of these tows is significant; thus, the tows become an integral component of the flow analysis. As the flow progresses through dual-scale porous media, two flow regimes exist: the macro flow along the length of the fabric and the micro flow impregnating the tows of the fabric. Consequently, the flow front and the fully-saturated front do not coincide; the distance between the two flow fronts is deemed the partially-saturated length. Fluid impregnates the fiber tows at a delayed rate, since the resistance to flow is much higher in the micro regions of the tows. Due to this flow phenomenon, two permeability values must be used to characterize such porous media.

1.3 Darcy's law and permeability characterization methods

There are different types of permeability characterization methods that are currently employed to determine this important material parameter. New and improved characterization methods are also continually sought. The permeability itself cannot be directly measured; the value must be determined from other quantities that are measurable. This resulting data must then be used in conjunction with Darcy's law, which models flow through porous media:

$$\left\langle \overline{v_d} \right\rangle = -\frac{\overline{\overline{K}}}{\mu} \cdot \nabla p .$$ (1.1)

This relation expresses the average Darcy flow velocity vector, $\left\langle \overline{v_d} \right\rangle$, as a function of the permeability tensor of the preform, $\overline{\overline{K}}$, the viscosity of the fluid, μ, and the pressure gradient, ∇p. This formulation can be completely expressed, using a matrix representation as follows:

$$\begin{bmatrix} \left\langle v_d \right\rangle_x \\ \left\langle v_d \right\rangle_y \\ \left\langle v_d \right\rangle_z \end{bmatrix} = -\frac{1}{\mu} \begin{bmatrix} K_{xx} & K_{xy} & K_{xz} \\ K_{yx} & K_{yy} & K_{yz} \\ K_{zx} & K_{zy} & K_{zz} \end{bmatrix} \begin{bmatrix} \partial p / \partial x \\ \partial p / \partial y \\ \partial p / \partial z \end{bmatrix} .$$ (1.2)

$\left\langle \overline{v_d} \right\rangle$ is additionally defined as the ratio of the flow rate vector, $\overline{Q}$, to the cross-sectional area through which the flow is progressing, A, by the expression: $\left\langle \overline{v_d} \right\rangle = \frac{\overline{Q}}{A}$. This expression can then be related to Darcy's law.

In the system of equations, the coordinate direction in the direction of flow is x, that perpendicular to the flow is y, and that transverse to the flow is z. When orienting the fiber tows of a biaxial fabric parallel to the flow, the coordinate flow direction becomes a principal direction. Based on the fabric orientation, only the

principal coordinates (K_{xx}, K_{yy}, K_{zz}) remain, since the coordinate directions are chosen along the principal axes of the preform. The permeability tensor reduces to one that is diagonal. Relating the fabric geometry to the tensor, by aligning the coordinate and principal directions, shows how all off-diagonal terms of the tensor are thus zero [3]. Accordingly, when evaluating only a 1D flow progression in the flow direction, the system reduces to only one equation:

$$\langle v_d \rangle_x = -\frac{K_{xx}}{\mu}\frac{dp}{dx}. \tag{1.3}$$

It is evident from the 1D Darcy relationship, when related to the definition of velocity, $\frac{Q}{A}$, that the unknown permeability can be determined in one of two ways. A constant pressure injection can be employed, from which flow rate data can be captured, or, a constant flow rate injection can be employed, from which pressure data can be captured.

The most basic permeability characterization techniques assume there is only a macro permeability value to be determined. These methods rely on a matched mold and an RTM process in either a 1D linear or a 2D radial flow configuration. In the linear case, only the in-plane permeability of one fabric direction can be obtained, since the flow stems from a line source and is assumed to be 1D. In the radial case, the permeability of both in-plane fabric directions can be obtained, since the flow stems from a point source and is assumed to be 2D [2].

If the permeability of one in-plane direction is known, a VARTM experiment can be conducted, during which the arrival-time data is captured. This information can then processed using a permeability estimation algorithm, to determine the transverse permeability, as well as the permeability of the DM used for

11

flow enhancement [4]. Alternatively, one VARTM experiment can be conducted to determine both the in-plane and out-of-plane permeabilities, using PERMSTAT, a permeability measurement workstation developed at the Center for Composite Materials at the University of Delaware.

Methods clearly exist which can characterize the macro permeability in different fabric directions [5-15], but no methods exist which are able to handle the determination of both the macro-scale and micro-scale permeability of dual-scale fabrics. Such a method is necessary to ensure both values are captured and characterized. As with any permeability measurements that are performed, it is well known that ten to twenty percent variability from one experiment to another is not uncommon [2]. The values obtained from measurements are not necessarily repeatable, due to local compaction and nesting variations that change from one test to another as a result of how the fabric layers are cut, placed, and stacked. The experimental measurements need to be coupled with numerical and analytical predictions to get a better understanding of the flow in dual-scale porous media and the impact on micro void formation.

1.4   Void formation and processing techniques

The main goal of all LCM methods, irrespective of the type of fabric employed, is to manufacture a part that does not contain any regions devoid of resin. Macro-voids may result if the available fluid pressure cannot overcome the resistance the fabric is providing. The resin is ideally displacing the air in the preform, but if it is unable, air may remain entrapped. These voids extend to the micro level in dual-scale fabrics. The flow progresses more quickly between fiber tows, since the resistance is lower there than within the tows. This provides the opportunity for the resin to

encircle certain tow regions and entrap micro-voids within [2, 16, 17]. The different void-entrapment scenarios are highlighted in Figure 1.5.
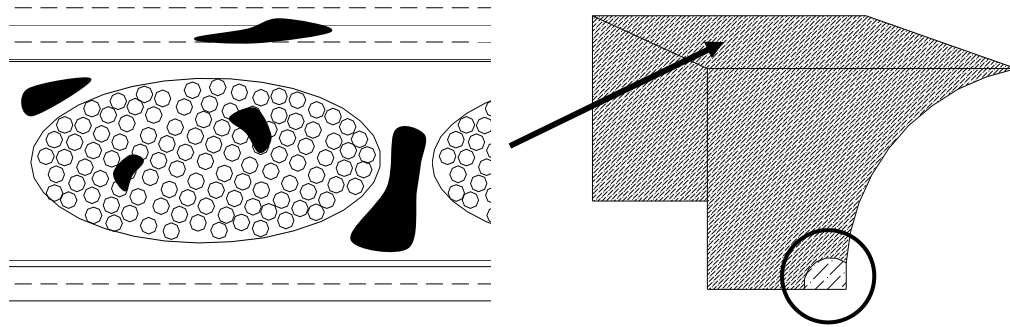
Figure 1.5: **Micro voids – depicted in black – are entrapped either between fiber tows or within fiber tows within a much larger part. Macro voids – an example of which is circled – especially result when pockets within parts remain unfilled.**

The two dissimilar permeability values in the macro and micro regions are clearly very important in that they impart specific tendencies, such as the formation of voids. If the processing techniques used to manufacture parts composed of dual-scale media are altered, the degree of void entrapment can be significantly reduced. The first technique that can be employed is to allow the resin bleed, or continue to flow even once the flow has reached the vent. This way the fiber tows, which have a much lower permeability, are given additional time to fully saturate. Figure 1.6 depicts how the fiber tows would begin to fill more uniformly along the length of the part if resin is allowed to bleed, as compared to the case when the resin injection is discontinued as soon as it arrives at the vent. In the latter case, the part may be fully saturated near the injection gate, but tows in the proximity of the vent may not at all be impregnated with resin.
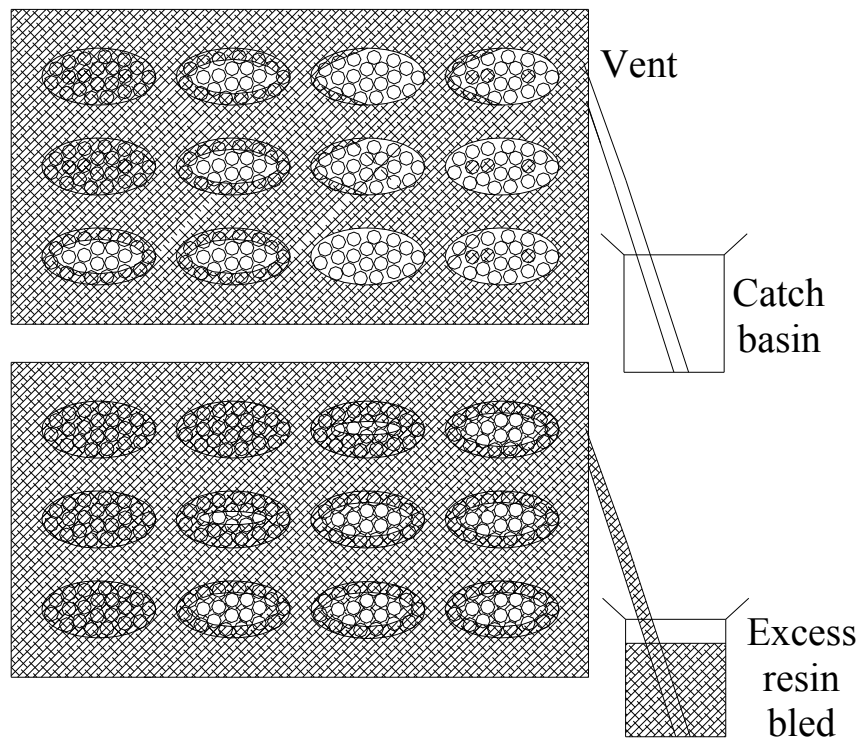
Figure 1.6: **The fiber tows may be filled at the beginning of the part if bleeding is not allowed, but tows at the end may not at all be filled. Alternatively, if bleeding is employed, the degree of resin impregnation ideally becomes more uniform over the length.**

Alternatively, additional resistance can be included near the end of the part, in order to alter the flow and drive the resin into the micro pores within the tows. This is done to ensure the tows are completely permeated with resin. A higher pressure is induced in the mold as a result of the resistance, which ideally enables faster impregnation of the fiber tows. As shown in Figure 1.7, the addition of only resistance could result in a similar degree of filled tows as in the case of only allowing bleeding; the location and distribution of the specific tows that are more filled would just vary. Ideally, if both techniques are incorporated, all fiber tows will be filled with

resin and any remaining void content will be uniform over the length and through the cross-section of the part. Less resin would also need to bleed, since the resistance is aiding in the saturation of the tows.
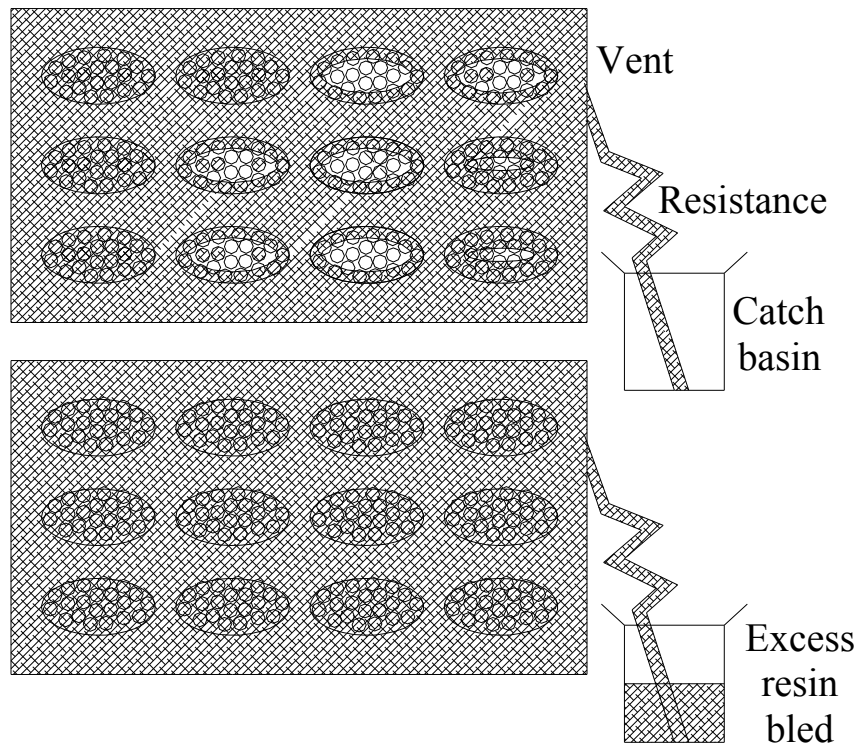
Figure 1.7: If resistance is employed at the vent, the degree of resin impregnation ideally improves over the length of the part. If both bleeding and resistance are integrated, all fiber tows will ideally fill.

Two key technical questions remain: How long should the resin be allowed to bleed? How much resistance should be attached to the vent? To answer these questions, the macro-permeability value of the bulk preform and micro-permeability value of the fiber tows must be known. In order to explore these

questions further, one must also be able to incorporate these values into a filling simulation that models flow through dual-scale porous media. Simulation and experimental investigations are important so that micro-voids, such as the ones shown in Figure 1.8, can be addressed.
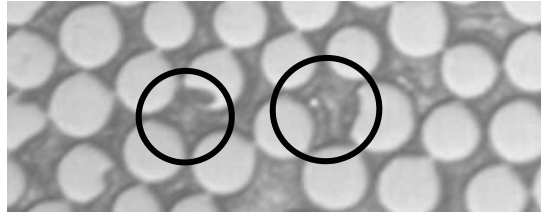
Figure 1.8:   Micro-voids can result if the appropriate processing techniques are not addressed or applied.

1.5   Fill time and flow simulation

Other major goals of LCM processing are to fabricate parts in the shortest time and in the most cost effective manner possible. Flow simulations are developed to replicate mold filling processes and scenarios. This way many processing techniques can be evaluated without necessitating trial and error techniques, in which materials and therefore money are lost. The movement of resin can be predicted, which is particularly helpful if a closed-mold process is used, since the flow progression cannot be visualized. Based on the type of fabric and mold being used, the permeability parameters can be input, along with other key parameters (fiber volume fraction, viscosity, etc.) and all geometric considerations. Flow behavior can be better understood using flow simulations. The tooling and overall process can be

better designed to ensure the fabrics within the mold will result in the lowest percentage of voids and fully permeate in the least amount of time.

Liquid Injection Molding Simulation (LIMS) has been developed at the University of Delaware in order to simulate LCM processes. LIMS uses a finite element/control volume approach to implement Dacry's law and model the flow through a generated mesh that represents the part being infused with resin. The moving flow front is tracked by the fill factors associated with the control volume surrounding each node of the generated mesh. The fill factors report the fraction of fluid that occupies each control volume; a value of zero corresponds to empty and a value of one corresponds to full. At each full node, the pressure values are calculated, and at each time step, the flow is advanced as the fill factors are updated [2].

LIMS has the ability to combine 1D, 2D, and 3D elements so that each component used in processing can be modeled, yet the parameters thereof can be independently set. Additional scripts can be used to modify the parameters of the simulation. When evaluating dual-scale porous media, a specific script is used that evaluates the saturation of the fiber tows [18]. This script couples the flow at the macro and micro scale by combining 2D or 3D elements that represent the flow between the tows with 1D elements that model the flow within the tows; however, the permeability values for 2D elements that represent the macro flow and the 1D elements that represent the micro flow must both be provided. From there, the injection scheme can be introduced, the flow progression can be visualized, and the location of dry spots can be predicted. The actual flow rate and pressure distribution data can additionally be monitored and collected, so that the results can be compared with experimental results.

17

1.6   Summarized objectives

The main objective of this work is to experimentally characterize both the macro-scale and micro-scale permeability of different fabric preforms. A 1D constant flow rate RTM system is employed in order to gather pressure data over the duration of the injection, so that Darcy's law can be used to determine the macro permeability. The RTM experimental and flow conditions are then replicated in the LIMS environment in order to determine a fitting parameter associated to the micro-permeability. All parameters are held constant except for the micro permeability, which is changed until the pressure profile from LIMS matches the experiment most closely. Characterizations of four different fabrics are performed.

The determined permeability values of the fabric are then applied to a LIMS model of the VARTM process. The infusion schemes are altered in order to correlate void content and distribution to the processing techniques. The impact different micro permeability values have on the time to fully saturate the part are also investigated. The relative void contents are additionally experimentally determined, since valuable insight is provided into the actual distributions throughout a composite panel. The experimental trends are compared with trends resulting from the simulations.

Chapter 2

**PERMEABILITY CHARACTERIZATION OF DUAL-SCALE FIBROUS
POROUS MEDIA**

2.1 Introduction

It has been known for some time that woven and stitched fabrics inherently induce a dual-scale flow behavior [19, 20]. These porous preforms are comprised of distinct macro- and micro-flow regions, which exhibit distinctly different impregnation rates and, therefore, each correspond to a different permeability value. The macro pores between the fiber tows will fill more rapidly, while the micro space between individual fibers within the tows will saturate more slowly, due to the smaller size of the pores. The size of the pores between the tows, the diameter of the fibers within a tow, and the architecture of the preform all play a role in the determination of the preform permeability.

The distinction between these separate inter- and intra-tow flow regions is important, due to the delay that occurs in the complete saturation of the preform. The macro flow front first impregnates the more permeable pores between the tows. Then, the fluid from the macro region impregnates the less permeable pores within the tows, at which point the more slowly advancing micro flow front dictates the filling progression. For this reason, the location of the macro flow front seldom coincides with the fully-saturated fluid front. For such preforms, a partially-saturated zone exists and can be defined as the region in which the macro pores in between the fiber tows

may be filled, but the fiber tows are only partially filled. In 1D flow, one can define a partially-saturated length, Ls, which is the distance between the macro flow front and the fully-saturated front, as depicted in Figure 2.1. The tows ahead of the macro flow front are completely *unsaturated* and the tows behind the fully-saturated front are completely *saturated*.
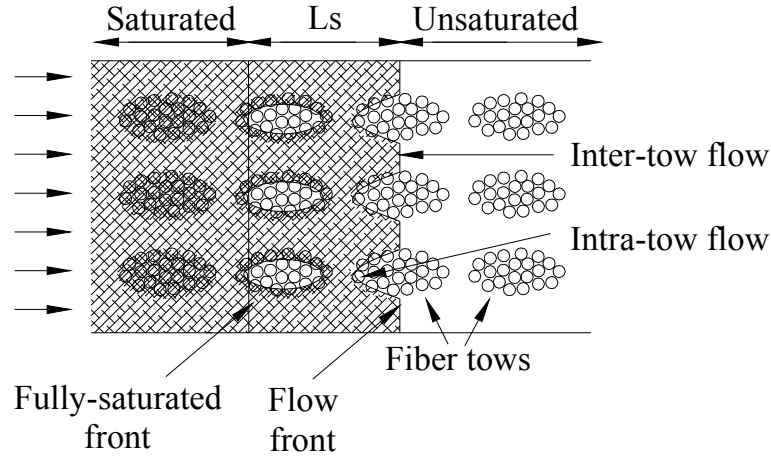
Figure 2.1: **A schematic that depicts the saturated, partially saturated (Ls), and unsaturated flow regions within dual-scale preforms, and highlights the delayed impregnation of the fiber tows.**

The partially-saturated length decreases as the value of the micro permeability of the fiber tows moves closer to the value of the macro permeability of the preform. Single-scale fabrics, such as most random mats, which only have one permeability value, are the most extreme case in which the micro permeability is inherently equal to that of the macro permeability; accordingly, these fabrics have no partially-saturated length.

In order to properly determine the permeability of a fabric preform, the results of a 1D constant flow rate injection experiment are interpreted in the two inter-

and intra-tow regions. Darcy's law, which is used to describe flow through porous media, must be correctly applied to the different regions, since a delayed or lagging flow behavior is exhibited. In a single-scale fabric, i.e. random mat, the pressure drop relationship over time that results from this 1D constant flow rate experiment exhibits a linear behavior. When experimentally evaluating dual-scale fabrics, this linear trend only holds for two specific cases.

On one hand, the permeability of the tows may be of the same order as the macro permeability; therefore, both regions fill simultaneously and the pressure as a function of time grows linearly. For this type of flow, the macro permeability of the preform can be characterized. On the other hand, the permeability of the tow may be many orders of magnitude smaller than the macro permeability, in which case the tows remain completely empty in the time it takes to fill the regions in between the tows. For this case, the pressure as a function of time again grows linearly, but more quickly than the previous case. For this type of flow, the unsaturated macro permeability can be characterized; this is the macro permeability of the preform for the case in which the fiber tows remain completely unsaturated.

For the linear cases outlined above, the conventional Darcy's law relationship, as expressed in Equation (1.1), is valid. Darcy's law can be simplified to one-dimension and re-expressed as:

$$\langle v_d \rangle = \frac{K}{\mu} \frac{dp}{dx},$$
(2.1)

where the permeability in the flow direction, K, is a scalar value. This expression is a generic form of the 1D relation reached in Equation (1.3). When applying this relationship to a planar 1D flow experiment in which the test fluid is injected into the

preform through a mold cross-section, A, at a constant flow rate, Q, the definition of velocity, $\langle v_d \rangle = \dfrac{Q}{A}$, can be related to Darcy's law.

The 1D Darcy relation can then be re-cast in terms of the changes in the injection pressure, P_{in}, and the position of the macro flow front, x, with respect to time:

$$\langle v_d \rangle = \frac{K}{\mu} \frac{m}{\left(\frac{dx}{dt} \right)}, \tag{2.2}$$

where $\dfrac{dP_{in}}{dt} = m$ is the slope of the inlet pressure profile with respect to time for a constant flow rate injection experiment.

To enable one to find the preform permeability, the flow front velocity, v_{ff}, is expressed in terms of the Darcy average velocity by dividing it by the available porous volume, as dictated by mass conservation:

$$\frac{dx}{dt} = v_{ff} = \frac{\langle v_d \rangle}{\phi}. \tag{2.3}$$

This expression must be implemented, since the average Darcy velocity ($\langle v_d \rangle = v_{ff}\phi$) can only account for the porous region that must be filled within the fiber architecture.

Equation (2.3) is substituted into Equation (2.2) and the definition of velocity, $\dfrac{Q}{A}$, is implemented. A rearrangement of terms results in an explicit expression for the permeability of the preform in the direction of the flow:

$$K = \frac{\mu}{m\phi} \left(\frac{Q}{A} \right)^2. \tag{2.4}$$

Clearly only one permeability value can be ascertained from Equation (2.4). The micro-scale impregnation is in effect neglected, which is a valid assumption for a single-scale preform or a dual-scale preform in which the tows exhibit the behavior of one of the two extreme cases mentioned: the tows are either completely unsaturated or

completely saturated. For these cases, one expects that for a constant flow rate injection, the change in pressure at the inlet with respect to time will be linear, resulting in a constant value for the slope.

It is evident from Equation (2.4) that a steeper slope will result in a lower permeability value. When the fiber tows of a preform remain completely unsaturated as fluid flows through a dual-scale fabric, the pressure grows linearly and quickly. The dry fabric is providing resistance, resulting in a steeper slope and hence a lower permeability value. If the tows are completely saturated, it is suspected that the fluid inside the tows is stagnant [9] and only the fluid outside the tows is flowing. There is less resistance to the flow in this case since the tows are filled with fluid and provide lubrication for the bypassing flow. The pressure still grows linearly, but not as quickly as in the former case, resulting in a less steep slope and hence a larger permeability value as compared to the unsaturated case. Such findings were reported by Breard *et al.* [21].

The region between the two extreme linear cases represents the true nature of the flow. The tows at the inception may be completely unsaturated; therefore, the pressure profile with respect to time at the inlet begins briefly on the pace of a completely unsaturated preform and is linear. Then this profile becomes non-linear to reach the pace of a completely saturated preform, which is again linear. The impregnation of the fiber tows that begins during this non-linear phase is accomplished by applying mass conservation with a sink term to the macro flow.

A mass balance can be performed on the elemental volume shown in Figure 2.2.

$$(1 - V_f^{tow}) \cdot V_f^{tows\,inEV} \cdot \frac{\partial s}{\partial t}$$
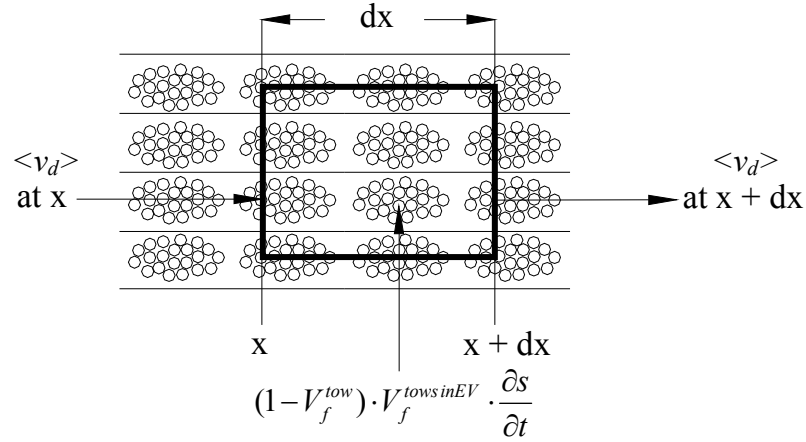
Figure 2.2: **A mass balance is performed on an elemental volume. The sink term resulting from the impregnation of the fiber tows must be accounted for to properly model the flow.**

The mass balance results in the following expression:

$$A \cdot dx \cdot v_d - A \cdot dx \cdot (1 - V_f^{tow}) \cdot V_f^{tows\,inEV} \cdot \frac{\partial s}{\partial t} = A \cdot dx \cdot \left(v_d + \frac{\partial v_d}{\partial x} \cdot dx \right), \qquad (2.5)$$

where A is the cross-sectional area of the elemental volume and dx is the length of each side of the element. $V_f^{tows\,in\,EV}$ is the volume fraction of tows in the elemental volume, $(1 - V_f^{tow})$ is the remaining porous volume fraction in each fiber tow, and $\frac{\partial s}{\partial t}$ is the saturation rate of the fiber tows. The fiber tows act as sinks which drain away fluid from the advancing flow front; by rearranging the mass balance expression, the mass conservation with the sink term is achieved in the one dimension of interest:

$$\frac{\partial v_d}{\partial x} = -(1 - V_f^{tow}) \cdot V_f^{tows\,in\,EV} \cdot \frac{\partial s}{\partial t} = \nabla \cdot \langle \overline{v}_d \rangle_{in1D} \, . \qquad (2.6)$$

Once the fiber tows are fully saturated, there will be no remaining porous volume to fill $(1 - V_f^{tow} = 0)$; therefore, Equation (2.6) reverts back to the homogeneous form of mass conservation:

24

$$\nabla \cdot \left\langle \overline{v}_d \right\rangle = 0 \,. \tag{2.7}$$

This important application of the sink term to the mass conservation equation is incorporated into the finite element/control volume based LIMS model that predicts the flow of resin through dual-scale fibrous preforms [18]. The interactions of the inter- and intra-tow regions are modeled in the LIMS environment by attaching 1D elements that represent the micro-flow regions to each node of the 2D or 3D elements that represent the macro-flow regions, as seen in Figure 2.3.
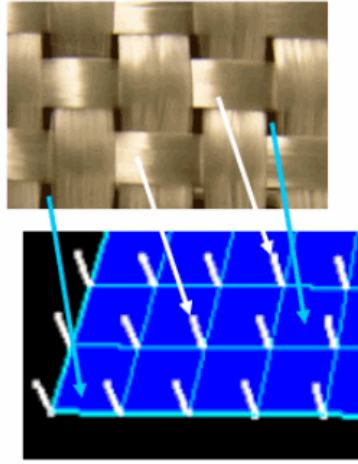
Figure 2.3: **Inter- and intra-tow interactions are modeled in LIMS by attaching 1D elements, which represent the flow regions into the fiber tows, to the 2D or 3D elements, which represent the flow regions between the tows.**

The 2D or 3D elements represent the regions in between the tows that are the pores the macro flow will saturate. The extra nodes imposed by the addition of the 1D elements represent the fiber tows and the associated micro pores to be saturated. The two types of elements are assigned separate permeability values corresponding to the macro

permeability of the bulk preform and the micro permeability of the fiber tow. Since the 1D elements share the nodes and consequently pressure values with the 2D or 3D mesh, the micro flow is coupled with the macro flow. The saturation of the tows can be tracked, as well as the impact this impregnation has on the injection pressure, which can be monitored at an inlet node. This numerical methodology is completely outlined in the work of Simacek and Advani [18].

This model is chosen, as it allows one to determine the pressure profile at the inlet by specifying the macro and the tow permeability, for the inter- and intra-tow regions respectively. A methodology is introduced that allows one to estimate the macro permeability and a fitting parameter associated to the micro permeability of dual-scale preforms by matching the inlet pressure profile from LIMS to the data obtained from experiments. A validation of the methodology is provided and permeability values for four distinctly different fabrics are calculated.

2.2 Background

2.2.1 Modeling

Modeling the dual-scale nature of fibrous preforms by implementing not only the macro flow, but also the micro flow, is not a new trend. Parnas and Phelan [19] recognized, early on (1991), the importance of evaluating the global flow front along with the local impregnation of the fiber tows. The model incorporated a sink term, which takes away fluid from the advancing flow front. This was a key development since it coupled the flow at different length scales by combining 1D radial flow into the tow with 1D linear flow along the length of the preform. Sadiq *et*

26

al. [20] experimentally investigated the model, and observed key trends, which reinforced the importance of the need for such models.

Many further models have been developed, which evaluate unsaturated flow, which is through initially dry porous preforms. These models explore how the macro flow behavior is influenced by the impregnation of the fiber tows [5, 6, 22-28]. Such models have the ability to be transformed into flow simulations, in order to numerically incorporate the sink that causes the non-linearity in the pressure profile. However, for accurate predictions, one would have to supply two permeability values: one for the bulk flow and one for the impregnation of the tows, hence the need to characterize both values.

2.2.2 Experimental Investigations

Experiments to determine the in-plane bulk permeability have been developed and various pitfalls in measurement techniques have been improved and corrected [5-15]. For dual scale preforms, Parnas *et al.* [7] conducted 1D linear and 2D radial flow experiments at a constant injection pressure. The unsaturated and saturated permeability values were compared, which are associated with the flow through a dry and an already impregnated preform, respectively. A difference between the two values was observed for both random mat and woven fabric. Luce *et al.* [8] extended this work by conducting the same type of experiments, but utilizing preforms composed of two types of fabric. The impact of compaction of the preform was additionally addressed. Binetruy *et al.* [5] also conducted constant injection pressure experiments and highlighted the difference between the saturated and unsaturated regions of the preform. They concluded the micro flow had no effect on the saturated

region, but that the unsaturated region is affected by the impregnation of the tows and accordingly affects the overall permeability of the preform.

Slade *et al.* [6] conducted 1D linear experiments at a constant flow rate, in order to evaluate the resulting pressure profile over time. The pressure results were used to determine both the unsaturated and saturated permeability values of random mat and stitched biaxial fabric. Babu and Pillai [9] also examined the pressure plots resulting from 1D constant flow rate experiments. This work studied what effect compression has on the pressure profile of biaxial stitched, triaxial stitched, biaxial woven, and unidirectional fiber mats.

However, no method has been found in which both the macro and micro permeability values can be determined from one experiment. A methodology to recover both the macro permeability and the micro-permeability parameter of different preforms by conducting a single RTM constant flow rate injection experiment is proposed. Experimental data is used to directly determine the macro permeability and the resulting pressure profile is compared to the numerical results generated by LIMS to determine the micro-permeability parameter. Both values can then be used in the LIMS environment to accurately predict the flow in closed mold processes.

2.3 Experimental procedure: macro permeability determination

In order to measure the permeability of different preforms, 1D constant flow rate RTM experiments are conducted. A closed mold is used, which consists of one 1/2"-thick aluminum lower mold half and one 2"-thick clear acrylic top mold half that acts as a viewing window. A 1/8"-thick aluminum spacer separates the two halves and provides the cavity within which the layers of fabric are placed. O-rings are fitted to grooves machined in both mold halves in order to seal the mold and prevent any

fluid from leaking out of the cavity. The mold is secured with twenty-six bolts, which are equally spaced and torqued. The mold is additionally reinforced to minimize any deflections, by clamping stiffening bars, which stand 2" on end, to the mold exterior. Similar apparatuses have been used by previous researchers [3, 29, 30]. A schematic of the mold is shown in Figure 2.4.
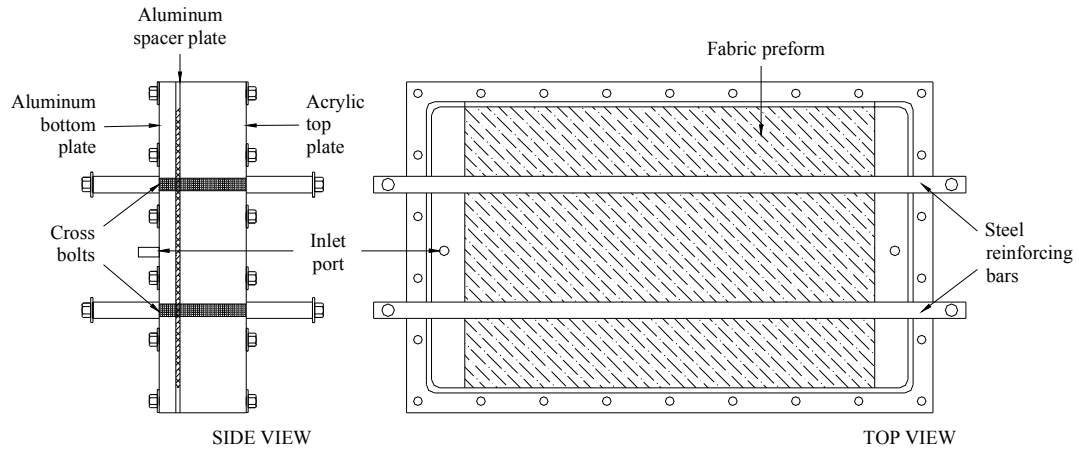
Figure 2.4:   Mold setup for 1D permeability determination experiments.

In order to achieve an experiment free of race-tracking along the edges of the preform, much care is taken when cutting each fabric layer. Race-tracking occurs when a channel of lower resistance is created along the edges of a preform within a mold cavity, as a result of frayed fabric edges or incorrect preform size [10]. The flow progression induced by having *no* race-tracking versus having race-tracking are shown in Figure 2.5. The flow must remain uniform in order to properly assume a true 1D line injection is being conducted, which is why race-tracking cannot be allowed.
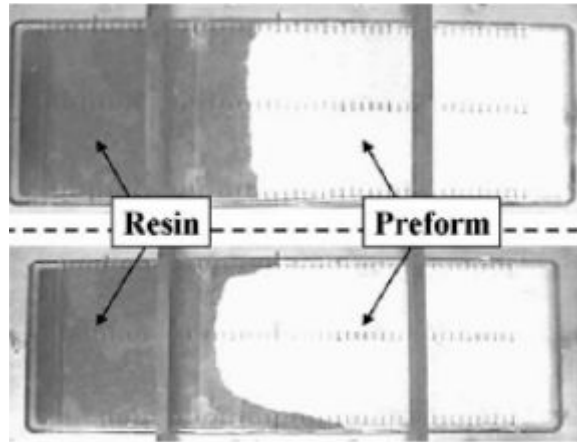
Figure 2.5: **One-dimensional line injections without and with race-tracking [10]. The flow front with race-tracking is not uniform, as is assumed when conducting a 1D flow experiment.**

A frame that is identical in dimensions to the mold cavity is used as a cutting template to ensure the width of the layers is as exact as possible. The fabric is cut to ensure the inlet port is left uncovered so that the test fluid first fills the empty space within the cavity and initiates a planar 1D flow through the preform. The vent port is also not covered by the fabric, so air can escape without any resistance or restriction. The cut preforms are 8 1/8" wide and 12" long in the flow direction.

Each experiment is videotaped to highlight three important criteria: (a) the progression of the flow front is straight, even, and steady; (b) the flow is free of edge effects such as race-tracking; and (c) no layers are washed away by the flow. The transparent top plate facilitates this procedure. The macro permeability measurements can be conducted in the presence of race tracking [10]. But, as stated above, the numerical LIMS analysis to which the experimental data is matched, assumes a true 1D line injection with no edge effects; therefore, the experiments are conducted to

match this assumption and if this criterion is not met, the data is discarded. The data is also discarded if one of the other two criteria is not met.

Vegetable oil, either pure or colored by the addition of an oil-based dye, is used as the test fluid in this study. The viscosity of the oil is measured before each experiment using a Brookfield viscometer. The oil is injected into the closed mold, by way of the inlet port, using a Radius brand injection machine; this injector moves a piston via a stepper motor, in order to provide a constant flow rate. The inlet pressure is recorded using a pressure transducer connected to the Radius injection system. This pressure data is collected over the duration of the experiment. The data collection is complete once the macro flow reaches the end of the fabric, but the injection continues until the pressure reaches a steady state, which indicates the preform is fully saturated with fluid. A schematic of the 1D flow controlled system is shown in Figure 2.6.
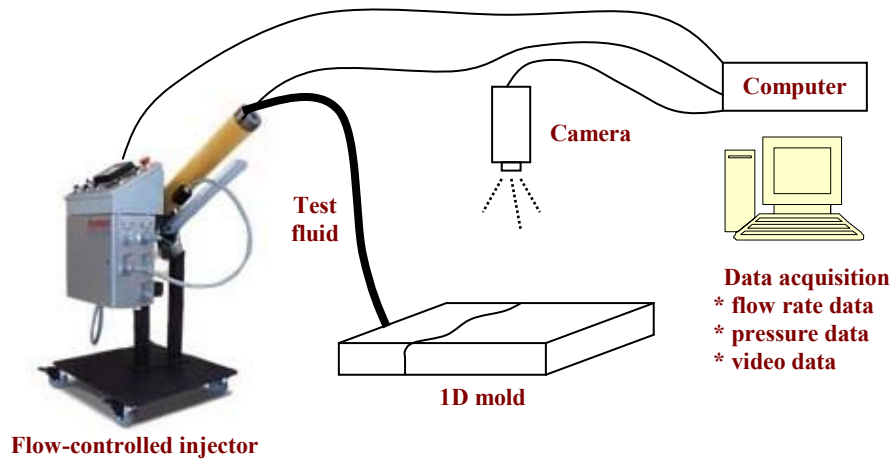
Figure 2.6: **Schematic of the 1D controlled flow system used to determine permeability values of fabric preforms.**

For each experiment, the inlet pressure data is plotted against time. The plot begins at time zero, which corresponds to when the oil enters the preform; the plot ends when the macro flow front reaches the end of the preform at time t_f. The plot, an example of which is shown in Figure 2.7, can be subdivided into three regions.
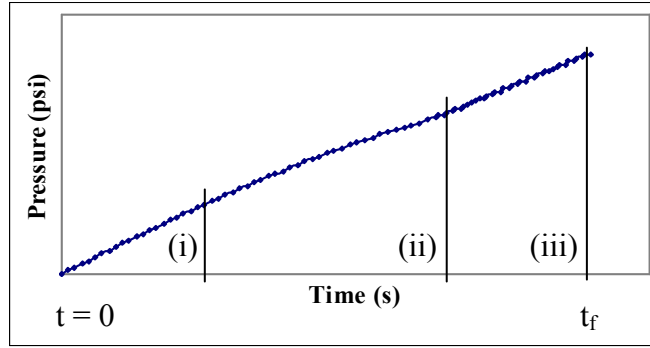
Figure 2.7: Dual-scale fabrics exhibit three flow regions; (i) an initial linear region, (ii) a non-linear region, and (iii) a final linear region, which represents the flow that has a constant partially-saturated length.

Linear region (i) is representative of the time frame during which fluid fills the macro pores, yet no micro pores have had time to be impregnated. Non-linear region (ii) is representative of the pressure response as the fluid of the macro flow front begins to impregnate the fiber tows. Linear region (iii) is representative of the period during which a constant partially-saturated length ensues.

As previously discussed, there are two flow regions in dual-scale fabrics: the inter-tow flow through the larger pores between the tows and the intra-tow flow through the smaller pores within the tows. In essence, the flow through both of these regions initially develops, but after a certain time frame becomes fully developed. The micro pores are more difficult to impregnate, so the time it takes the flow to fully develop will be longer than the time it takes the flow in the macro pores to fully-develop. In order for the constant partially-saturated length to exist in region (iii), the mold must be long enough to ensure that the micro flow front fully develops, meaning the fully-saturated front is present. Once both fronts fully develop, the fully-saturated front and the flow front are then traveling at the same speed. The complete

mathematical proof of this phenomenon is available in the Appendix of [31]. The partially-saturated length, which is the distance between the two fronts, is thus constant and the associated pressure drop is linear.

Using an excel template, the final experimental data point is fixed and preceding data points are added as to maximize the fit (R^2 value) of the linear best fit line passing through the data points. The distinction between region (ii) and (iii) can thus be made, since the addition of non-linear points from region (ii) would not improve, but impede the fit. Linear region (iii) is used to determine the macro permeability of the preform. The slope of the best fit line in region (iii), which is also determined by the excel template that is created as a data analysis tool, is used directly in Equation (2.4) to determine the macro permeability. Implementation of the slope of the best fit line of linear region (i) into the same equation results in the unsaturated macro permeability, but this is not the permeability value of interest.

Accordingly, a minimum requirement of the experiment is that an appropriate combination of volume fraction, viscosity, and flow rate are used in order to yield an experiment in which the tows of the fabric begin to fill and the constant partially-saturated length region is reached. The pressure plot therefore begins linearly, becomes non-linear, and finally reaches a linear slope during the final portion of the experiment. If this requirement is not met, the macro permeability value of interest can not be determined, since region (iii) will not exist.

2.4 Numerical procedure: micro permeability determination

The 1D constant flow rate RTM experiment is modeled to simulate the experimental conditions and parameters. Pressure data is generated and collected over the course of the injection, just as if a physical experiment were being conducted. A

rectangular mesh that is composed of square, 2D elements is generated to replicate the preform contained within the mold used in the experiment. The mesh size is eighty-three elements in length by sixty elements in width. These 2D elements are assigned a volume fraction, V_f^{bulk}, and a permeability value, K_{bulk}, within LIMS, both of which correspond to the bulk- or macro-impregnation regions of the preform.

One-dimensional bar elements are then attached to every 2D element node; the LIMS procedure and codes needed to accomplish this transformation of the mesh are included in Appendix A. These 1D elements are assigned a volume fraction, V_f^{tow}, and a permeability value, K_{tow}, representing the micro-impregnation regions of the preform, i.e. the fiber tows. By the addition of these 1D elements to the existing 2D elements, the interactions between the macro- and micro-flow regions are enabled.

A length, l, is set for each 1D element, each of which also has an associated initial default cross-sectional area, A^{tow}. This area is adjusted to $A^{tow-adj.}$ by the LIMS model, based on the set V_f^{tow} and the input V_f^{bulk}:

$$A^{tow-adj.} = V^{bulk}\left(\frac{V_f^{bulk}}{V_f^{tow}}\right)\left(\frac{2}{l}\right),\tag{2.8}$$

where V^{bulk} is the volume of a 2D element. V_f^{bulk} is next adjusted to $V_f^{bulk-adj.}$ in order to accommodate for the additional set volume fraction of the tows; this preserves the overall porous volume of the preform:

$$V_f^{bulk-adj.} = V_f^{bulk}\left(1+2\left[\frac{1-V_f^{tow}}{V_f^{tow}}\right]\right).\tag{2.9}$$

The parameters used to run each simulation, as well as the values of the parameters that are modified, are compiled in Table 2.1. The complete details governing the saturation program approach are explicitly outlined in [18] and the main steps to

conduct the simulation, inclusive of the code that incorporates Equations (2.8) and (2.9), are included in Appendix A.

Table 2.1: **Two- and one-dimensional element parameters corresponding to each LIMS flow simulation.**

	2D elements		1D elements
			V_f^{tow} (%): 80
			l (m): 0.002
			A^{tow} (m^2): 0.001
Fabric Types	V_f^{bulk}	$V_f^{bulk-adj.}$	$A^{tow-adj.}$ (1E-03 m^2)
Woven E-glass - WGa	40%	60.0%	0.0191
WGb	40%	60.0%	0.0191
Woven Carbon - WCa	35%	52.5%	0.0167
WCb	35%	52.5%	0.0167
Stitched E-glass 1 - SG1a	54%	81.0%	0.0387
SG1b	54%	81.0%	0.0387
Stitched E-glass 2 - SG2a	31%	46.5%	0.0148
SG2b	39%	59.1%	0.0188

For each experiment, a LIMS file of the mesh is created to match the experimental parameters. The viscosity, μ, of the test fluid is first input into LIMS. Then, V_f^{bulk} is set and K_{bulk}, which is determined from the experimental pressure profile over time, as discussed in the previous section, is assigned to the 2D elements. The 1D elements are next attached to each node of the 2D element mesh. The constant flow rate injection simulation is finally conducted in LIMS. The constant flow rate boundary condition is imposed at the edge nodes of the 2D mesh, which are along the width of the preform. The injection flow rate is divided over the sixty-one nodes along the width, ensuring that the corner nodes would see only half of the value the

edge nodes see. This implementation correctly models the linear injection that is initiated during the actual experiment.

In order to determine the micro-permeability parameter, the pressure and corresponding time data that is output from the simulation is matched to the experimental data. Only the simulation fitting parameter associated with the tow permeability, K_{tow}/h^2, is determined [18]. This fitting parameter lumps together the fiber tow permeability, the cross-section characteristic dimension of the fiber tow, h, which is equivalent to $l/2$, and possibly a shape factor of the fiber tow cross-section. The designation h from the analysis in [18] is equivalent to A^{tow} in the current analysis and the symbols can be used interchangeably. The actual permeability, K_{tow}, of the micro flow regions inside the tows is not evaluated. There are several arbitrary parameters preset in the simulation for the 1D elements, such as l and A^{tow}, which do not represent actual physical parameters of the fabrics used in the experiments. But, as long as the same input parameters are used in the simulation environment with the experimentally obtained value of K_{tow}/h^2, the macro- and micro-flow interactions can be properly modeled.

Initially, the K_{tow}/h^2 value of the 1D elements is estimated and assigned to these bar elements. The corresponding inlet pressure profile that is generated is compared with the experimental data. The next value is selected, by either doubling or halving the guess, depending on how the data from the initial guess plots against the experimental data. Figure 2.8 illustrates the two possible scenarios; case (a) shows the generated plot lies above the experimental plot, which corresponds to an initial guess that was too small and therefore must be doubled, while case (b) shows the opposite circumstance in which the generated plot lies below the experimental plot, which

corresponds to a guess that was too large and must be halved. The direction of increasing tow permeability is shown to clarify the choice, either doubling or halving, that needs to be made according on this bisection method.
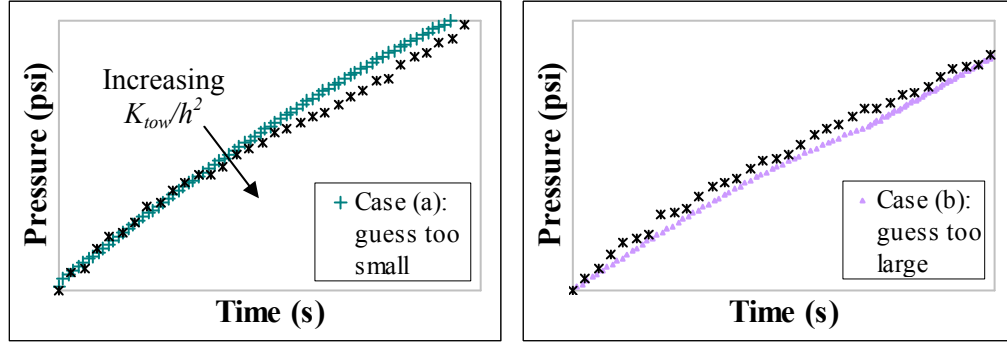
Figure 2.8: During estimation of the value of K_{tow}/h^2 two scenarios arise: case (a) the guess for K_{tow}/h^2 is too small and case (b) the guess for K_{tow}/h^2 is too large.

This iterative bisection process is continued until two curves, corresponding to two different tow permeability parameters, flank the experimental data curve. This resulting interval is then subdivided into multiple equally spaced segments. Each region is defined by a permeability parameter and the pressure and time data that corresponds to each value is generated. Multiple segments are generated, as opposed to purely bisecting the interval, so that the minimization location can be graphically verified.

The time, t_j, and the corresponding generated pressure data, $p^{num}(t_j)$, where j is from 1 to the total number of data points, N, is input into an excel template. The pressure values are first interpolated at each experimental data time step, so both sets of data can be compared at the same value of time:

38

$$p^{num}(t_{\exp}) = \left[p^{num}(t_j)\right]\left(\frac{t_{j+1}-t_{\exp}}{t_{j+1}-t_j}\right) + \left[p^{num}(t_{j+1})\right]\left(\frac{t_{\exp}-t_j}{t_{j+1}-t_j}\right). \tag{2.10}$$

The experimental time, t_{exp}, falls between the numerical time steps, t_j and t_{j+1}: $t_j \leq t_{\exp} \leq t_{j+1}$.

A simple point wise linear regression scheme is then implemented. The template is used to locally determine the set of numerically generated pressure data that best fits the experimental pressure data, p^{exp}. Still within the template, the difference in the pressures is taken at each time step, squared, and summed over the length of the experiment from $t_{exp}=0$ to t_f:

$$\sum_{t_{\exp}=0}^{t_f}\left[p^{num}(t_{\exp}) - p^{\exp}(t_{\exp})\right]^2. \tag{2.11}$$

The segment where this error is globally minimized is then identified. The new interval is further subdivided into equally spaced segments. The segments are progressively refined as the procedure is iterated in order to converge on the value of the tow-permeability fitting parameter.

2.5 Validation

The model of the 1D constant flow rate RTM experiment is used as a tool to validate the methodology for determining the macro permeability and the micro permeability parameter. Both of these values are chosen and assigned to the 2D and 1D elements in the finite element mesh, respectively. The 1D constant flow rate simulation is then performed using LIMS. The pressure plot is constructed as a function of time, by recording the pressure output by the simulation at an inlet node. This plot is then viewed as if it was obtained from a physical experiment.

This experiment is then processed, as if it were any typical physical experiment. The macro permeability is determined by using the slope of linear region (iii) of Figure 2.7, as discussed in the experimental procedure. The micro-permeability fitting parameter is determined by following the sequence of steps outlined by the flowchart in Figure 2.9. The values obtained for the macro permeability and micro-permeability parameter are then compared with the selected values to verify the methodology.
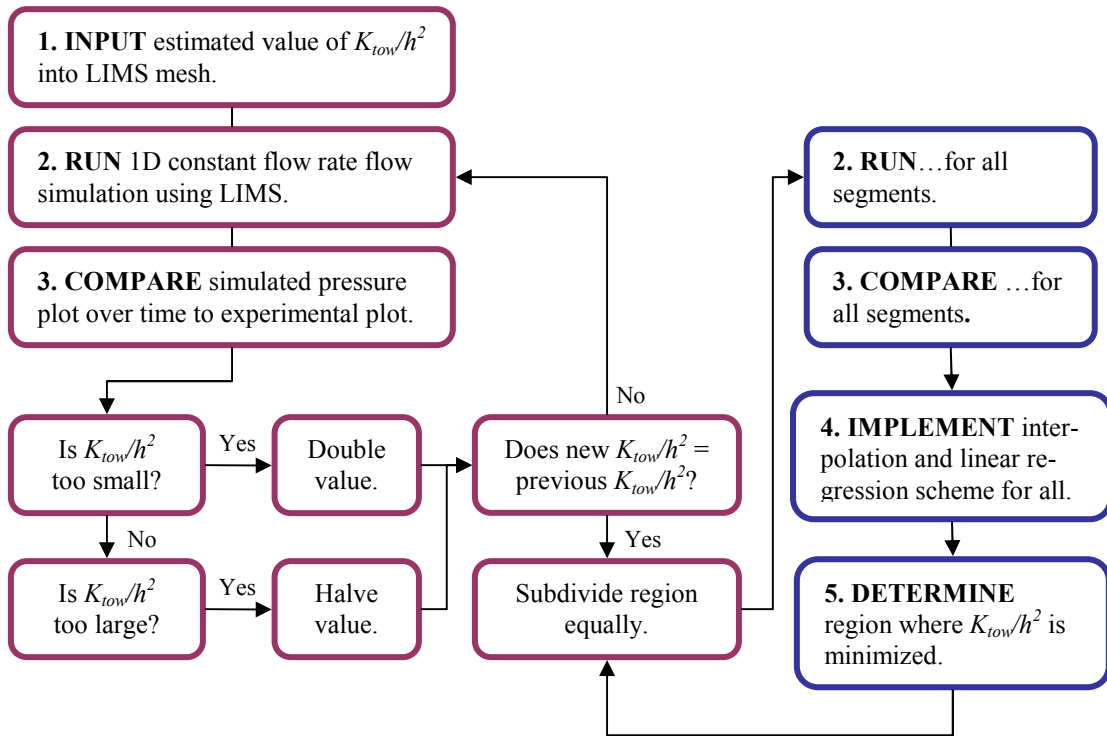
Figure 2.9: Flowchart of the procedure to determine the micro permeability parameter.

The methodology is tested for different ratios of permeabilities to ensure that it is sufficiently robust. The macro-permeability value is selected to be of the order of 1E-09 m^2. Permeability values of different orders, 1E-12 m^2, 1E-13 m^2, 1E-14 m^2, and 1E-15 m^2 are assigned to the 1D elements. This is done to ensure the methodology has the ability to recover permeability values, irrespective of the permeability ratio. Both values are exactly extracted when imposing the above methodology. One limitation, which is exposed, is that the values cannot be recovered if no tows fill with fluid, as in the case when the permeability value of the 1D elements is of the order 1E-15 m^2. This result corroborates the minimum requirement discussed in the numerical procedure: if the tows of the preform do not even begin to saturate, a saturated macro permeability can clearly not be determined.

2.6   Experimental results

Four fabrics are evaluated in this study: fiber mats of 9 oz/yd^2 biaxial woven carbon (WC), 24 oz/yd^2 biaxial woven E-glass (WG), and two types of biaxial stitched E-glass, 96 (SG1) and 18 (SG2) oz/yd^2 respectively. Different fabrics are evaluated to show how they deviate from a baseline single-scale medium and exhibit dual-scale behavior. Figure 2.10 highlights the different architectures of the four different fabrics.
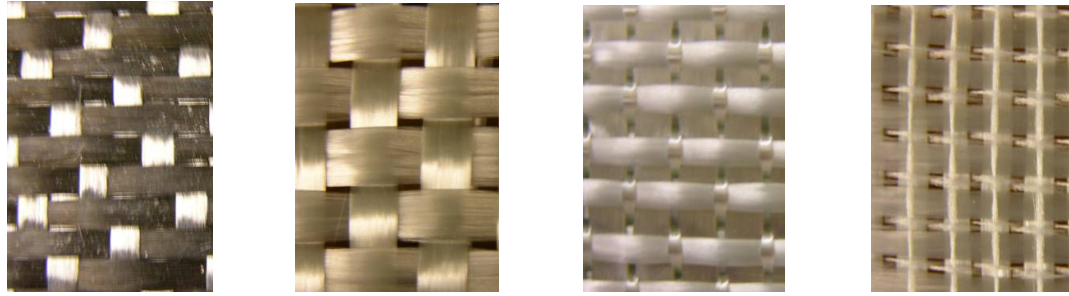
Figure 2.10: The four fabrics – 9 oz/yd^2 biaxial woven carbon, 24 oz/yd^2 biaxial woven E-glass, and 96 and 18 oz/yd^2 biaxial stitched E-glass – that are characterized.

Random mat fabric is included as a reference fabric, since it is known to exhibit a single-scale Darcian flow behavior. The random mat preform has only one length scale and accordingly exhibits a linear pressure profile. The woven and stitched fabrics have slight nonlinearities and bend away from the single-scale trend over the duration of the experiment, since these preforms have two length scales. The non-linearity is induced by the presence of the fiber tows, which act as sinks into which the fluid of the advancing flow front ingresses. The non-linearity in these preforms is slight, but not insignificant. This transition of the pressure from a linear, to a non-linear, and back to a linear profile, as is described in Figure 2.7 and as can be seen in Figure 2.11, enables the determination of the micro-permeability fitting parameter that can be used in LIMS to properly model the flow through different fabrics. The normalized plots for both the reference random mat fabric and an example of one woven E-glass fabric (WGb) are shown in Figure 2.11 to highlight the varying profile trends. The plots of all experiments, two – a and b – for each type of fabric, are subsequently discussed.
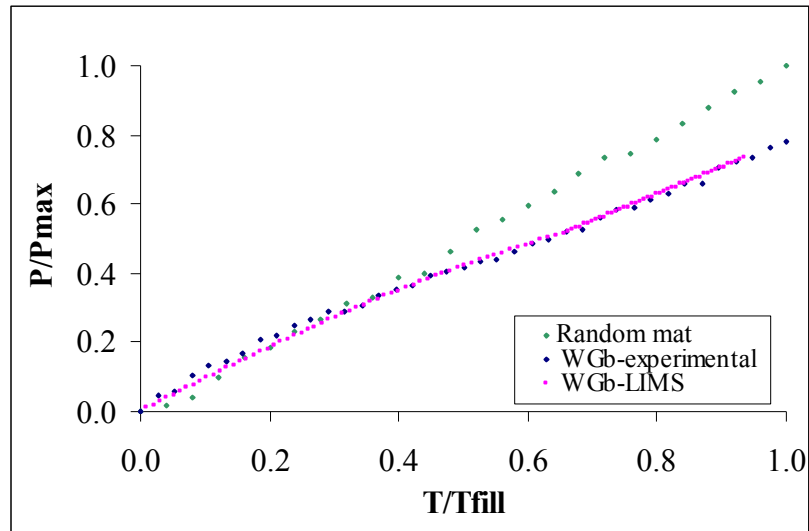
Figure 2.11: Woven glass fabric exhibits a non-linear pressure profile compared to a linear pressure profile of random mat.

Multiple experiments are performed for each type of fabric to evaluate repeatability. Four types of dual-scale porous media are characterized and the results of two experiments are included for each fabric. The normalized pressure profile results obtained from the 1D constant flow rate RTM experiments that are conducted, are compared with profiles output by LIMS, in order to determined the micro-permeability fitting parameter associated with each fabric.

The experiments that are conducted on the woven carbon, shown in Figures 2.12 and 2.13, exhibit the furthest fit from the LIMS model with an average absolute error or 4.38. However, this carbon fabric does correlate to the lowest area weight at 9 oz/yd^2 and, accordingly, the most repeatable experimental results, as shown in Figure 2.14.
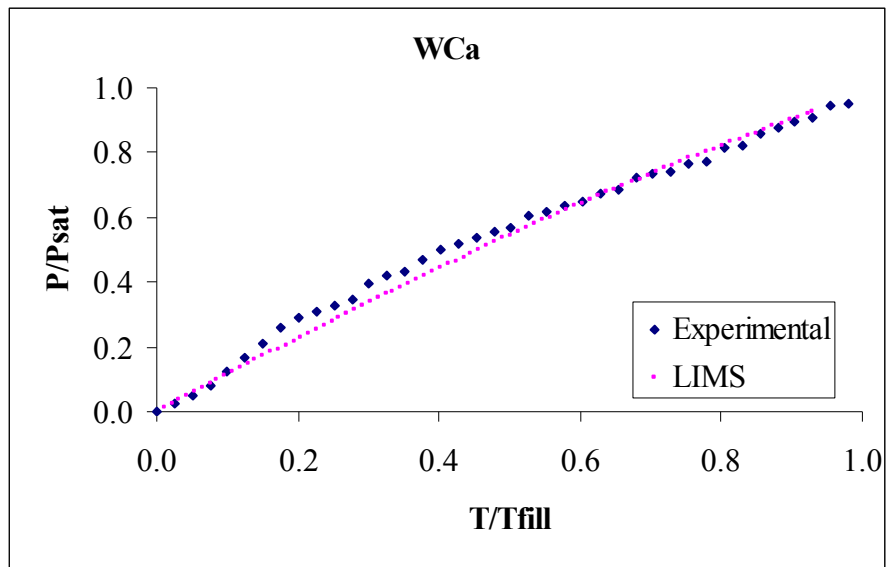
Figure 2.12: 9 oz/yd^2 woven carbon experiment a.
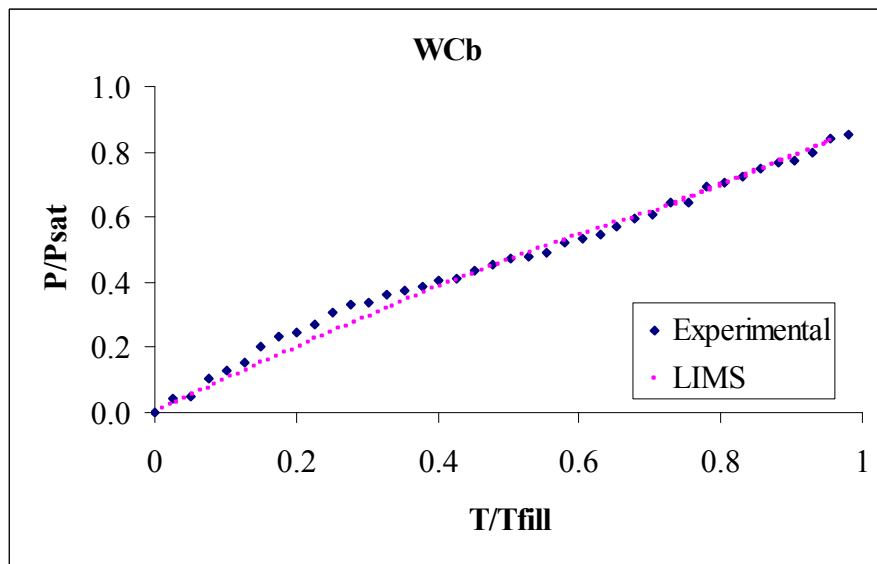
Figure 2.13: 9 oz/yd^2 woven carbon experiment b.
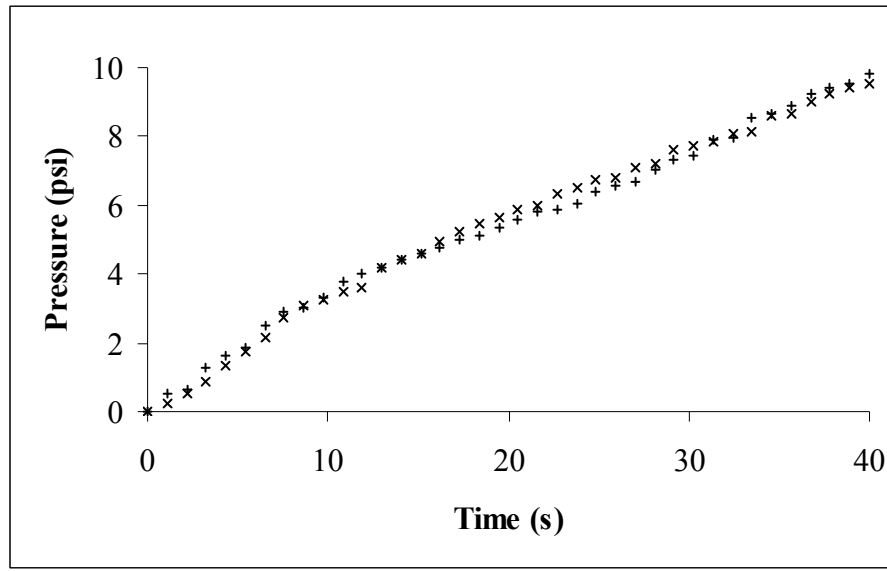
Figure 2.14: WC experimental results from Figures 2.12 and 2.13 are plotted together to show the least variability between experiments.

Subsequently, with an average absolute error or 1.45, the experiments conducted on woven E-glass, shown in Figures 2.15 and 2.16, rank next in the degree of fit to the LIMS model. This fabric shows greater deviations in repeatability, as is clear from Figure 2.17. The area weight is almost three times greater than the carbon at 24 oz/yd^2 and, consequently, the pliability and ability for the layers to easily and consistently mesh is reduced.
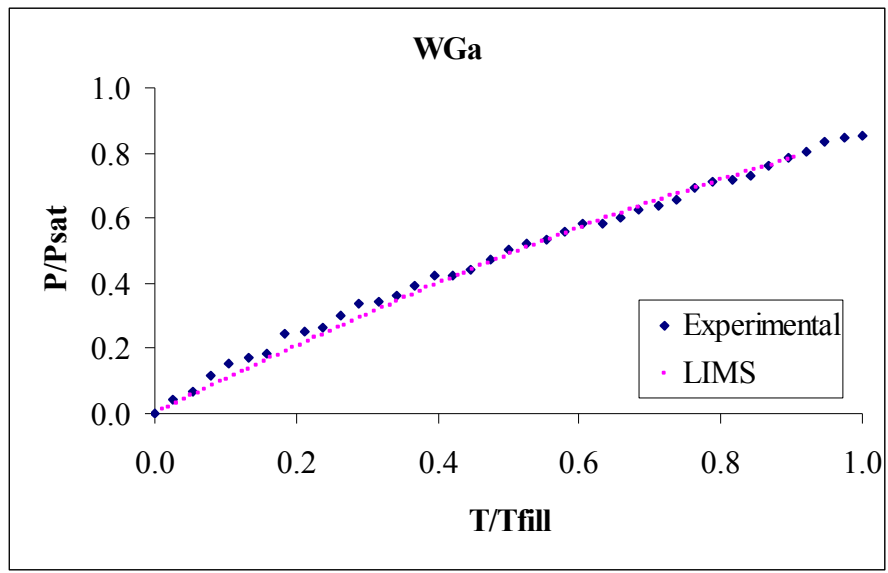
Figure 2.15: 24 oz/yd^2 woven E-glass experiment a.
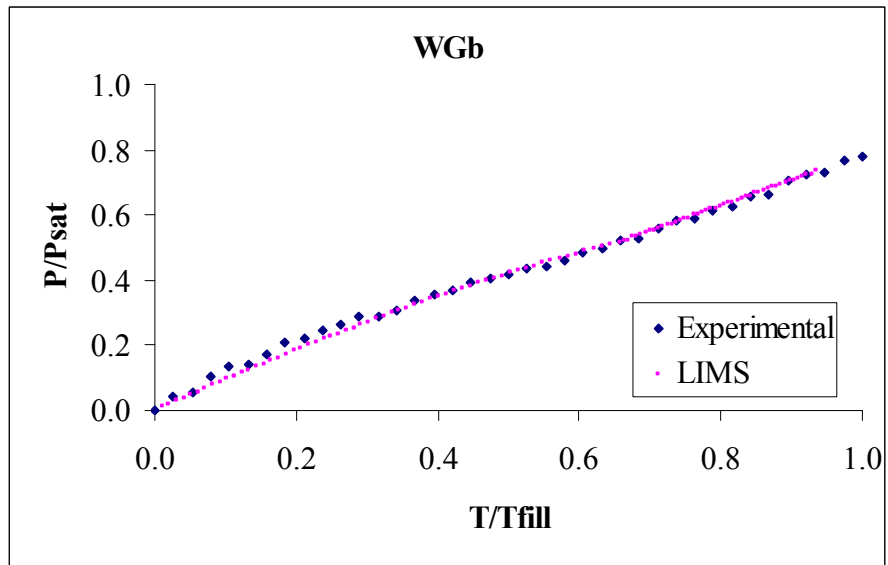
Figure 2.16: 24 oz/yd^2 woven E-glass experiment b.
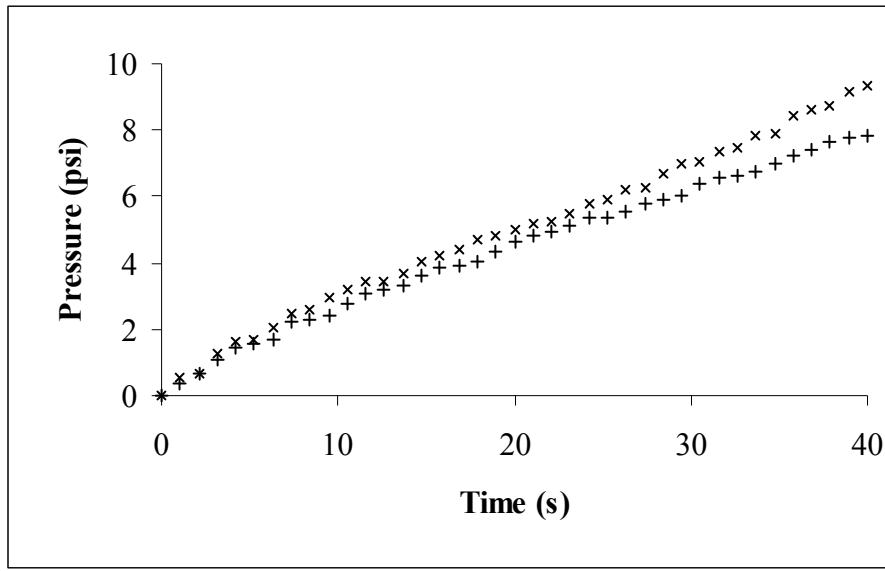
Figure 2.17: WG experimental results from Figures 2.15 and 2.16 are plotted together to show slightly greater deviations between experiments.

The stitched E-glass experiments in Figures 2.18 and 2.19 exhibit the best fit to the LIMS model, with an average absolute error of 0.26. But, the greatest variability between data sets is experienced, as shown in Figure 2.20. The area weight is over ten times that of the woven carbon and four times that of woven E-glass at 96 oz/yd^2 and, thus, the ability for the fabric layers to consistently mesh together is even further reduced.
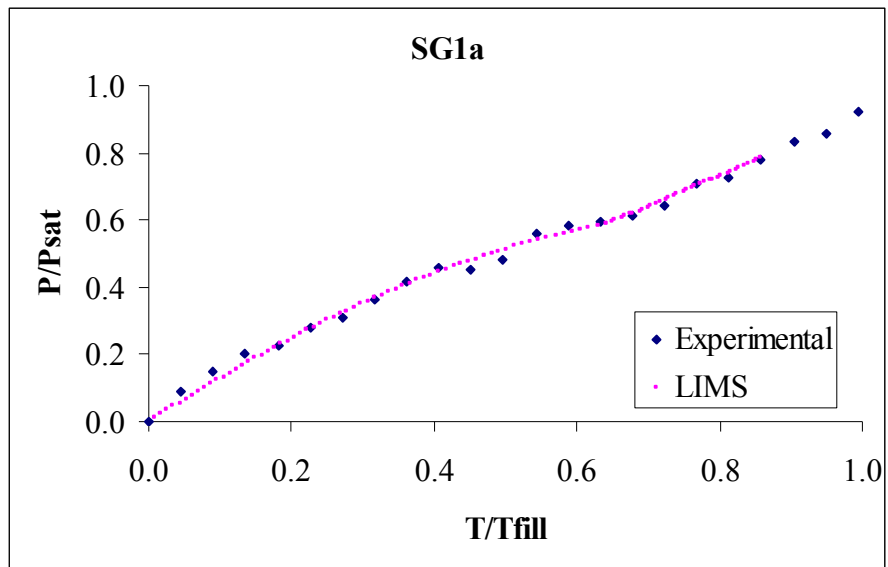
Figure 2.18: 96 oz/yd^2 stitched E-glass experiment a.
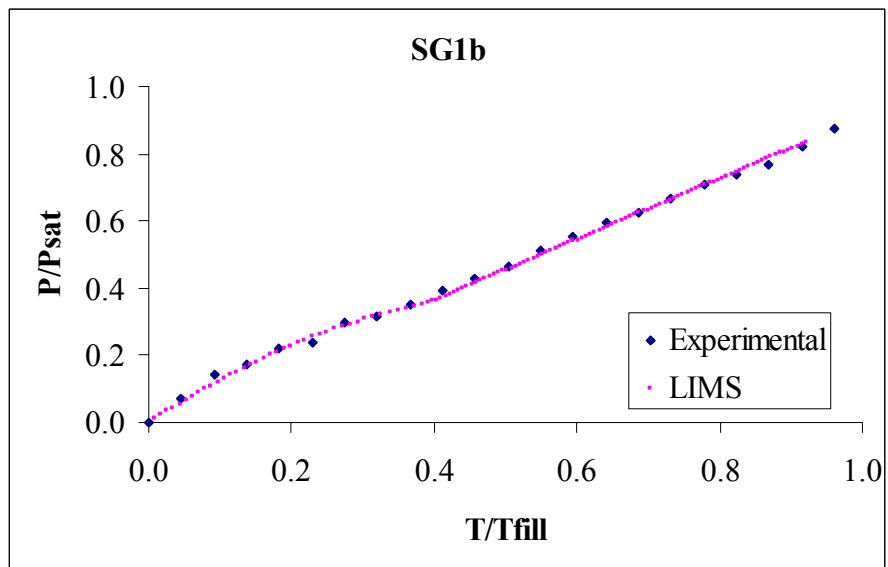
Figure 2.19: 96 oz/yd^2 stitched E-glass experiment b.
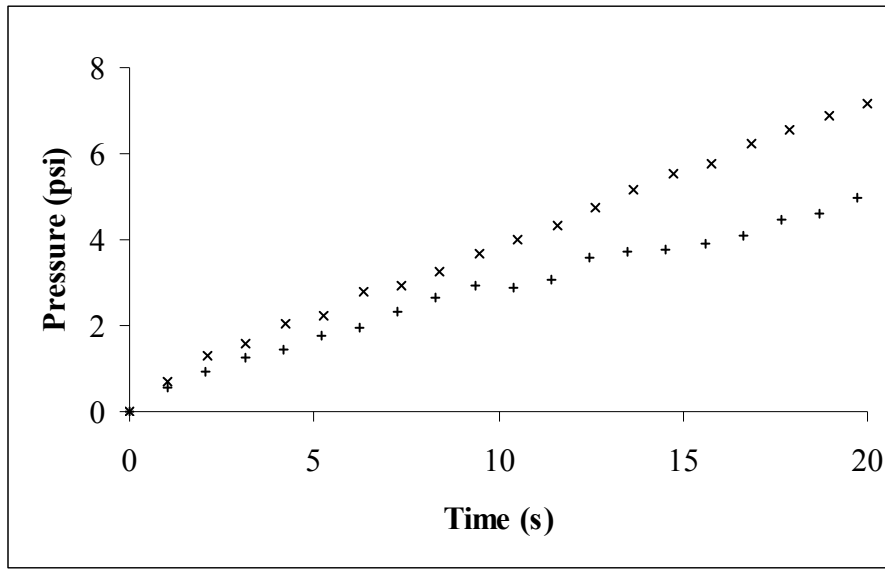
Figure 2.20: SG1 experimental results from Figures 2.18 and 2.19 are plotted together to show the greatest variability between experiments.

The final data sets depicted in Figures 2.21 and 2.22 provide a good fit to the LIMS model with an average absolute error of 0.55. The experiments are conducted on 18 oz/yd^2 stitched E-glass fabric at two different values of volume fraction, whereby different pressure profiles are anticipated, as the plots in Figure 2.23 show. The aim is to see how the micro-permeability fitting parameter changes for the same fabric, as the volume fraction and, therefore, the bulk permeability changes.
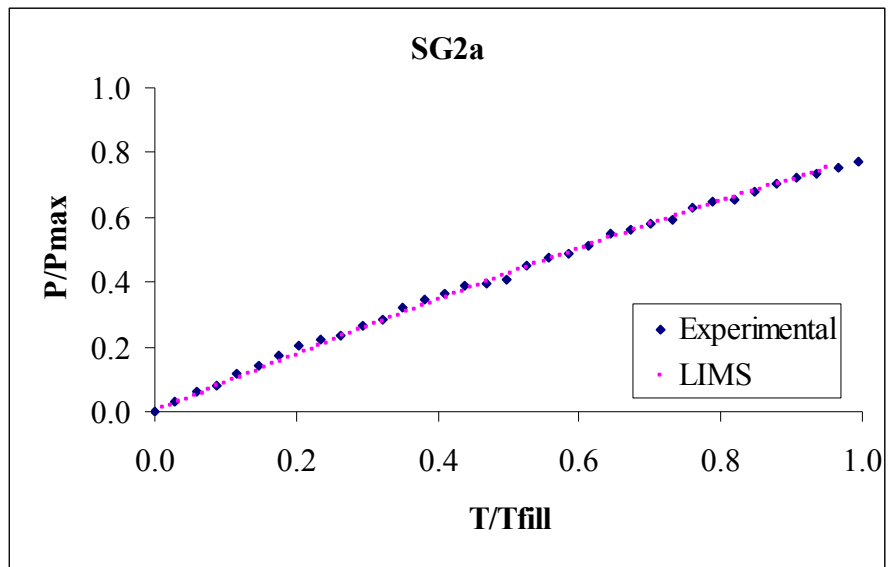
Figure 2.21: 18 oz/yd^2 stitched E-glass experiment a.
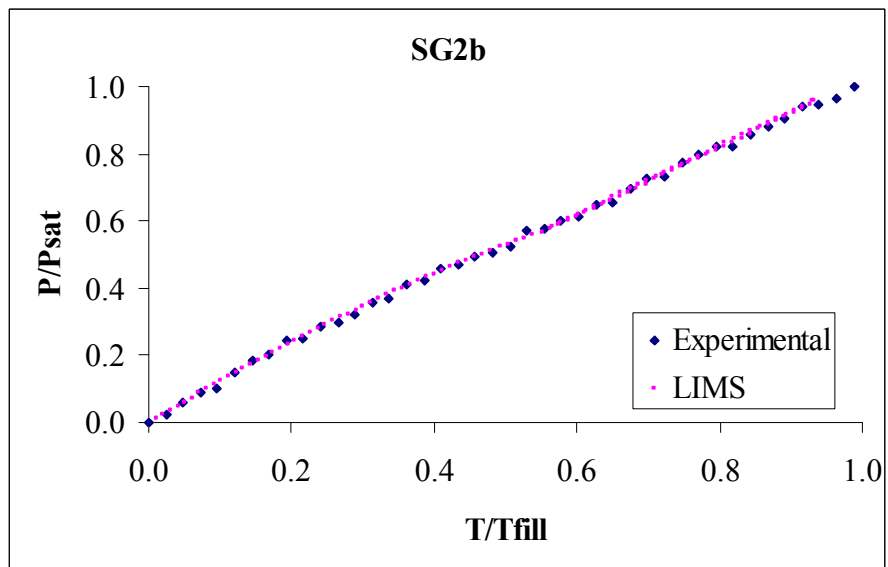
Figure 2.22: 18 oz/yd^2 stitched E-glass experiment b.
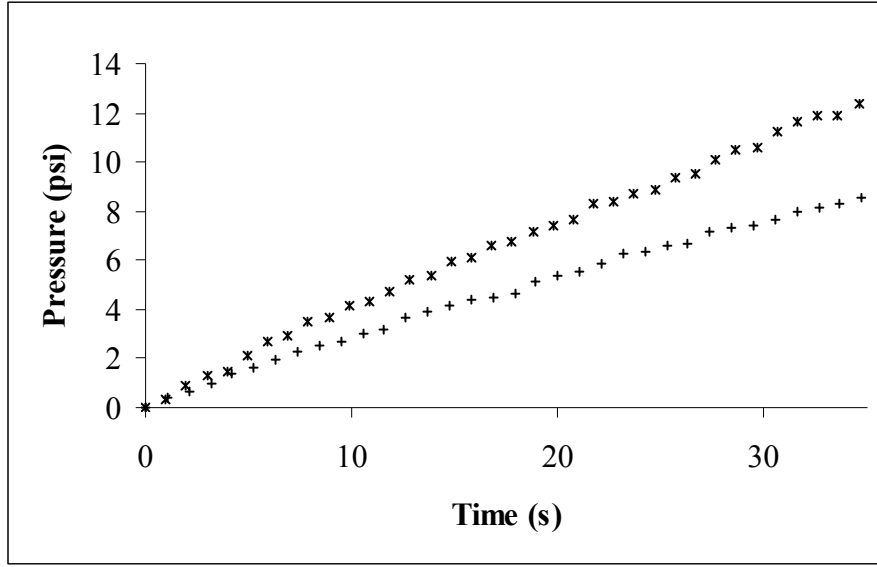
Figure 2.23: SG2 experiments from Figures 2.21 and 2.22 show anticipated variability, since two different volume fractions, 31% and 39%, are evaluated.

Table 2.2 outlines the macro permeability values that are determined from the preceding experimental plots, as well as the values of the micro-permeability fitting parameter that are obtained from matching the experimental data to the data output by LIMS. In addition, the value K*, which represents the ratio of the macro permeability to the micro-permeability parameter, is tabulated:

$$K* = K_{bulk}\left(\frac{h^2}{K_{tow}}\right). \tag{2.12}$$

The partially saturated length, Ls, generated by LIMS and a non-dimensional constant $\left(\dfrac{Ls^2}{K*}\right)$, which aides in addressing what parameters are impacting the partially-saturated length, are also incorporated into the results table.

51

Table 2.2: **Macro permeability, micro permeability parameter, K*, Ls, and Ls^2/K* results for each experiment.**

Fabric	V_f	K_{bulk} 1E-10 (m^2)	K_{tow}/h^2 1E-08	K* (m^2)	Ls (m)	Ls/L	Ls^2 / K*
WGa	40%	12.6	2.3	0.055	0.257	0.892	1.21
WGb	40%	10.7	3.7	0.029	0.188	0.653	1.22
WCa	35%	8.6	1.3	0.066	0.272	0.944	1.12
WCb	35%	8.3	2.3	0.036	0.199	0.691	1.10
SG1a	54%	20.6	8.6	0.024	0.210	0.729	1.84
SG1b	54%	14.2	15.5	0.009	0.129	0.448	1.82
SG2a	31%	12.7	1.8	0.071	0.267	0.927	1.01
SG2b	39%	7.2	3.3	0.022	0.163	0.566	1.22

2.7   Discussion

The data sets corresponding to the first three types of fabric (WG, WC, and SG1) are determined from experiments conducted at the same volume fraction. In the case of the stitched glass preforms, the macro permeability varies approximately 30%. This variation decreases to approximately 15% in the case of the woven glass fiber and is only a few percent in the case of the carbon fiber preforms. Other researchers have also reported that permeability values do achieve a large scatter from one experiment to the next [11, 13]. The pressure profiles of the two different experiments, from each of the three different fabrics, are plotted together in Figures 2.14, 2.17, and 2.20, to graphically show how the variability increases.

The way the fabric layers nest together plays an important role in these variances. Layers may end up placed either bundle to bundle or bundle to gap, as shown in Figure 2.24.
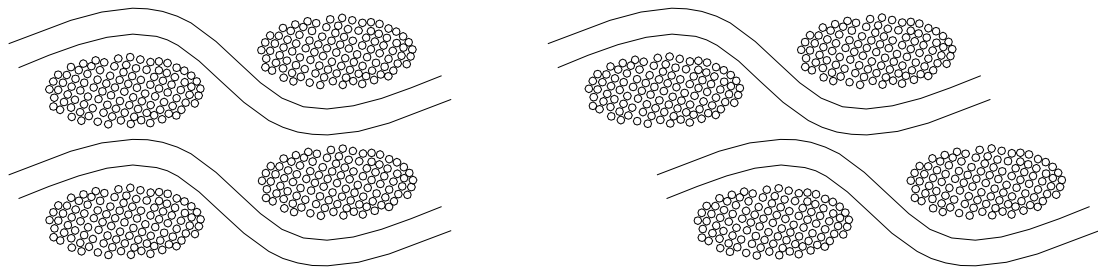
Figure 2.24: When fabric layers are placed together they stack either bundle to bundle or bundle to gap, creating different preferential flow paths.

One configuration may preferentially allow fluid to more easily permeate through the macro pores as compared to the other, which causes the deviations. In the case of the woven carbon, seven plies in the mold result in fiber volume fraction of 35%, where as only four plies of the woven E-glass occupy 40% of the mold. Deviations in stacking are thus not impacting the macro pores of the carbon to the extent the glass has the ability to be impacted. Accordingly, the glass is more permeable than the carbon, though there is less porous volume for the fluid to flow through. The thicker woven E-glass plies cannot mesh as well as the carbon plies, and more preferential macro flow regions are therefore likely to exist.

The first type of stitched glass preform (SG1) has seven layers that are already joined together; the tows of one layer are perpendicular to the tows of the preceding layer. This architecture is very different from the second type of stitched glass preform (SG2); the tows are again perpendicular to one another, but only two layers are stitched together. Thus, for the SG2 fabric, only two plies are needed to achieve a fiber volume fraction of 54% within the mold, whereas four and five layers of the SG1 fabric occupy 31% and 39% of the mold. The SG2 layers are accordingly less pliable and have much more freedom in how they nest, causing the greater macro

53

permeability deviations from one experiment to the next. Figure 2.25 highlights the difference between the 24 oz/yd^2 biaxial woven E-glass and the 96 oz/yd^2 biaxial stitched E-glass; the latter, with four times the area weight can clearly not mesh as easily as the former.

Figure 2.25: Woven and stitched E-glass, with 24 and 96 oz/yd^2 area weights respectively, highlight how much more difficult the latter is to mesh with multiple layers than the former.

The micro-permeability fitting parameter cannot be directly compared from fabric to fabric. The parameter is impacted by the size of individual fibers and fiber tows, the shape of fiber-tow cross-section, the volume fraction of the fiber tow, and possibly by some pre-set simulation parameters. Accordingly, the $A^{tow-adj.}$ values are different in the LIMS environment for each different fabric. But, the parameter can be compared between experiments for each type of fabric, since the experiments are conducted at the same volume fraction and the simulations are conducted corresponding to the same $A^{tow-adj.}$ parameters.

A trend which is exposed is that less permeable macro pores correspond to a more permeable parameter in terms of the micro pores. A hypothesis for this result is that as the oblong tows are compressed and become wider and thinner in cross

section, the macro pores are reduced in size. Thus, it is harder to infiltrate the macro pores, but the tows are able to fill more easily, since the fluid does not need to travel as far to reach all portions of the tow. A comparison of the tows of the four different fabrics is shown in Figure 2.26. The cross-sectional area varies due to the number of individual fibers that comprise each tow.
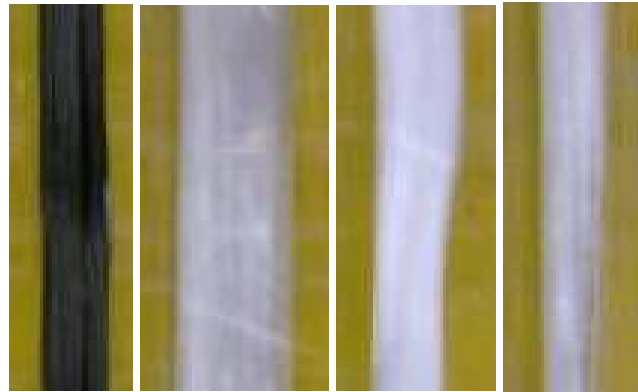
Figure 2.26: A comparison of the tow sizes for the four fabrics – WC, WG, SG1, and SG2 – that are characterized.

The second set of stitched glass fabric data (SG2), which is determined from experiments conducted at two different volume fractions, also demonstrates the trend that the micro-permeability parameter increases, as the bulk preform becomes less permeable. In this case, as the number of plies increases, the macro permeability also decreases as anticipated.

When comparing the permeability parameter relevant at the micro scale to an equivalent parameter pertinent at the macro scale, namely K_{bulk}/L^2, where L is the length of the preform, the ratio of the two values is of interest. Table 2.3 outlines the

separate values, in which the final data column reveals the ratio of the parameter from the micro to the macro region.

Table 2.3: **The ratio of the micro-permeability parameter to an equivalent parameter relevant at the macro scale reveals information regarding the time scales in the two different flow regions.**

Fabric	Kbulk (m^2) 1.E-10	Kbulk L^2	Ktow (m^2) 1.E-14	Ktow h^2	Ktow*L^2 h^2*Kbulk
WGa	12.6	1.5E-08	2.30	2.3E-08	1.51
WGb	10.7	1.3E-08	3.70	3.7E-08	2.87
WCa	8.6	1.0E-08	1.30	1.3E-08	1.25
WCb	8.3	1.0E-08	2.30	2.3E-08	2.30
SG1a	20.6	2.5E-08	8.60	8.6E-08	3.46
SG1b	14.2	1.7E-08	15.50	1.6E-07	9.05
SG2a	12.7	1.5E-08	1.80	1.8E-08	1.18
SG2b	7.2	8.7E-09	3.30	3.3E-08	3.80

This ratio reveals information regarding the different times scales in the two flow regions. The tows may need between 1.18 and 9.05 times as long to fill as the macro regions, depending on the architecture of the fabric. This ratio is important, as it alludes to necessary processing requirements of the different fabrics. Though these time requirements are not directly applicable for the characterization of the materials, they must be considered when resin is infused into the fabrics, so as to ensure all regions are saturated with fluid before the part cures.

As the macroscopic flow front progresses along the length of the preform, a region at the beginning exists in which at least 99% of the micro pores are saturated. Additionally, a region at the end exists where less than 1% of the micro pores are saturated. The region in between, is the partially-saturated region. As depicted in Figure 2.27, each shade correlates to a varying degree of saturation and the

combination of all shades represents the partially-saturated length, Ls, for each preform. This length identifies the region in which flow continues to ingress into the fiber tows and lies between one and ninety-nine percent saturation: $1\% < Ls < 99\%$.

The degree of saturation output from LIMS has the ability to be mapped to a contour plot, which is depicted in Figure 2.27. Ls can be clearly measured from the 99% to the 1% demarcation on the left side and right side, respectively. The values less than 1% are not included in the value of Ls, because they are deemed completely unsaturated, just as the values above 99% are not included, as they are considered completely saturated. This partially-saturated length is generated through LIMS since it is not possible to know exactly which regions are saturated to which degree from the current experimental set-up. The contour plots of all experiments are included in Appendix B (Figures B.1-B.8).
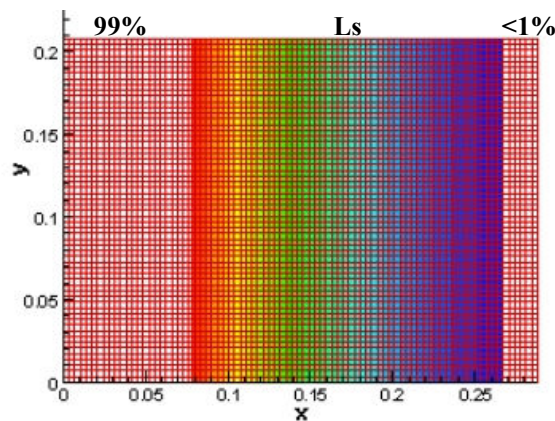
Figure 2.27: An example of a contour plot that enables the LIMS determination of the partially-saturated length, Ls, which is the region between 1% and 99% saturation.

If K^* increases, one would expect Ls to increase as well, as Ls will be impacted by changes in either the macro permeability or the micro permeability parameter. For example, if the micro permeability fitting parameter K_{tow}/h^2 is made smaller and smaller, Ls will increase, since K^* approaches a very large value. This is an anticipated result, since there should be a longer partially-saturated region as the micro-permeability parameter moves further away from the value of the bulk permeability. On the other hand, Ls will decrease as the micro-permeability parameter moves closer and closer to the value of the macro permeability. This result is again anticipated, since no partially-saturated length would be present in a single-scale medium.

The notion of the partially-saturated length provides valuable information about the experiments that are conducted. Ls^2/K^* is an important parameter since it remains steady for experiments conducted on the same type of fabric that have the same volume fraction. By knowing the partially-saturated length, along with the macro permeability of the bulk preform, the micro-permeability parameter can be obtained by using the knowledge that the Ls^2/K^* term is a constant for a specific fabric. As the general volume fraction in the mold increases, though the trend exists among the four different types of fabric that possess very different architectures, the Ls^2/K^* parameter also increases in general. Both the K^* vs. Ls/L and Ls^2/K^* vs. V_f^{bulk} trends arising from Table 2.2 are plotted in Figure 2.28.
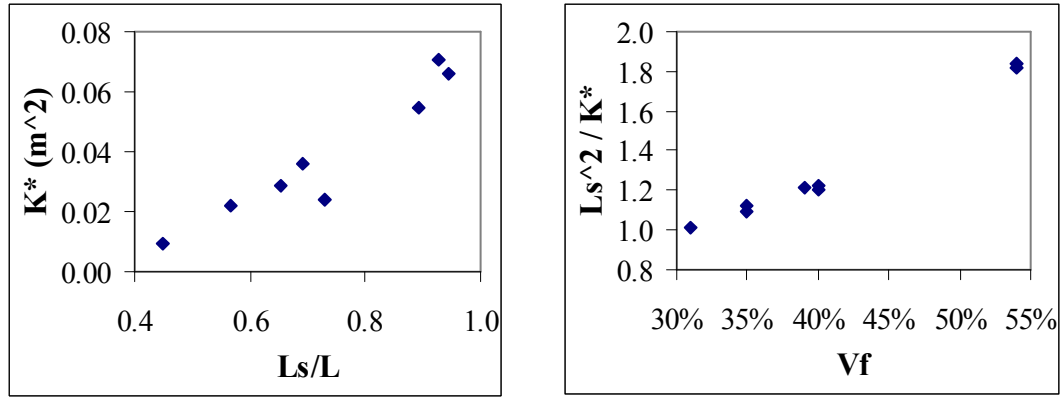
Figure 2.28: Non-dimensional trends exhibited by parameters *K** vs. Ls/L and *Ls²/K** vs. V_f^{bulk}, where Ls is a value output from LIMS.

The average summed absolute least squares error for each type of fabric are found to be 4.38 (WC), 1.45 (WG), 0.26 (SG1), and 0.58 (SG2) as previously mentioned. These results lead to the hypothesis that the experimentally obtained pressure profiles of the stitched glass fabrics provide the best fit for the model. It can be observed too, that the three fabrics with the lowest error are all comprised of E-glass. The carbon fibers within each tow have a smaller diameter, at 4-6 microns, than E-glass fibers at 9-12 microns [30]. Thus, there are smaller pores within the carbon tows, which may alter the sink strength in a manner not captured by the current LIMS model.

2.8 Conclusions

A methodology has been developed that determines both the macro permeability and micro-permeability fitting parameter for a fiber preform. The inlet injection pressure history of a 1D constant flow rate experiment is reproduced in the LIMS numerical analysis environment and the two profiles are compared. In LIMS,

1D elements represent the micro pores within the fiber tows and 2D elements represent the macro pores between the tows. The pores at the micro scale are much smaller and can not be infiltrated as easily as the pores at the macro scale. The model confirms with experiments that non-linear behavior is exhibited as a fluid, injected at a constant rate, flows into a dual-scale fabric in which the micro- and macro-scale permeability are different. This resulting nonlinear behavior is due to the way the fluid of the macro flow front enters the fiber tows at a delayed pace; the tows are accordingly considered fluid sinks. The gathered experimental data, along with generated LIMS data, couple the macro- and micro-flow interactions, which are so crucial in dual-scale preforms used in many LCM applications.

2.9 Limitations

The permeability characterization study is developed and conducted based on the established tow saturation script that serves as an extra simulation tool to complement LIMS [18, 32]. Once the macro permeability is determined from the experimental pressure profile, the constructed LIMS model is used to characterize the micro permeability, whereby certain limitations are revealed. As discussed in 2.4, the actual value of the micro permeability is not directly determined. A fitting parameter associated with the tow permeability, K_{tow}/h^2, results due to the way the value is linked to the 1D parameters set in the LIMS environment. Several parameters linked to the fiber tow are not representative of actual physical parameters, so the associated variability is lumped into the tow-permeability parameter.

The micro-permeability fitting parameter values that are obtained are still important, in that if the same 1D element parameters are set for future LIMS simulations, the flow can be accurately modeled. The interest remains in additionally

having a solution that can directly expose the relationship between the macro and the micro permeability. The actual physical parameters of the fiber tows are ideally incorporated, so that the sink affects occurring for different fabrics with different size tows are accounted for on a case by case basis. For these reasons, a model is developed to quantify the flow in the three regions depicted in Figure 2.7 analytically, so the *actual* value of the micro permeability can be determined.

The experimental and simulation results are compared to the results from the analytical model, to verify that the exhibited pressure profiles and trends are in line with the actual flow physics and match one another. Appendix C steps through the equations that are uncovered for the model that is used. Plots are constructed to graphically highlight the resulting analytical curves to which the experimental and LIMS data are compared. Examples of both types of stitched biaxial E-glass fabric are included in Figures 2.29 and 2.30, to highlight the good agreement that is shown between all three methods.
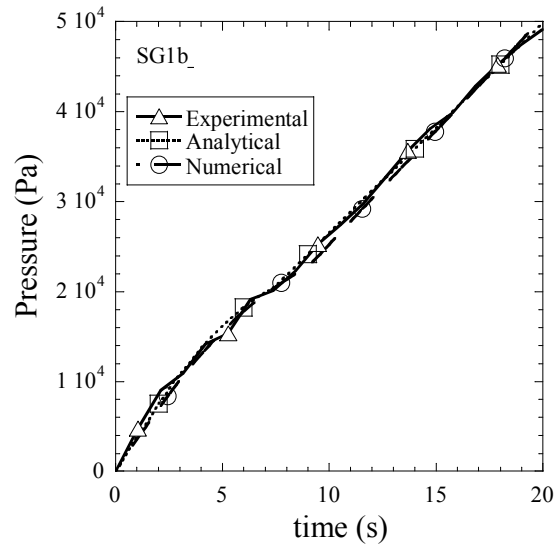
Figure 2.29: The experimental, analytical, and numerical solutions have good agreement, as shown for SG1 E-glass fabric.
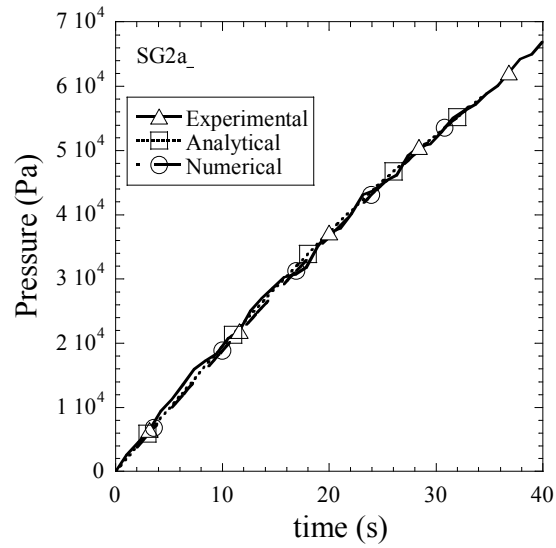
Figure 2.30: The experimental, analytical, and numerical solutions have good agreement, as shown for SG2 E-glass fabric.

Additionally, the analytical model confirms the requirement that the partially-saturated length is constant during region (iii) of Figure 2.7. This length can be analytically expressed as:

$$Ls = \sqrt{\frac{K_{bulk}\, h^2}{K_{tow} \cdot a \cdot V_f^{tow}}}\, \cosh^{-1}\left(\frac{1 - V_f^{bulk}}{1 - V_f^{tow}}\right).$$ (2.13)

This equation clearly shows that Ls is a constant that increases with the bulk permeability, if the tow permeability remains constant, and decreases with tow permeability, if the bulk permeability remains constant. It is anticipated that no partially-saturated length (Ls = 0) will be present in a single-scale medium ($K_{bulk} = K_{tow}$ and $V_f^{bulk} = V_f^{tow}$), which is explicitly revealed by Equation (2.13).

A non-dimensional parameter $\left(\dfrac{Ls^2}{K*}\right)$ is also evaluated and concluded to remain constant for experiments conducted on the same type fabric that have the same volume fraction. The same conclusion can be reached from the analytical model:

$$\frac{Ls^2}{K^*} = \frac{\cosh^{-1}\left(\dfrac{1 - V_f^{bulk}}{1 - V_f^{tow}}\right)}{a \cdot V_f^{tow}}.$$ (2.14)

Chapter 3

CORRELATION OF VOID DISTRIBUTION TO VARTM MANUFACTURING TECHNIQUES

3.1 Introduction

The VARTM process is one in which resin is pulled through a dry fabric preform by the application of vacuum pressure. The initial air that exists within the preform is expelled in preparation for injection; to do so, the inlet line remains closed as a vacuum is drawn on the system. As the inlet line is opened, a pressure gradient is created, which drives the resin to impregnate the fibers. The ultimate goal of VARTM is to fill all regions devoid of resin, which exist between the fiber mats, between the fiber tows, and within the fiber tows, with resin. As the architecture of the preform becomes more complex, the ability to fill every region becomes increasingly difficult.

Single-scale fibrous porous media constitutes the most straightforward types of fabric since no significant fiber bundles are contained therein. This type of fabric is purely composed of randomly oriented fiber bundles that have a small diameter, in which the space between the bundles is of the same length scale as the actual bundle. Once fiber bundles of a significant diameter become a part of the architecture and are either woven or stitched together, the structure of the fabric clearly becomes more complex. This type of media is considered dual-scale, since two regions exist that have very different properties: the macro-flow region between the fiber tows and the micro-flow region between the individual fibers within the tows.

Key parameters that vary between the macro to the micro regions are the permeability and the porosity. The empty regions within a bundle of tightly packed fibers are on the scale of microns and difficult to impregnate with resin. The gaps between the tows are on the scale of millimeters and, accordingly, more porous and permeable; thus, these regions are easier to impregnate with resin. The macro regions often act like channels, a designation that highlights the relative ease with which the resin flows through these areas. On the other hand, the resin has a harder time flowing between the tightly packed fibers within each tow that ultimately comprise the "walls" of these channels. If the channel flow is faster than the flow into the tows, the resin reaches the vent before all the tows are filled, forming voids *within* the tows [16, 17, 20, 23, 33, 34]. Altering the processing technique of the fabric preforms results in the reduction in the amount of these unwanted micro voids.

Due to the parameter variances in the two different macro- and micro-length-scale regions of the fabric, a resin-bleeding practice has been adopted for VARTM processing of such dual-scale fabrics. By employing this technique, the resin that is injected continues to flow through the preform and into the vent line even once the visible flow front reaches the vent line. This way, the fiber tows, which have a much lower permeability than the bulk fabric, are given additional time to fully saturate with resin. This concept of bleeding is definitely warranted [35], but a difficulty remains in determining how much resin to bleed to ensure all regions are infiltrated with resin.

An alternative processing modification is to add a resistance at the vent location, which helps to reduce the filling time and the amount of resin wastage due to bleeding. The added resistance attached as an appendage at the vent slows the

bleeding rate of the resin; it also provides higher pressure and residence time for the resin to permeate all regions of the preform. Tubing that has a smaller diameter or additional layers that are porous but have a low permeability, are attached to the vent. Then, the resin pressure within the mold can drive the resin into the micro spaces between the fibers within the fiber tows of the preform. A similar difficulty arises in determining how much resistance should be added to ensure all areas are fully saturated with resin.

Both techniques are options for fabricating parts with VARTM that hope to eliminate or reduce the voids that are created by the different length scales inherent in dual-scale fiber preforms. If the chosen manufacturing techniques do not incorporate provisions to fill even the micro regions, gaps remain within the preform, which constitute voids. The fabrication method also affects how voids are distributed along the length and through the thickness of the part. Voids can be induced in specific directions due to preferential flow paths created by the manufacturing process [36]. Depending on where strength is specifically needed, the role of the manufacturing technique is clearly very important. Depending on the method of fabrication, variances exist in the amount and distribution of voids, and, therefore, in the part quality. Defect-free composites are in effect not attainable, but the interest in quantifying any defects that are manufactured into or simply not expelled from the part remains. A comparison parameter should be available among processes, so that the most effective process can be determined.

The chosen process can also be modeled numerically by conducting flow studies using LIMS. The VARTM process necessitates four different permeability values to be assigned to the mesh used in the simulation, in order to properly represent

66

the flow. These values include the permeability of the fabric in (i) the flow direction and in (ii) the direction transverse to the flow; also, the permeability values are needed of (iii) the fiber tows and of (iv) the distribution media (DM) that is used to enhance the flow in the plane of the composite part. These values need to be determined prior to the numerical analysis by conducting both RTM and VARTM experiments, so that the complete permeability values can be characterized [4, 37]. Applying the determined fabric permeability properties of the macro pores surrounding the fiber network to the 2D elements of the mesh and of the micro pores within the actual fiber tows to the 1D elements of the mesh is very important; these values are non-uniform and thus induce regions that are susceptible to the formation of voids.

The distribution of these voids is clearly of interest, especially when fabricating panels with VARTM, since the preform starts out completely dry and ideally should end up fully saturated with resin. Yet, due to fabric architecture, the way the preform is processed, and the inherent variations of the lay-up technique and the preform, voids within the plane of the fabric, as well as through the thickness can remain. If only a single layer were being used to create a panel using an LCM process, only in-plane voids would be of interest; but, most fabricated panels are comprised of multiple fabric layers that are stacked together. In this latter situation, the in-plane void formation is still relevant, but voids are also formed through the cross-section of the panel [34]. The variations that exist from the DM side to the tool side of the panel can be seen when cross-sections of the panels are analyzed using image analysis techniques.

This portion of the study investigates how altering the manufacturing process of composite panels impacts the void content variation through the thickness

and along the length of the different panels. Slightly varying the process conditions can have a significant impact on void content and distribution in the final composite [36]. Understanding where the voids are formed becomes a necessary and important task, since the location will play a big role in the way the manufacturing process is designed, as dictated by the application of the part.

3.2 Background

The flow advancing through fibrous preforms is very complex in nature, because of the intricate geometries that exist due to the way individual fibers and bundles of fibers, i.e. the tows, mesh together on both the macro and micro scale. Because of these complexities, void formation mechanisms are still not completely understood, but the desire to control the presence of these voids remains.

A primary way voids originate is from the entrapment of air during lay-up or impregnation. The voids can be due to resin mixing operations or due to wrinkles or pockets that are created during the lay-up [36]. Voids can be entrapped in the macro, inter-tow spaces and, if so, are called matrix voids, or in the micro, intra-tow spaces, and, if so, are called preform voids; these cases occur due to stronger capillary and viscous flow, respectively [1]. This interpretation stems from evaluating the modified capillary number, Ca*, which is the ratio of the viscous forces, μv_{ff}, where μ is the viscosity of the resin and v_{ff} is the flow-front velocity, and the capillary forces, $\gamma cos\theta$, where γ is the surface tension of the resin and θ is the contact angle.

Using such phenomena to understand the mechanisms of the presence of voids enables effective methods to be developed in order to begin to understand and control void formation. Experimental techniques with which the void content can be visually detected offer ways to quantitatively establish the amount of voids, either

absolute or relative, present within an actual composite part. Different methods exist, both non-destructive and destructive, to determine these void contents.

Ultrasonic inspection is the most used non-destructive technique to detect defects [38]. This method is used to measure the porosity levels corresponding to the amplitude intensity used during the ultrasonic scan. Researchers [38-40] determine if the level of voids is acceptable, based on the application of the part; a void content of one percent or less is tolerable for high performance applications, while five percent is tolerable for other applications [38].

Microscopic image analysis is among the most accurate destructive methods to measure void content [1]. The size, shape, and spatial variations can be uncovered by researchers [1, 38-41] once machined composite sections are potted or mounted, the surface of interest is polished, and the samples are inspected. An optical microscope equipped with a camera and an image processing system is used to inspect and photograph the samples at 200X magnification [1, 38], which enables voids the size of the radius of a single fiber to be detected.

Image analysis techniques are vital, since the distribution and amount of voids can be physically seen and correlated to the processing conditions employed during manufacturing. The common aim is to optimize the manufacturing technique in order to minimize the void content. The relationship between various processing parameters and the resulting void contents are studied to uncover any relationships that may exist. A comparison of the relative void content offers an understanding as to why certain manufacturing methods induce fewer or more voids. Defect-free composites are practically impossible to manufacture and it is not imperative to

eliminate all of the voids that may exist; but, it is important to minimize the void content and keep the laminate uniform [42].

3.3   Experimental methods

One fabric, which is evaluated in the RTM permeability study [37], is chosen with which to conduct the current VARTM void formation and distribution study. SG1 fabric, which is a seven-layer, bi-axial, stitched, 96 oz/yd^2 E-glass, is used to manufacture four different composite panels. Each panel is comprised of two plies of the chosen fabric and fabricated with the VARTM technique explicitly outlined in 1.2. The fabric layers, which are cut seven inches in width and ten inches in the flow direction, are placed and processed on the simplest form of mold tool: a flat, table-top surface. The vacuum pulls prepared 411-350 Derakane Vinyl-Ester resin, which contains 0.2% by weight of cobalt naphtheenate as the accelerator and 2% by weight of Trigonox 239A as the initiator, into the preforms. The vacuum removes the air, compacts the fabric, and creates a pressure difference to drive the resin into the spaces between the fibers.

A baseline case is manufactured in which no resin is allowed to bleed (NB) through the vent-side tubing and no vent-side resistance (NR) is used. The injection process is halted by clamping off the inlet line once the resin reaches the vent line, which occurs in approximately two minutes. The panel is then allowed to cure at room temperature overnight. Three successive variations of this baseline process are employed to fabricate panels that will then be compared with the baseline in terms of void content and distribution.

The first variation that is employed in the process is one in which the resin is allowed to bleed (B) through the vent-side tubing once the resin reaches the vent,

without attaching any additional resistance at the vent. The resin is allowed to bleed for a time-frame equal to two times the time it takes the resin of the baseline case to reach the vent; the total time the inlet line is open accounts for approximately six minutes. An amount of time, versus a volume of resin is chosen, due to the small panel that is constructed, for which the overall volume of resin needed is small at just 100cc. The implications of cycle time are thus of more interest than resin wastage.

The second variation of the process adds a resistance (R) to the vent side of the panel in the form of smaller diameter tubing. The diameter of the initial tubing is ⅜" and the resistance tubing is less than one-third of this diameter. The resistance tubing is stepped down via a connector, as shown in Figure 3.1. A length of twenty inches is used to provide ample reduced cross-section and volume through which the resin flows and for which the resistance can still make an impact. The injection is discontinued once the resin reaches the end of the attached additional tubing that serves as the resistance at the vent.
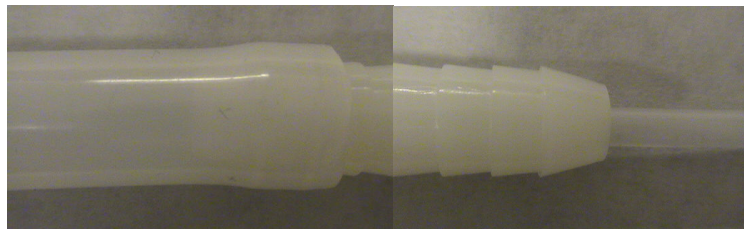
Figure 3.1:   The resistance that is added is in the form of smaller diameter tubing, stepped down via a connector.

The final variation of the process combines the first and second variation and allows resin to bleed through the resistance, following the same time-frame guidelines as previously mentioned.

In addition, one thick-sectioned composite (T), fabricated from six layers of the same fabric, is manufactured. This extension to the analysis is included in order to see if the void distribution is exacerbated as the number of layers is increased. This panel is manufactured using the baseline processing conditions in which no additional resistance is added and no resin is allowed to bleed. A summary of all of the manufactured and evaluated cases is presented in Table 3.1.

Table 3.1: **Five different cases of VARTM-fabricated composite panels are manufactured, evaluated, and compared.**

	Cases		Key	
1	NB - NR		N	No
2	B - NR		B	Bleeding
3	NB - R		R	Resistance
4	B - R		T	Thick-Sectioned
5	NB - T			

NB-NR: **Baseline case, where *no* resin is allowed to bleed from the vent, which has *no* additional resistance attached to it.**
B-NR: **Variation from the base line case, where resin is allowed to bleed from the vent, which has *no* additional resistance attached to it.**
NB-R: **Variation from the base line case, where *no* resin is allowed to bleed from the vent, which has additional resistance attached to it.**
B-R: **Variation from the base line case, where resin is allowed to bleed from the vent, which has additional resistance attached to it.**

After the composite panels are manufactured with the final dimensions of ten inches in length and seven inches in width, two specimen locations are selected. Specimens from three and nine inches from the injection line are machined from each panel. These samples are taken from the central region of each panel, as shown in Figure 3.2.
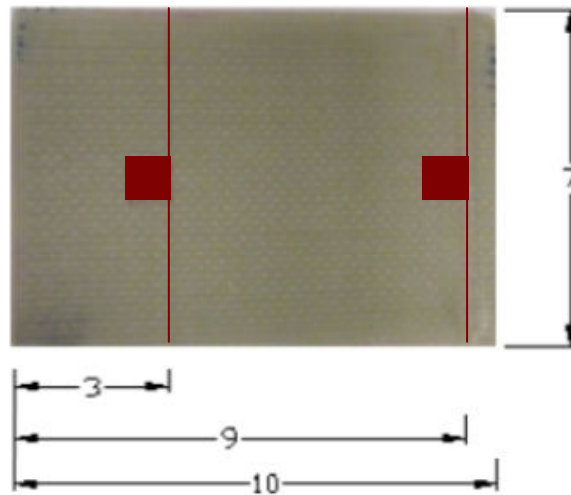
Figure 3.2: A top view representing the fabricated composite panels highlighting the locations, 3 and 9 inches along the length, from which samples are machined – all dimensions are in inches.

These samples are potted in Epo-kwick epoxy overnight. The new epoxy samples containing the composite sections are then polished using a polishing wheel and a progression of sandpaper and aluminum-oxide particles, to a final tolerance of five microns. The polished samples are then viewed at 200X magnification using an optical microscope. This microscope is equipped with a camera, in order to photograph images through the cross-section. Image analysis software is then used to

gather data to quantify the relative void content of the ten samples. A certain light intensity is chosen for all of the samples, and a specific grayscale threshold is selected with which to compare one panel to another and one panel location to another. The voids have a distinct color difference compared to the surrounding fibers and resin; they are very dark, as shown in Figure 3.3, which is why a relative comparison can be conducted.
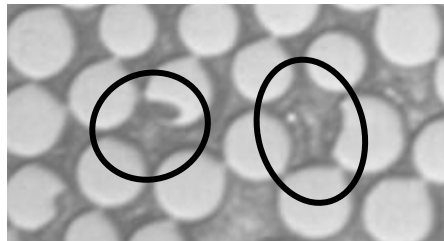
Figure 3.3: **The voids found within the composite samples are evident from image analysis; the voids represent the darkest regions of the photo, which are circled, and are of the size of an individual fiber.**

But, the exact grayscale threshold chosen is subjective; therefore, an absolute measure of the void content is not made. In this study, only a relative comparison is used to illustrate the effect the employed manufacturing technique has on the void content and distribution.

Sets of seven images are taken through the thickness of the samples, from the DM to the tool side of the panel. The void content found for each image is averaged, as well as plotted through the thickness, to see the variances not only among samples, but within each sample.

3.4   Use of flow simulation to predict void content and distribution

LIMS [32] is used in order to compare the experimental findings with fiber tow saturation predictions using a numerical simulation. The 1D constant pressure VARTM experiment that is conducted is modeled in order to simulate the experimental conditions and parameters. Fill-time data is generated over the course of the injection and void data is uncovered. A rectangular mesh representing the cross-section along the length of the manufactured panels is created to replicate the VARTM preform fabricated in the experiments. This mesh consists of rectangular 2D elements, of which the dimensions are achieved by satisfying the following aspect ratio criterion:

$$\sqrt{\frac{K_{trans}}{K_{flow}}} \frac{l_{flow}}{l_{trans}} \approx 1, \tag{3.1}$$

where K_{flow} is the permeability in the flow direction that corresponds to the value along the length of the panel and K_{trans} is the permeability in the direction transverse to the flow that correlates to the value through the thickness of the panel. The length of the individual 2D elements in the flow and transverse directions are l_{flow} and l_{trans}, respectively. The mesh size is eighty-two elements in length by twenty elements in width.

These 2D elements are assigned a permeability value in both the flow direction and the direction transverse to the flow within LIMS. Both values correspond to the macro-impregnation regions of the preform. The value of K_{flow} that is implemented is taken from the average of the 1D RTM experiments previously conducted for SG1 fabric, the values of which are tabulated in Table 2.2. The value of K_{trans} that is used is concluded by conducting a 1D VARTM experiment. The time is noted when the corn syrup, which is used as the test fluid, reaches a location along the length of the panel on the DM side, as well as on the mold-tool side of the panel. The

experiment is conducted on a clear acrylic sheet, to enable these flow locations to be viewed and determined. The determined arrival-time data is input into a permeability estimation algorithm, which takes this gathered information on the lead length, as well the established permeability value in the flow direction, and outputs the permeability values of interest – K_{flow} and K_{DM}. The specifics of the basis of the algorithm are detailed in [4].

One-dimensional bar elements are then attached to every 2D element node. These 1D elements are assigned a permeability value, K_{micro}, representing the micro-impregnation regions of the preform, i.e. the fiber tows. By the addition of these 1D elements to the existing 2D elements, the interaction between the macro- and micro- flow regions is enabled [18]. The value of K_{micro} that is implemented is taken from the average of the SG1 fabric values previously characterized, the values of which are also tabulated in Table 2.2.

One-dimensional elements are added between fifty-four of the eighty-three nodes along the top of the mesh, to simulate the DM that is used when manufacturing the panels, and assure this portion of the processing is also represented. The DM does not extend along the entire length of the panel, but only along sixty-five percent of the length, to represent the conditions employed in the experiments; this is why only fifty-three additional 1D elements are added. These 1D elements are also assigned a permeability value, K_{DM}, which is also determined from the data input into the permeability estimation algorithm expressed in [4], as discussed above. Figure 3.4 displays how the four permeability parameters are assigned to the different 1D and 2D elements of the mesh.
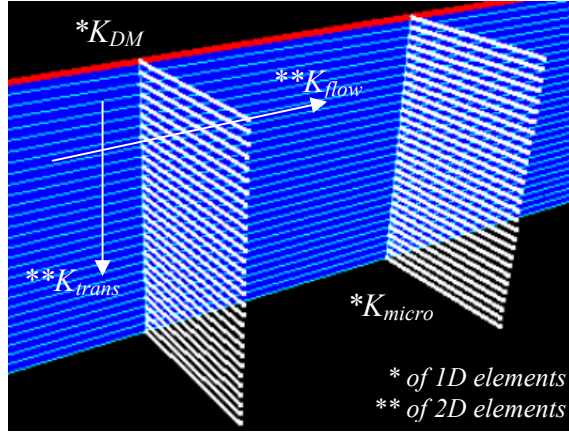
Figure 3.4: **Four permeability values K_{flow}, K_{trans}, K_{micro}, and K_{DM} are needed to define the 2D and 1D elements of the mesh, so one can simulate the flow in bidirectional preform in a VARTM experiment that uses a DM.**

A summary of the parameters used in the LIMS simulations is listed in Table 3.2, where, L, represents the overall length in the flow and transverse directions, and, l, represents the individual 2D element length in the flow and transverse directions.

Table 3.2: **The parameters used in LIMS to conduct the flow simulations – permeability values are in m^2 and length values are in cm.**

K_{flow}	K_{trans}	K_{micro}	K_{DM}
1.74E-09	1.06E-11	1.21E-13	9.04E-09

L_{flow}	L_{trans}	l_{flow}	l_{trans}
25.4	0.481	0.31	0.024

For each experiment that is conducted, a LIMS file of the mesh is created that matches the experimental parameters. The viscosity of the resin is input and the constant pressure boundary condition is imposed at a corner node, which represents

the way the flow stems from the top of the preform along the DM and, from there, progresses along the length and through the thickness of the preform [35]. As discussed in 2.4, the cross-sectional area of the 1D tow elements and the volume fraction of the 2D bulk elements are adjusted according to Equations (2.8) and (2.9), respectively. Accordingly, 59% of the resin volume will enter the micro regions of the fiber tows and the remaining 41% of the resin volume will enter the macro regions between the fiber tows. This proportion is realistic, in that the 96 oz/yd^2 E-glass fabric that is experimentally used, which has a volume fraction of 54%, is predominantly composed of fiber tows; the residual space between each of the tows correspondingly makes up much less of the total volume to fill than the tows themselves.

The flow simulations that are conducted represent the four main cases that are manufactured and evaluated, which are listed in Table 3.1. In the LIMS simulation environment, only the base 2D and 1D elements that represent the preform, the fiber tows, and the DM are needed for the NB-NR case, since no bleeding or additional resistance are incorporated. When only bleeding is allowed as for case B-NR, one additional 1D element is attached to the base mesh that has the associated cross-sectional area and permeability of the tubing through which the resin is bled in the experiments. When only resistance is implemented for case NB-R, again only one additional 1D element is attached, which has the cross-sectional area and permeability corresponding to the smaller resistance tubing through which resin flows in the experiments. In case B-R, both 1D elements are combined, so that the resin first flows through the 1D element representing the resistance, and then has the ability to keep bleeding through the final 1D element. For both 1D elements, the permeability is determined from flow through a tube:

$$\frac{Q}{\pi R^2} = \frac{R^2}{8} \frac{\Delta P}{\mu L},$$
(3.2)

where the permeability goes as $R^2/8$ when relating this equation to Darcy's law [2].

3.5 Experimental results

The average void content for each of the five different VARTM-fabricated panels is tabulated in Table 3.3. The results include both samples from each panel, which are machined at three and nine inches along the length of the panel. The standard deviation associated with each average value is included so that the variability can be discussed.

Table 3.3: **Average void percentage findings (on left) and standard deviation values (to the right) for two locations along the length of the manufactured composite panels.**

	NB - NR		B - NR		NB - R		B - R		NB - T
3" into panel	0.80	0.63	1.38	1.36	1.19	0.67	0.66	0.47	5.83
9" into panel	6.02	3.82	1.39	0.82	3.33	1.37	0.69	0.37	6.67

The images are also evaluated from image one, which is taken at the DM side, to image seven, which is taken at the mold-tool side. The succession of images is highlighted in Figure 3.5. When the averages of the void contents of these image locations are sequentially plotted, from image one to image seven, different trends are revealed, depending on if resistance is implemented in the fabrication process.
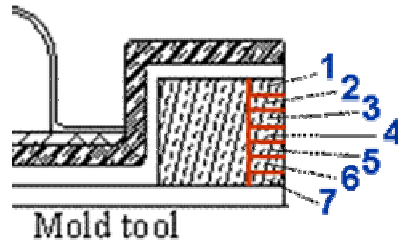
Figure 3.5: **Seven images are taken from the DM side to the mold-tool side of the fabricated composite panel samples.**

The percentage of voids is low near the DM and high near the mold tool when *no* resistance is employed. This trend, in which the void content increases in an overall manner through the thickness of the panel becomes apparent when evaluating the bar graphs in Figures 3.6 and 3.7. In both the NB-NR and B-NR cases, the values are increasing through the thickness for both samples sets taken at three and nine inches along the length of the panel. The NB-NR case nine inches into the panel in Figure 3.6 especially highlights this increasing trend; this sample location is closer to the vent side and no resin is allowed to bleed, so the presence of voids is exacerbated. In the B-NR case, the amounts that are tallied are much lower overall, as compared with when no bleeding is employed. The region of the composite captured by image four in this particular B-NR sample is at the interface of the two plies of fabric. For this reason, a large percentage of the image frames are resin, and no macro voids are found therein, so the overall void content of these images is very low; thus, the increasing void content trend is disrupted at this location.
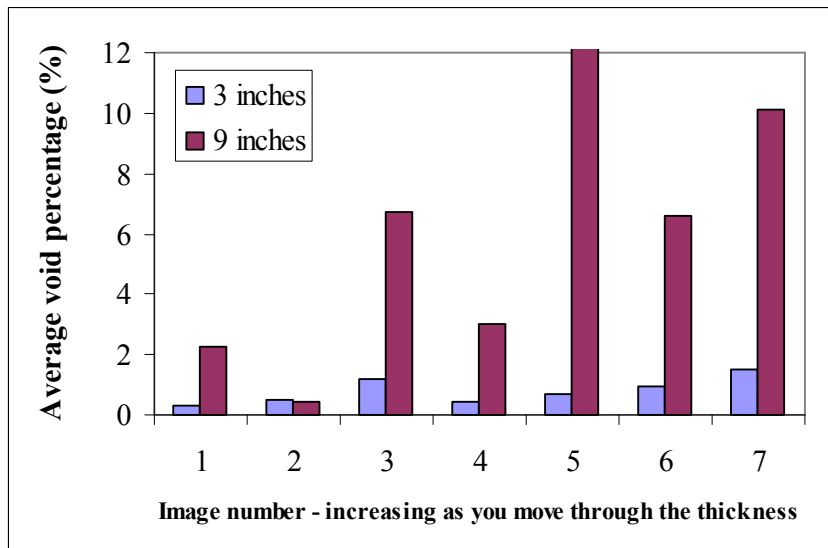
Figure 3.6: The NB-NR case highlights the trend of how the relative void content increases from the DM to the mold-tool side.
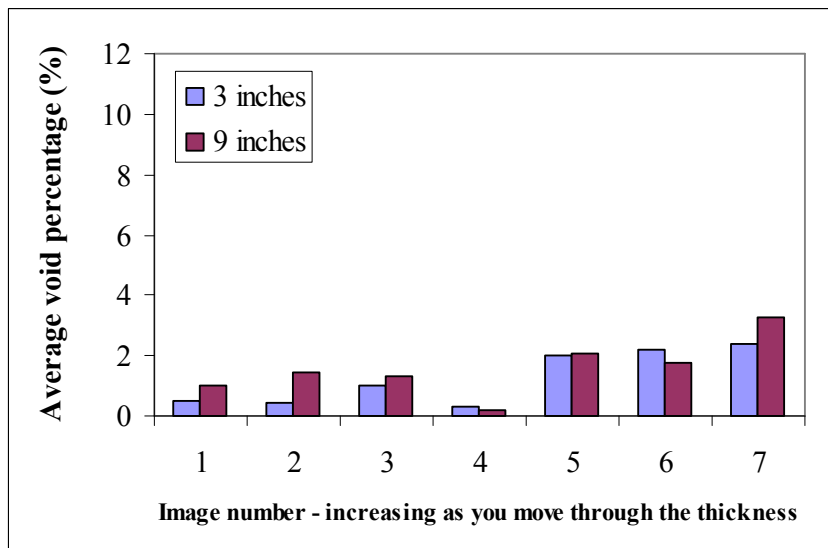
Figure 3.7: The B-NR case also highlights the increasing trend, though the relative amount is substantially lower than when resin is not allowed to bleed.

81

When examining the images from the DM to the tool side of the samples as resistance is added, the bar graphs become more random in distribution, as seen in Figures 3.8 and 3.9, and the overall trend can be considered uniform. The void percentage axes are plotted over the same range as in Figures 3.6 and 3.7, so the distinct differences in the trends and maximum values can be directly compared. The maximum void percentages are lower, when comparing to the respective resistance cases, and these smaller values are evenly distributed, with no distinct trend imposed in a direction through the cross-section.
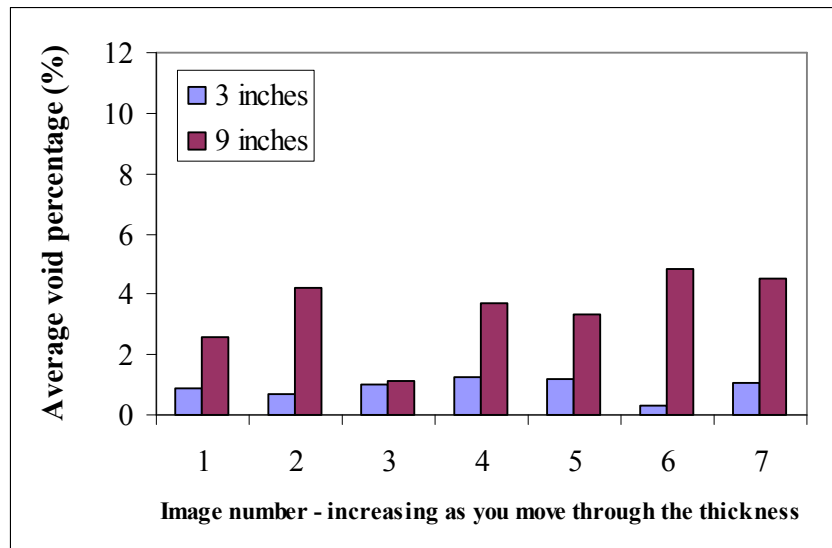
Figure 3.8: **The NB-R case highlights an overall uniform trend from the DM to the mold-tool side, where the relative amount of voids is much lower than when no resistance is employed.**
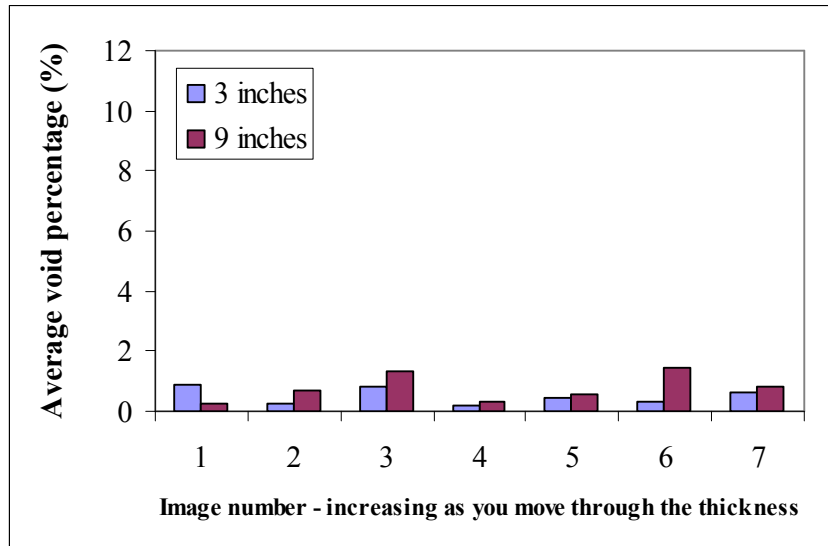
Figure 3.9: **The B-R case also highlights an overall uniform trend, and the overall relative void content is the lowest of the four cases.**

3.6 Parametric study

A contour plot of the flow progression through the mesh, where each contour represents a different interval of time, is first created to show the flow pattern inherent to the VARTM process: the flow along the DM is leading the flow along the mold tool. Figure 3.10 displays this contour plot, in which the dimensions have been scaled in order to visualize the flow pattern. In reality, the height dimension is less than 2% of the overall length dimension, which if imposed, will clearly intensify the discrepancies in the lead length that are even currently observable.
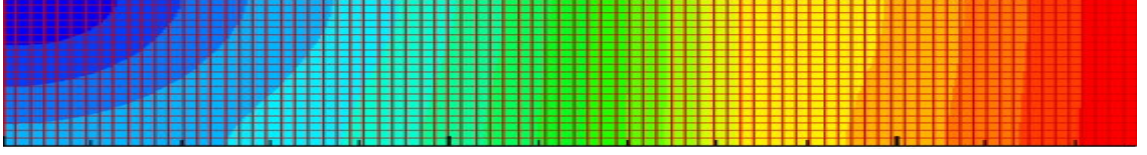
Figure 3.10: A contour plot of the flow progression enables the flow pattern inherent to VARTM to be visualized.

A parametric study is conducted in the LIMS simulation environment for the two extreme processing cases. First, a mesh representing the baseline NB-NR case is addressed; no supplementary elements are needed, since no bleeding is allowed and no additional resistance is added. A non-dimensional time ratio, t^*, is evaluated:

$$t^* = \frac{t_{micro}}{t_{macro}},$$ (3.3)

where t_{micro} is the time it takes the last 1D tow element to fill, and t_{macro} is the time it takes the final 2D element of the bulk preform to fill. This non-dimensional parameter is compared to another non-dimensional parameter K^{**}:

$$K^{**} = \frac{K_{micro}}{K_{macro}},$$ (3.4)

to see what impact changing K_{micro} has on the time it takes all regions of the mesh to fill. Figure 3.11 clearly shows that as K_{micro} is increased an order of magnitude at a time, the time to fully saturate the mesh asymptotically increases.
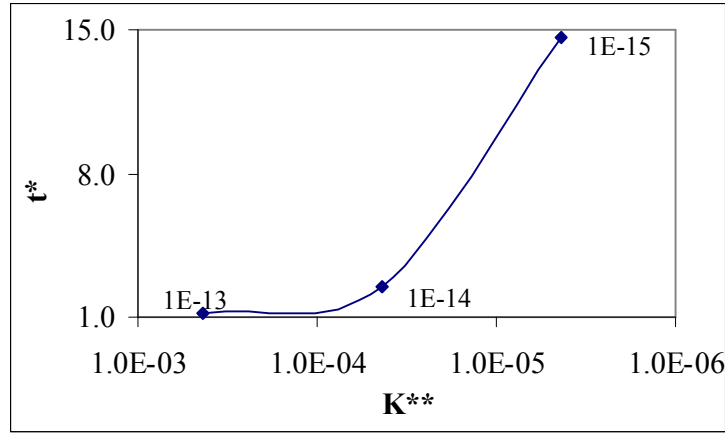
Figure 3.11: **The trend between the non-dimensional parameters t* and K** are evaluated to address the impact K_{micro} has on the overall time to fill all regions of a generated mesh; the order of K_{micro} (in m^2) is labeled next to each data point.**

Next, the complete opposite case, B-R, is addressed. Now both resistance is added to the vent-side of the mesh via an additional 1D element, and the resin is allowed to bleed through that resistance via another 1D element. The bleeder element has a very large volume that will not fill before the final 1D tow element fills. These elements are added to asses the impact the changes in micro permeability and vent resistance have on the overall fill time of the mesh.

A new normalized non-dimensional time parameter, $\hat{t}$, is introduced:

$$\hat{t} = \frac{t*}{t*_{baseline}} , \tag{3.5}$$

85

in order to relate the resulting time ratios, t^*, of the new processing scenario, to the time ratio of the baseline scenario, $t^*_{baseline}$, depending on if K_{micro} is of the order 1e-13 m^2, 1e-14 m^2, or 1e-15 m^2, as previously evaluated. Additionally, a new non-dimensional resistance parameter, $\hat{K}$, is introduced:

$$\hat{K} = \frac{K_{vent}}{K_{macro}}$$

(3.6)

so that the impact K_{vent}, the resistance applied to the vent side of the panel, can be addressed. Figure 3.12 highlights that there is a specific region, which corresponds to a limited range of K_{vent} values that will actually impact the time to saturate the entire mesh. If this range is not attained or it is exceeded, altering the value of K_{vent} will not impact the time. The range represents approximately three orders of magnitude, which, depending on the cross-sectional area of the employed resistance, is a range that can be easily over- or under-shot.
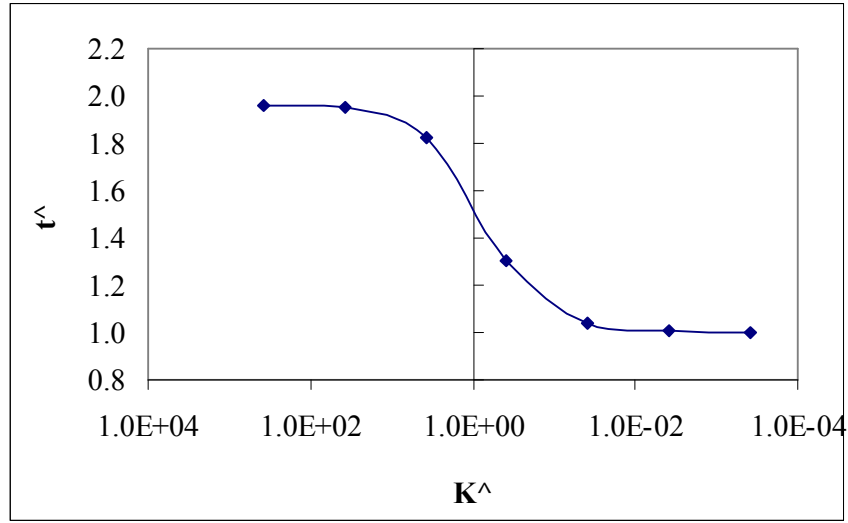
Figure 3.12: **The trend between the non-dimensional parameters t^ and K^ are evaluated to address the impact K_{vent} has on the overall time to fill all regions of a generated mesh.**

This trend can be extended to evaluate curves for which the order of K_{micro} varies; $\hat{t}$ is first introduced to enable this exact analysis to be conducted. Figure 3.13 depicts how the normalized time ratio grows not only as the vent resistance increases, but as the micro permeability increases in increments of one order of magnitude. The three resulting curves can additionally be compared when non-normalized, so that the absolute change is depicted. This plot, which reverts back to t^* along the vertical axis, is shown in Figure 3.14.
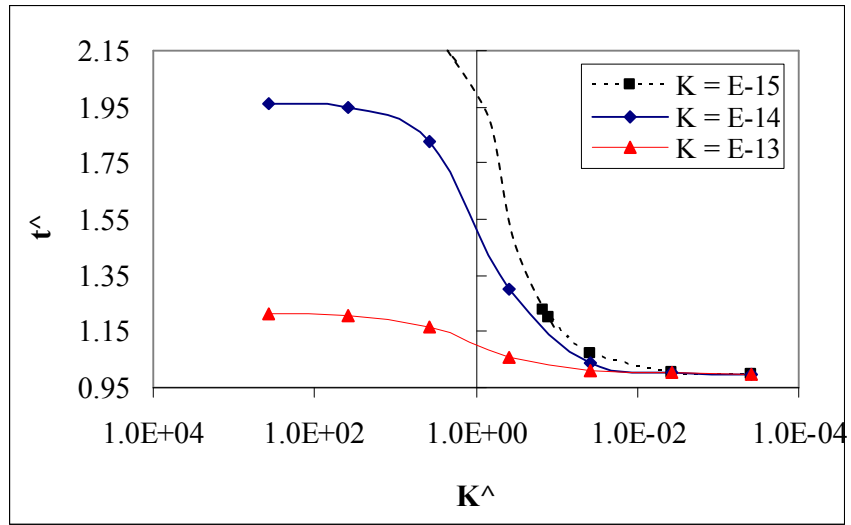
Figure 3.13: The analysis between the non-dimensional parameters t^ and K^ is extended to compare varying values of K_{tow}.
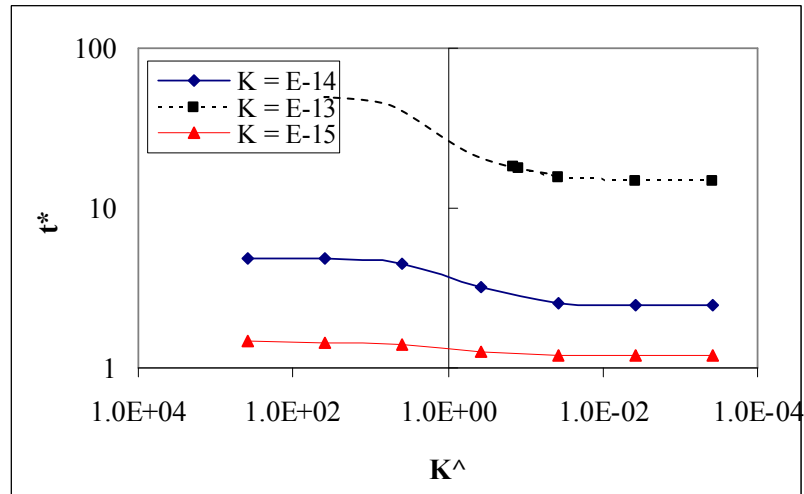
Figure 3.14: The analysis comparing varying values of K_{tow} is changed to evaluate the absolute, instead of the normalized time ratio - t^* not $t^\wedge$.

3.7   Numerical results

A parametric analysis of the fill time ratios is clearly of interest, but so are the changes occurring in the void distribution. LIMS results are obtained from evaluating the four processing scenarios, which can be compared to the experimental results that are achieved. The average void content for each of the simulated panels is tabulated in Table 3.4, along with the standard deviation, so that any variability can be evaluated. The results include two sample sets representative of the machined samples taken at three and nine inches along each panel.

Table 3.4:   Average void percentage findings (on left) and standard deviation values (to the right) for two locations along the length of the simulated composite panels.

	NB - NR		B - NR		NB - R		B - R	
3" into panel	31.78	2.34	0.024	0.016	12.10	2.79	0.016	0.016
9" into panel	55.79	0.13	4.26	3.08	37.70	0.47	0.022	0.010

A succession of seven locations is again evaluated, as if seven images were taken, as is done in the experiments. First, the no-resistance cases are again evaluated.   The LIMS NB-NR case, as shown in Figure 3.15 results in very high void contents at both locations along the length of the panel; at three inches approximately 50% of the fiber tows are filled, while at nine inches only up to 2% of the fiber tows are filled. There is also an overall increasing tendency through the thickness at both locations along the length as uncovered experimentally; the three-inch location is clearly more predominant than the nine-inch location.
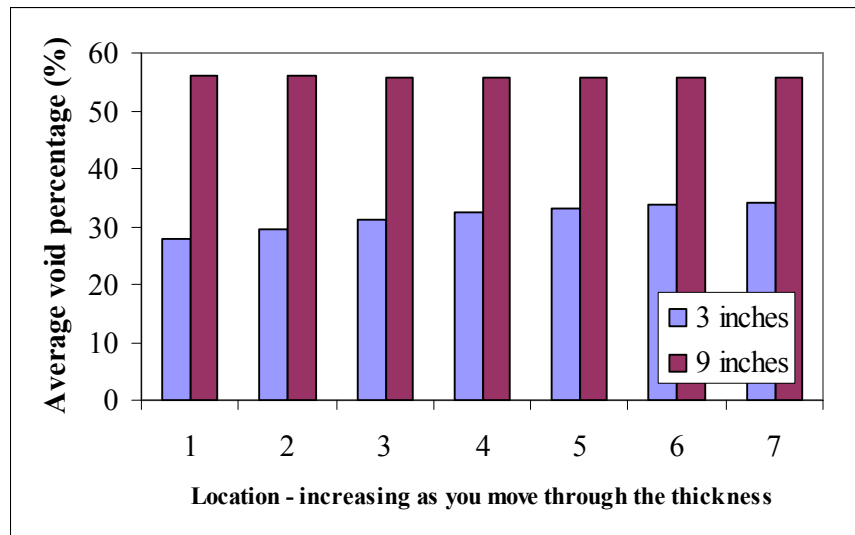
Figure 3.15: In the LIMS NB-NR case, the increasing void content trend is revealed as it is experimentally. The overall void content is very high, as 50% and virtually no tows are filled at the 3 and 9 inch locations, respectively.

The LIMS B-NR case is next assessed and the trend depicted in the experimental data is again apparent in the LIMS results. As evident in the bar graphs in Figure 3.16, the void content increases from the DM to the mold-tool side of the panel at the nine-inch location, while there is no specific trend at the three-inch location. At this location, the content is so low that the overall random trend that is imparted, which does not coincide with the experimental data, is not of much concern.
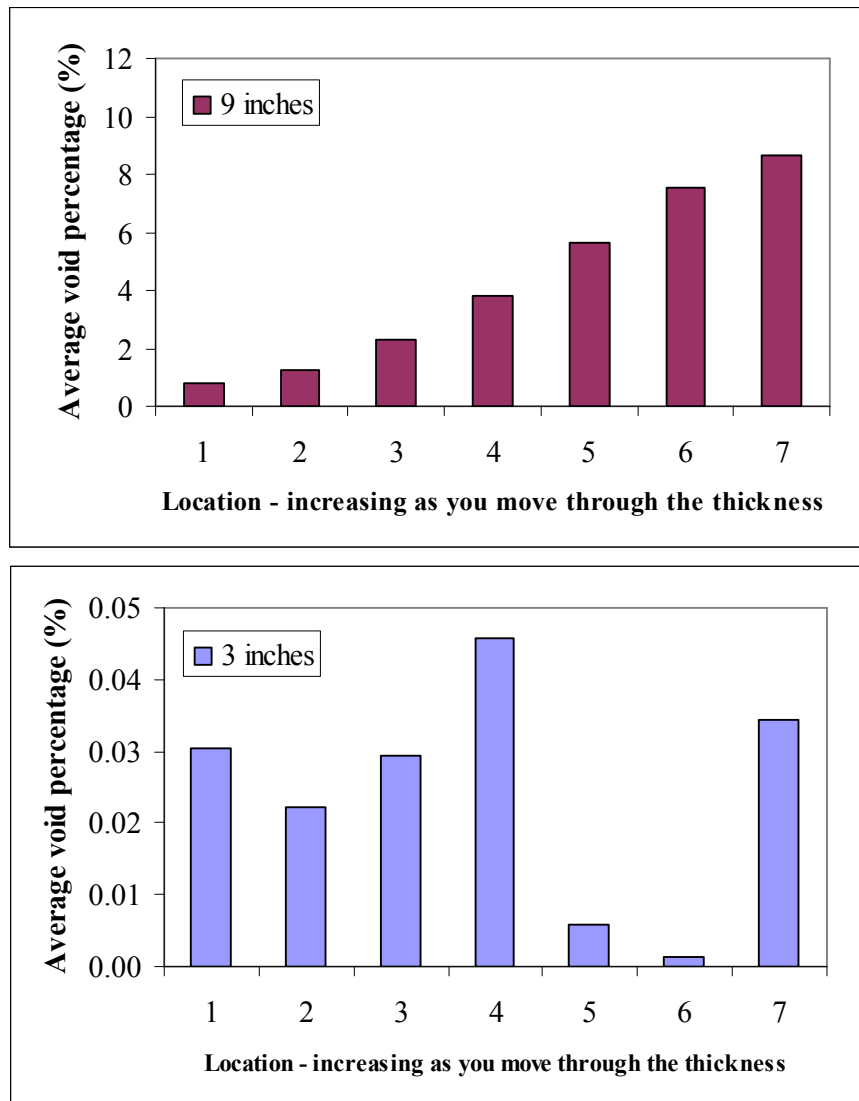
Figure 3.16: In the LIMS B-NR case, the trend of how the relative void content increases from the DM to the mold-tool side is highlighted at the 9 inch location, just as it is experimentally. At the 3 inch location, the void content is so low that the random distribution imparted is not a concern.

Though the void content increases through the thickness, the amount of bleeding that is implemented dramatically improves the percentage of voids

throughout the entire panel.   Figure 3.17 shows how the content decreases considerably from the baseline case in which no bleeding is used (No bleeding – from Figure 3.15).   First, resin is allowed to bleed for the amount of time it takes to fill the panel (1X bleeding); then, resin is allowed to bleed for two times the amount of time it takes to fill the panel (2X bleeding – from Figure 3.16), which corresponds the panel constructed experimentally.
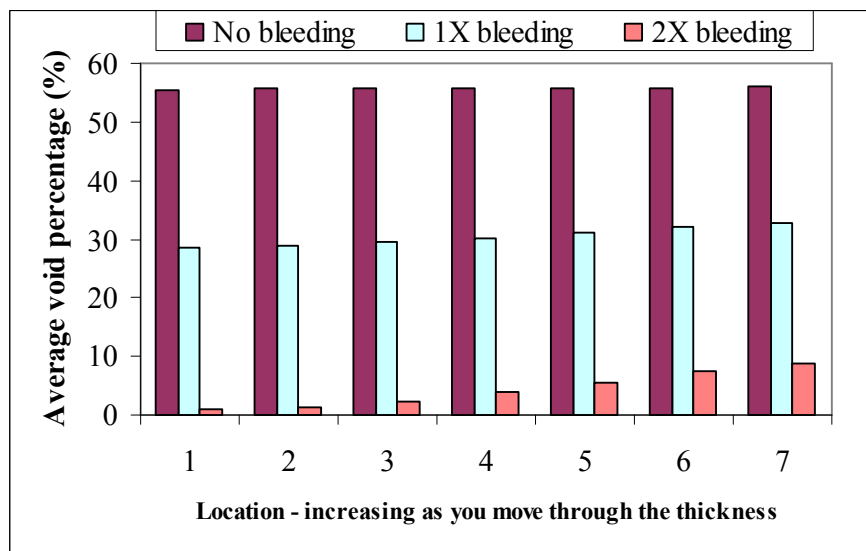
Figure 3.17: In the LIMS B-NR case, the amount of bleeding imposed dramatically improves the void content throughout the panel.

Next, the cases in which resistance is implemented are evaluated. For the LIMS NB-R case in Figure 3.18, a uniform distribution is evident at one panel location, while the three-inch location does give rise to an increasing void content. This is one difference that is exposed in the trends that are captured experimentally. Here, as in the NB-NR case, the overall void content is quite high; at three inches

approximately 80% of the fiber tows are filled, while at nine inches approximately 50% of the fiber tows are filled.
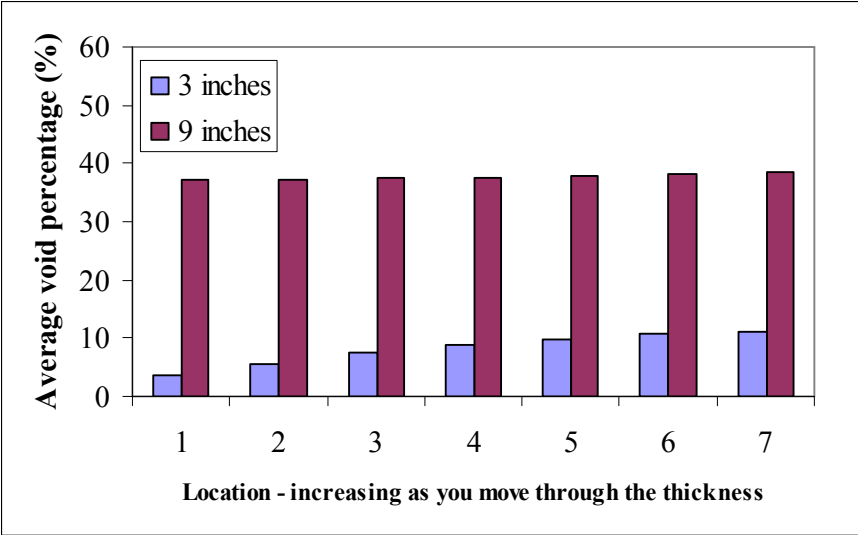
Figure 3.18: In the LIMS NB-R case, the void content levels out at the 9 inch location, as seen experimentally, while the level increases through the thickness at the 3 inch location. The overall void content is again high, as 80% and 50% of tows are filled at the 3 and 9 inch locations, respectively.

For the LIMS B-R case, the random distribution through the thickness is generated in the LIMS environment. This trend is exposed in the assessment of the actual panels as well; consequently, there is no preferred tendency in a specific direction in either LIMS or the experiment. This case has the least amount of voids through the thickness and along the length of the panel, as shown in Figure 3.19, just as experimentally observed.
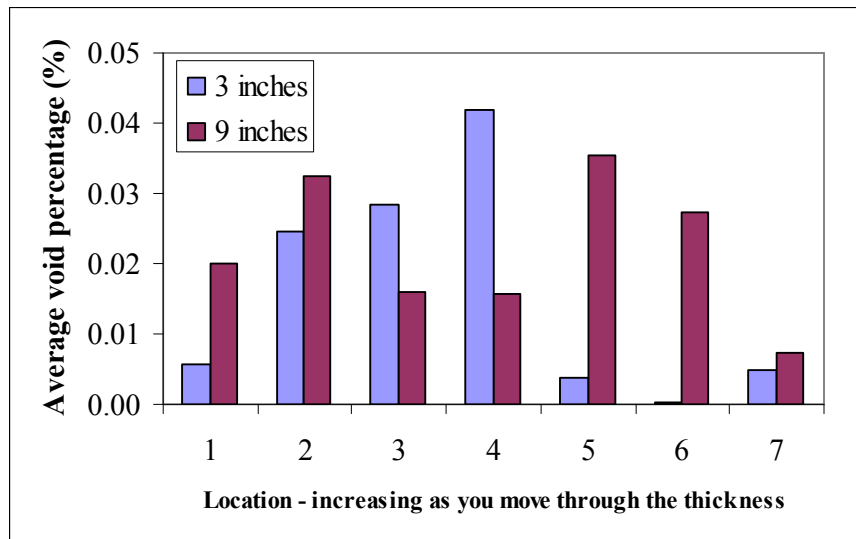
Figure 3.19: In the LIMS B-R case, the void content is randomly distributed, but can be considered uniform overall, and the lowest of all cases, as experimentally shown.

In both Figures 3.18 and 3.19, the maximum void percentages are much smaller, when compared to the respective resistance cases, as found experimentally.

The distribution of voids along the length of the panel can be compared for all four cases, as shown in Figure 3.20. This comparison clearly highlights the implications both bleeding resin and adding resistance have on the overall quality of the final panel.
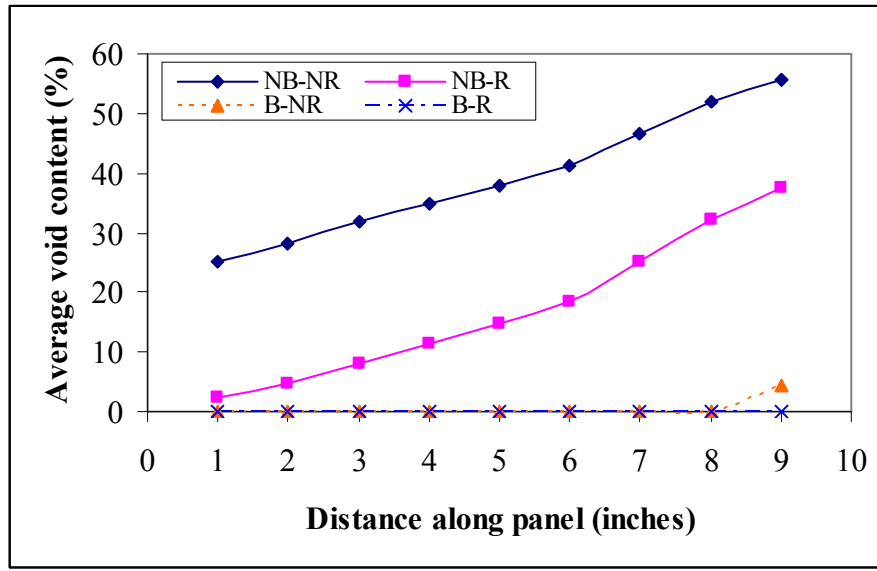
Figure 3.20: The distribution of the void content along the length of the panel can be compared for the four different cases and highlights the implications processing techniques have on part quality.

3.8 Discussion

The average void percentage data found for the five different VARTM-fabricated cases experimentally verifies anticipated trends along the length of the panels. In the baseline case, NB-NR, 7.5 times more voids are found near the vent side of the panel than the inlet side. This is expected, since no time is given for the resin to infiltrate the final region of the panel. Once the resin is allowed to bleed, as in the B-NR case, and thus has enough time to infiltrate the end of the panel, the void content levels out over the entire length of the panel. When resin only flows through the resistance added to the vent side, the ratio of voids from the vent side to the inlet side in the NB-R case decreases to 2.8. When resin is allowed to continue bleeding through the additional resistance, as in the B-R case, the void percentage again levels

out over the length of the panel, and the percentage is half as much as when no resistance is used.

The thick-sectioned composite can not be directly compared to the four other two-layer panels. What can be concluded from the thick-sectioned samples is that sufficient bleeding time and/or the addition of resistance is needed. The processing alterations are needed in order to ensure the resin can infiltrate all regions, since the void content is high at both the inlet and vent side of the panel.

The average void percentage data found for the four LIMS-simulated panels display and verify similar trends along the length of the panels. But, more extreme void content values are exposed in LIMS, as compared to those experimentally revealed. The values cannot be directly compared, since only a relative measure is captured experimentally, while an absolute measure is revealed through LIMS. However, a hypothesis for the high content can be made. The wicking effect that occurs within the fiber tows, which will experimentally fill the micro regions devoid of resin, is not taken into account in LIMS. Since the LIMS model is not predicting this phenomenon, a larger degree of voids remain when evaluating the different processing scenarios. If a pressure condition is prescribed to the 1D elements that represent the tows, the tows could fill at a faster rate. This way, the notion of capillary pressure could be introduced into the model, as other researchers impose in their models [1, 16, 17, 33]. This aspect has not yet been incorporated, so the comparison between the two sets of results is done in terms of the trends that are observed.

In the baseline LIMS case, NB-NR, 1.8 times more voids are found near the vent side of the panel than the inlet side. The difference is again expected, since

no time is given for the resin to infiltrate the final region of the panel, but the ratio is smaller than what is experimentally revealed. Once the resin is allowed to bleed, as in the LIMS B-NR case, the void content does not level out over the length, as revealed experimentally, but the percentage of voids does dramatically decrease, as compared to the baseline case. As resistance is added to the vent side, as in the LIMS NB-R case, the ratio of voids from the vent side to the inlet side at 3.1 is very similar to the experimental ratio. The LIMS results reveal one main difference from the experimental trends. Though the void contents are much lower in LIMS when resistance is added, as is reveled in the experiments, the ratio of vent- to inlet-side voids is actually higher than the baseline case; the experiments expose this ratio is lower than the baseline case. In the LIMS B-R case, in which resin is allowed to bleed through the additional resistance, the void content levels out, as seen experimentally. The percentages are also less than one percent at both locations along the length.

The standard deviation values associated to the average void content values over the length of the panels pinpoint the variability that exists both in the experiment and simulation. The deviations that do exist between the two sets of results are similar for the cases in which bleeding is employed. A definite variability range is established due to the way more voids are found near the mold tool side of the panel than the DM side. Few or no locations may have a void content equal to the average value; the value purely becomes the average of the high content near the mold tool and the low content near the DM, wherein the variability implications of the standard deviation values result. When bleeding is not implemented, the LIMS environment predicts the variability in the void content to be very small. The inter- and intra-tow volumes that must be filled are homogeneous throughout the simulated

preform. This homogeneity may not be the best representation of a real world VARTM process, in that the way the layers stack and mesh together results in regions along the length of the part that must fill varying volumes.

When looking at the trends through the cross-section of the fabricated and simulated panels, the void content increases when *no* resistance is employed. The main difference lies in the baseline LIMS case. Due to the way the volume fractions are re-assigned by the saturation script, 59% of the resin volume enters the tows. A high void content will result if only a small percentage of the tows are filled, as is true for the LIMS NB-NR case; the values could change once capillarity is introduced into the model. The specific values can again not be directly compared, since only a relative measure is made for the experimental cases, and the values from LIMS are absolute. When resistance is incorporated, both the experimental and LIMS cases show the voids level out through the thickness. One location, three inches into the LIMS NB-R panel, does show an increasing trend, from which one can infer just implementing resistance without bleeding is an improvement, but by no means the most consistent method to achieve a uniform void content. Again, there may be a capillary effect playing a role, which is not accounted for in LIMS. Employing both a resistance at the vent and allowing resin to continue to bleed through this resistance results in the lowest void content, which is level overall; this trend is shown experimentally and in the LIMS environment.

The time scale analysis conducted in 2.7 is of interest in this portion of the study as well, since processing parameters are being developed and the time to fill both the macro and micro regions is of interest. The ratio of the micro-permeability parameter to the equivalent macro parameter yields a value of 4.5. This value alludes

to the hypotheses that the pores within the tows will take 4.5 times longer to fill than the pores between the tows. This ratio is clearly of interest in that the bleeding time can be adjusted according to the value of this time scale parameter.

In this study, the micro pores are given 2 times longer to fill than the macro pores. Based on the time scale parameter, the bleeding time would need to be increased to ensure all regions of the panel are fully saturated with resin; that is, if no additional resistance is employed near the vent side of the panel. This conclusion is corroborated in both the experimental and LIMS environment. In the experiments, when allowing only bleeding, the void contents are low, but clearly have the ability to be further reduced. In LIMS, Figure 3.17 especially alludes to how additional bleeding time would achieve a panel with a minimized void content, since up to a 10% void content is still revealed when implementing a time-scale ratio of 2.

3.9   Conclusions

The void distribution results and trends from the four different scenarios are important, since voids may be tolerable in certain applications, as long as the amount remains uniform and thus does not change through the thickness of the part. If this is the case, it would be advantageous to manufacture the part using some form of additional vent-side resistance. The resin should also be allowed to bleed through the resistance, to not only ensure the void content remains uniform, but is minimized. In other applications, the void distribution may not be of interest, as long as a certain face of the part has close to no voids. In this case, the manufacturing process would not necessarily need additional resistance. Bleeding should be allowed, so the void content, though increasing through the cross-section, is much lower than when no resin is allowed to bleed.

The LIMS-generated results do not exactly match the experimental results, but many similar trends are revealed. Processing techniques, which do not incorporate resistance, will result in panels that have more voids closer to the tool-side. Techniques which employ resistance and allow for resin to bleed are ultimately the best way to fabricate a part free of voids. The exact amount of voids cannot be directly compared, since only a relative comparison is conducted experimentally, and the measure in the LIMS environment is absolute; the tendencies that are introduced by the varying processing scenarios are of key importance. The impact of the inclusion of the capillary effect into the LIMS model should also be considered, since the wicking effect would be incorporated and better results could likely be achieved.

The LIMS parametric analysis that is conducted on the two extreme processing scenarios clearly shows the large impact a change in the tow permeability has on the overall fill time. The importance of knowing the appropriate value of K_{tow} is thereby highlighted. The case where both bleeding is allowed and resistance is added to the vent, results in the best way to manipulate the processing technique to achieve the desired results: a part with a minimized void content. The cases where either only bleeding is allowed or only resistance is added are variations of the B-R case. The value of K_{vent} can be made very large so that essentially only bleeding is occurring; or, the length of the bleeding element can be made very small so that essentially only the resistance is a part of the analysis. Depending on the type of fabric, the analysis is definitely warranted before fabrication, since there is only a certain range in which changing K_{vent} can even impact the cycle time of the part and the void distribution throughout the part.

Chapter 4

CONCLUSIONS, CONTRIBUTIONS, AND FUTURE WORK

4.1   Conclusions

Dual-scale porous media is used for all types of LCM processes, whether a matched-mold process like RTM, or a single-sided-mold process like VARTM. This class of fabric has two inherent length scales, and, as a result, two regions in which the flow progresses differently.   In these regions, which are either on the order of millimeter or microns, the key fabric material property varies: the permeability. Previous characterization techniques are able to capture the permeability in one or two fabric directions, but always of just the macro regions of a preform. The permeability values are needed for both the macro and micro regions, so that the flow through such fabrics can be properly modeled and resulting processing traits, like the formation of voids and dry spots, can be predicted.

The predicted void distribution and degree of void formation established from the simulation environment is clearly a valuable result; but, the actual relative void distribution found experimentally is equally, if not more, powerful. The relative changes in the void distribution can be seen both along the length and through the thickness of a manufactured panel and, furthermore, compared as the processing technique is changed. It is imperative to allow the resin to have enough time to not only fill the macro regions between the fiber tows that are on the order of millimeters, but the micro regions between the individual fibers within the tows, which are on the

order of microns. This way, a panel results in which the least possible void content remains.

In summary, the interplay between the micro and macro permeability of dual-scale porous media has been investigated and a characterization methodology has been generated. The effect these two material parameters have on the fill time and void formation has been explored, as well as the role processing techniques play as they are varied.

4.2 Contributions

The employed techniques and corresponding outcomes of the presented work led to contributions in both the areas of permeability characterization and prediction of void distribution due to VARTM process development.

4.2.1 Permeability characterization

- A flow-controlled test system was implemented to monitor the inlet pressure profile of a 1D constant flow rate RTM experiment. This system utilized a flow-controlled injector and incorporated an updated, more robust mold that was both designed and manufactured in order to withstand anticipated ranges of pressure.

- A data analysis template was designed to easily evaluate the experimental pressure data over the duration of the experiment and determine the macro permeability of the preform.

- An additional template was developed to interpolate the LIMS pressure data and conduct a linear least squares regression, to determine which micro-permeability parameter minimized the error between the LIMS and experimental data sets.

- An overall methodology was developed to characterize the permeability of dual-scale porous media. First, the macro permeability is determined from the constant flow rate RTM experimental data, then, a LIMS analysis is conducted in order to match pressure profiles and determine the micro-permeability fitting parameter.

4.2.2 Void distribution based on VARTM processing

- The anticipated void distribution trends were experimentally verified by actual VARTM fabrication and image analysis.
- A methodology was developed for processing fabrics to include the lowest void content, when manufacturing composites panels using VARTM:
  - Resistance should be added and bleeding should be employed to ensure any remaining void distribution is uniform through the *thickness* of the part.
  - Bleeding should be incorporated to ensure any remaining void content is distributed uniformly over the *length* of the part.

4.3 Future work

Based on some of the limitations of the current system, adjustments can be made to the procedure and implementation to further improve the techniques being employed. The partially-saturated length, Ls, was found to be a very useful parameter when looking at the different non-dimensional trends in the permeability investigation portion of the study. The value is currently only attainable from LIMS; a method to experimentally measure this quantity would serve as a very important component of future permeability characterizations. Comparisons between the simulation and experimental results could be made and evaluated, and further conclusions could be drawn.

Also currently, the underlying assumption made in the LIMS tow saturation script is that the constant partially-saturated length region must necessarily stem from the origin. This should be reevaluated, since pressure curves should be able to result, which do not necessarily have a constant partially-saturated-length region that stems from the origin. This aspect has been analytically evaluated in [31] and the need to remove this condition can thereby be proven. The LIMS results implementing the different assumptions should be compared, in order to evaluate the differences between the models. The two models should next be compared to both the experimental and analytical results, in order to obtain a better understanding of the aspects of the flow phenomenon in place.

Other fabrics should be evaluated to assess not only the permeability values, but to see how the void distribution compares to the void content and trends experienced by the current fabric. The LIMS model can additionally be assessed to incorporate the effect of capillarity or wicking, to see if the experimental results can match the simulation more closely. Micro sensors can also be placed within tows near determined void formation sites to track how the progression of the saturation. These sensors can be used to corroborate simulation results, or as a manufacturing tool to ensure micro impregnation regions are fully saturated.

A form of fabric database could be developed to best asses the processing technique to be implemented and which fabric to choose. The decision would be based on how the combination of macro- and micro-permeability values impact the void content. Thereby, this mechanism of quality control could be incorporated before the manufacturing process, instead of others which are implemented after, when poor quality parts must be sacrificed.

REFERENCES

1. Hamidi, Y.K., L. Aktas, and M.C. Altan, Three-dimensional features of void morphology in resin transfer molded composites. Composites Science and Technology, 2005. 65(7-8): p. 1306.

2. Advani, S.G. and E.M. Sozer, Process Modeling in Composites Manufacturing. 2003, New York: Marcel Dekker.

3. Luce, T.L., An experimental investigation of the in-situ in-plane and transverse permeabilities of fiber preforms, in Mechanical Engineering. 1995, University of Delaware: Newark.

4. Gokce, A., M. Chohra, S.G. Advani, and S.M. Walsh, Permeability estimation algorithm to simultaneously characterize the distribution media and the fabric preform in vacuum assisted resin transfer molding process. Composites Science and Technology. In Press, Corrected Proof.

5. Binetruy, C., B. Hilaire, and J. Pabiot, The interactions between flows occurring inside and outside fabric tows during rtm. Composites Science and Technology, 1997. 57(5): p. 587.

6. Slade, J., K.M. Pillai, and S.G. Advani, Investigation of Unsaturated Flow in Woven, Braided and Stitched Fiber Mats During Mold-Filling in Resin Transfer Molding. Polymer Composites, 2001. 22(4): p. 491-505.

7. Parnas, R.S., J.G. Howard, T.L. Luce, and S.G. Advani, Permeability Characterization Part 1: A Proposed Standard Reference Fabric for Permeability. Polymer Composites, 1995. 16(6): p. 429-445.

8. Luce, T.L., S.G. Advani, J.G. Howard, and R.S. Parnas, Permeability Characterization Part 2: Flow Behavior in Multiple-Layer Preforms. Polymer Composites, 1995. 16(6): p. 446-458.

9. Babu, B.Z. and K.M. Pillai, Experimental Investigation of the Effect of Fiber-Mat Architecture on the Unsaturated Flow in Liquid Composite Molding. Journal of Composite Materials, 2004. 38(1): p. 57-79.

10. Lawrence, J.M., J. Barr, R. Karmakar, and S.G. Advani, Characterization of preform permeability in the presence of race tracking. Composites Part A: Applied Science and Manufacturing, 2004. 35(12): p. 1393.

11. Luo, Y., I. Verpoest, K. Hoes, M. Vanheule, H. Sol, and A. Cardon, Permeability measurement of textile reinforcements with several test fluids. Composites Part A: Applied Science and Manufacturing, 2001. 32(10): p. 1497.

12. Han, K.K., C.W. Lee, and B.P. Rice, Measurements of the permeability of fiber preforms and applications. Composites Science and Technology, 2000. 60(12-13): p. 2435.

13. Hoes, K., D. Dinescu, H. Sol, M. Vanheule, R.S. Parnas, Y. Luo, and I. Verpoest, New set-up for measurement of permeability properties of fibrous reinforcements for RTM. Composites Part A: Applied Science and Manufacturing, 2002. 33(7): p. 959.

14. Ding, L., C. Shih, Z. Liang, C. Zhang, and B. Wang, In situ measurement and monitoring of whole-field permeability profile of fiber preform for liquid composite molding processes. Composites Part A: Applied Science and Manufacturing, 2003. 34(8): p. 779.

15. Endruweit, A. and P. Ermanni, The in-plane permeability of sheared textiles. Experimental observations and a predictive conversion model. Composites Part A: Applied Science and Manufacturing, 2004. 35(4): p. 439.

16. Kang, M.K., W.I. Lee, and H.T. Hahn, Formation of micro voids during resin-transfer molding process. Composites Science and Technology, 2000. 60(12-13): p. 2427.

17. Lee, D.H., W.I. Lee, and M.K. Kang, Analysis and minimization of void formation during resin transfer molding process. Composites Science and Technology. In Press, Corrected Proof.

18. Simacek, P. and S.G. Advani, A numerical model to predict fiber tow saturation during liquid composite molding. Composites Science and Technology, 2003. 63(12): p. 1725.

19. Parnas, R.S. and F.R. Phelan, The Effect of Heterogeneous Porous Media on Mold Filling in Resin Transfer Molding. Sampe Quarterly, 1991. 22: p. 53-60.

20. Sadiq, T.A.K., S.G. Advani, and R.S. Parnas, Experimental investigation of transverse flow through aligned cylinders. International Journal of Multiphase Flow, 1995. 21(5): p. 755.

21. Breard, J., A. Saouab, and G. Bouquet, Numerical simulation of void formation in LCM. Composites Part A: Applied Science and Manufacturing, 2003. 34(6): p. 517.

22. Lekakou, C. and M.G. Bader, Mathematical modeling of macro- and micro-infiltration in resin transfer molding (RTM). Composites Part A: Applied Science and Manufacturing, 1998. 29(1-2): p. 29.

23. Binetruy, C. and B. Hilaire, Tow Impregnation Model and Void Formation Mechanisms during RTM. Journal of Composite Materials, 1998. 32(3): p. 223-245.

24. Pillai, K.M. and S.G. Advani, A Model for Unsaturated Flow in Woven Fiber Preforms during Mold Filling in Resin Transfer Molding. Journal of Composite Materials, 1998. 32(19): p. 1753-1783.

25. Ngo, N.D. and K.K. Tamma, Micro-scale permeability predictions of porous fibrous media. International Journal of Heat and Mass Transfer, 2001. 44(16): p. 3135.

26. Pillai, K.M., Governing equations for unsaturated flow through woven fiber mats. Part 1. Isothermal flows. Composites Part A: Applied Science and Manufacturing, 2002. 33(7): p. 1007.

27. Takano, N., M. Zako, T. Okazaki, and K. Terada, Microstructure-based evaluation of the influence of woven architecture on permeability by asymptotic homogenization theory. Composites Science and Technology, 2002. 62(10-11): p. 1347.

28. Grujicic, M., K.M. Chittajallu, and S. Walsh, Effect of shear, compaction and nesting on permeability of the orthogonal plain-weave fabric preforms. Materials Chemistry and Physics, 2004. 86(2-3): p. 358.

29. Mogavero, J., Compression characterization and resin infiltration of multi-layered preforms in resin transfer molding, in Mechanical Engineering. 1996, University of Delaware: Newark.

30. Estrada, G., Experimental permeability characterization of fiber preforms, in Mechanical Engineering. 2002, University of Delaware: Newark.

31. Zhou, F., N. Kuentzer, P. Simacek, S.G. Advani, and S. Walsh, Analytic characterization of the permeability of dual-scale fibrous porous media. Composites Science and Technology, 2005. In Press.

32. Simacek, P. and S.G. Advani, Desirable Features in Mold Filling Simulations for Liquid Molding Processes. Polymer Composites, 2004. 25: p. 355-367.

33. Pearce, N., F. Guild, and J. Summerscales, A study of the effects of convergent flow fronts on the properties of fiber reinforced composites produced by RTM. Composites Part A, 1998. 29: p. 141-152.

34. Jinlian, H., L. Yi, and S. Xueming, Study on void formation in multi-layer woven fabrics. Composites Part A: Applied Science and Manufacturing, 2004. 35(5): p. 595.

35. Modi, D., Numerical issues in mold filling simulations for composites processing, in Mechanical Engineering. 2003, University of Delaware: Newark.

36. Avila, A.F. and D.T.S. Morais, A multi-scale investigation based on variance analysis for hand lay-up composite manufacturing. Composites Science and Technology, 2005. 65(6): p. 827.

37. Kuentzer, N., P. Simacek, S.G. Advani, and S. Walsh, Permeability characterization of dual scale fibrous porous media. Composites Part A: Applied Science and Manufacturing. In Press.

38. Liu, L., B.-M. Zhang, D.-F. Wang, and Z.-J. Wu, Effects of cure cycles on void content and mechanical properties of composite laminates. Composite Structures. In Press, Corrected Proof.

39. Huang, H. and R. Talreja, Effects of void geometry on elastic properties of unidirectional fiber reinforced composites. Composites Science and Technology. In Press, Corrected Proof.

40. Abraham, D. and R. McIlhagger, Investigations into various methods of liquid injection to achieve moldings with minimum void contents and full wet out. Composites Part A: Applied Science and Manufacturing, 1998. 29(5-6): p. 533.

41. Hagstrand, P.O., F. Bonjour, and J.A.E. Manson, The influence of void content on the structural flexural performance of unidirectional glass fiber reinforced polypropylene composites. Composites Part A: Applied Science and Manufacturing, 2005. 36(5): p. 705.

42. Afendi, M., W.M. Banks, and D. Kirkwood, Bubble free resin for infusion process. Composites Part A: Applied Science and Manufacturing, 2005. 36(6): p. 739.

Appendix A

SIMULATION STEPS AND ASSOCIATED CODE

The simulation is conducted in three main steps:

1. Bar elements are generated to simulate the intra-tow spaces in dual-scale fabrics by running SATURATION.EXE on the existing 2D mesh that represents the preform in the experimental RTM set-up.

   - The program SATURATION.EXE reads an existing dmp-file, adds to each node a 1D element and an additional node, and writes a dmp-file at the end that then contains both the initial 2D and new 1D elements.

   - SATURATION.EXE is a command line program that follows the syntax: saturation file.dmp -DX=V, -DY=V, -DZ=V, -A=V, -Vf=V, -K=V where V represents a floating point value.

   - Either the x-, y-, or z-component of the 1D element, depending which direction the element should lay, is constructed using either the -DX, -DY, or -DZ components, respectively.

   - The cross-section, -A, for which the default value is 1E-3 m^2, the fiber volume fraction, -Vf, and the permeability, -K, for which the default value is 1E-10 m^2, are then set, all of which only pertain to the new 1D elements.

   - The length dimension of the bar element (-DX, -DY, or -DZ) must be set properly, but all other components can be re-set when executing Step 2.

2. The new converted mesh is read into LIMS and the LIMS basic file, SATURACE.LB is loaded.

   - It is executed by the simple syntax: SetElems Len,K,Vf,A where Len is the previously set x-, y-, or z-component of the bar elements, K is again the permeability, Vf is again the fiber volume fraction of the fiber tows, and A is again the cross-section, the latter three which can be different from the values assigned in Step 1.

The script is called as SetElems Len,K,Vf,A

This script sets the cross sections of the 1D elements and adjusts the volume fraction of the 2D elements for the saturation simulation. It assumes that element Len, K, and Vf are set properly, and that the fiber tow properties are uniform.

```
        PROC SetElems
        DEFDBL OrLen,OrK,OrVf,OrA
```

The arguments are checked – to ensure there are not less than or more than four input – and then set.

```
        IF Argc() <> 4 THEN
            MESSAGE "Call as SetElems Len,K,Vf,A"
            STOP
        ENDIF
        LET OrLen = Argument(1)
        LET OrK = Argument(2)
        LET OrVf = Argument(3)
        LET OrA = Argument(4)
```

The true number of nodes and elements are assigned.

```
        DEFINT TrueNN,TrueNE
        LET TrueNN = SoNumberNodes()/2
        LET TrueNE = SoNumberElems() - TrueNN
```

The proper elements can now be processed. The contributions from the true elements are added to the 1D elements.

```
        DEFINT i,j,nn,nelem
        DEFDBL Tmp,Vf,Area
```

The cross-sections of the 1D elements are altered.
Equation (2.8) is implemented into the code.

```
FOR i=1 TO TrueNE

    CALL ElemVolume i
    LET Area = 2.0*(Volume*GETELEMDATA(i,3))/(OrVf*OrLen)
    LET nn = GETELEMDATA(i,100)
        FOR j=1 TO nn
            LET nelem=GETELEMDATA(i,100+j)+TrueNE
            SETELEMDATA(nelem,2,
                GETELEMDATA(nelem,2)+Area/nn)
            SETELEMDATA(nelem,3,OrVf)
            SETELEMDATA(nelem,10,OrK)
        NEXT j
```

The volume fractions of the 2D elements are then altered.
Equation (2.9) is implemented into the code.

```
    LET Tmp=GETELEMDATA(i,3)*(1.0+2.0*(1.0-OrVf)/OrVf)
    IF Tmp>=1.0 THEN
        MESSAGE "New fiber volume fraction exceeds 100%"
        STOP
    ENDIF
    SETELEMDATA(i,3,Tmp)

NEXT i
```

The original and now extra cross-sections are subtracted from the 2D elements.

```
FOR i = (TrueNE + 1) TO SoNumberElems()
    LET Tmp = GETELEMDATA(i,2) - OrA
    SETELEMDATA(i,2,Tmp)
NEXT i
```

A cleanup is done of the variables.

```
ERASE Volume
ERASE i,j,nn,nelem,Tmp,Vf,Area
ERASE TrueNN,TRUENE
ERASE OrLen,OrK,OrVf,OrA

ENDPROC
```

3. The simulation is executed and the results are saved as needed.

```
proc fill
defint IsFull,i,NoNodes
let NoNodes=SoNumberNodes()/2

setintype "dmp"
read "WCa.dmp"
```

The constant flow rate boundary condition is set.

```
settime 0.0
setgate 1,2,0.000000023224
setgate 2,2,0.000000046448
setgate 3,2,0.000000046448
          .
          .
setgate 59,2,0.000000046448
setgate 60,2,0.000000046448
setgate 61,2,0.000000023224
```

The pressure data from the central inlet node is collected in a text file.

```
opentracer " WCa.txt",1,1,31
```

All nodes are filled, until the macro flow reaches the end of the preform.

```
do
  let IsFull = 1
  solve
  for i = 1 to NoNodes
   if SoFillFactor(i)<0.99 then
     let IsFull = 0
   endif
  next i
  print sonumberempty()," left"
loop while IsFull = 0
closetracer " WCa.txt"
```

114

The results, which can be accessed by LIMS, are saved.

```
setouttype "dmp"
write " WCa_RES.dmp"
```

*The results, which can be accessed by TECPLOT, are saved.*

```
setouttype "tplt"
write " WCa_RES.tec"

erase isFull,i,NoNodes
endproc
```

Appendix B

**CONTOUR PLOTS USED TO DETERMINE THE PARTIALLY-SATURATED LENGTH**

Each mesh used by LIMS corresponds to the actual preform used in the experiment. The flow parameters of each simulation also correspond to the actual flow conditions implemented during the experiment. A resulting parameter that can be output by LIMS, which is not experimentally measured, is the partially-saturated length, Ls. This value is the length of the preform that is more than 1%, but less than 99% saturated with fluid, and it corresponds to the shaded regions in all of the following contour plots. The results of both experiments from all four fabrics are shown in Figures B.1 through B.8.
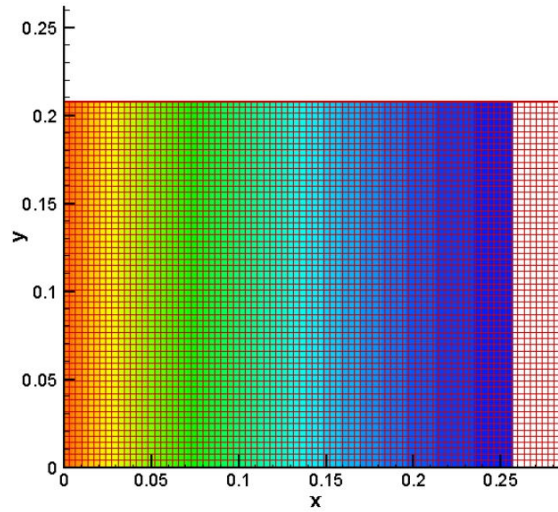
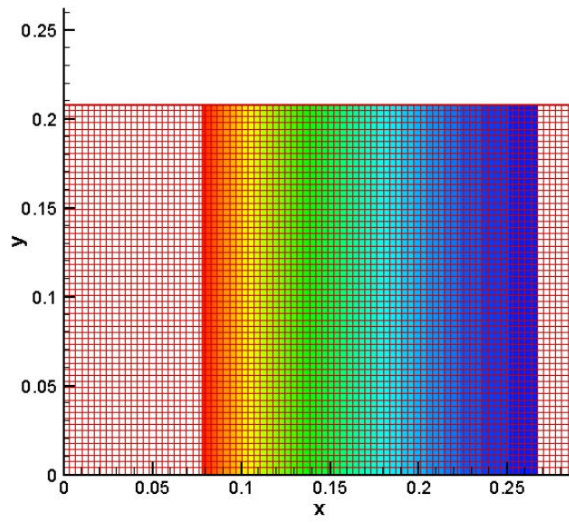**Figure B.1: Contour plot of Ls for 9 oz/yd^2 woven carbon experiment a. Ls/L = 0.892.**
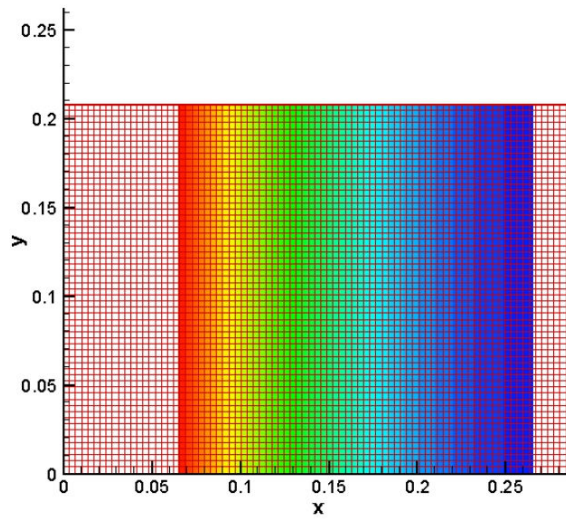
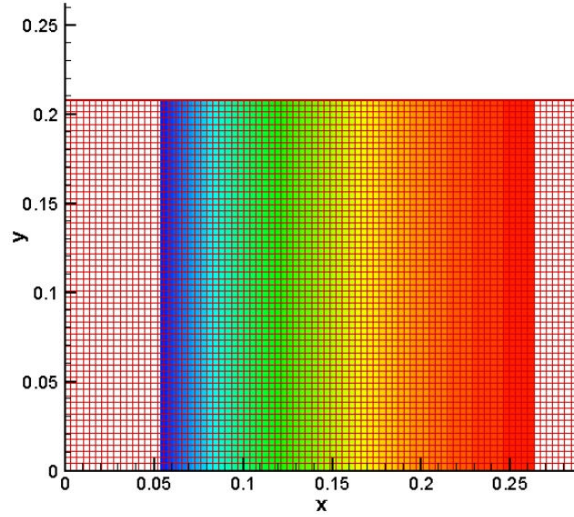**Figure B.2:** **Contour plot of Ls for 9 oz/yd^2 woven carbon experiment b. Ls/L = 0.653.**
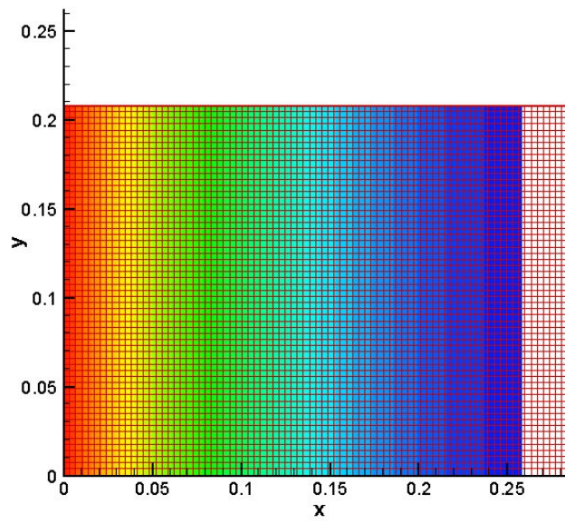
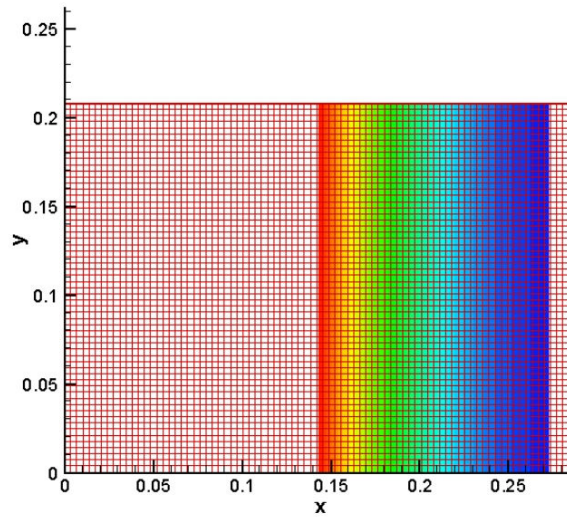**Figure B.3:** **Contour plot of Ls for 24 oz/yd^2 woven E-glass experiment a. Ls/L = 0.944.**
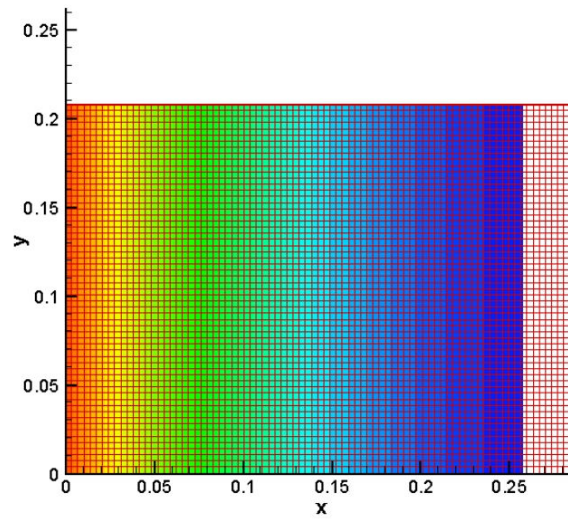
Figure B.4: Contour plot of Ls for 24 oz/yd² woven E-glass experiment b. Ls/L = 0.691.

Figure B.5: Contour plot of Ls for 96 oz/yd² stitched E-glass experiment a. Ls/L = 0.729.

119

Figure B.6: Contour plot of Ls for 96 oz/yd^2 stitched E-glass experiment b. Ls/L = 0.448.

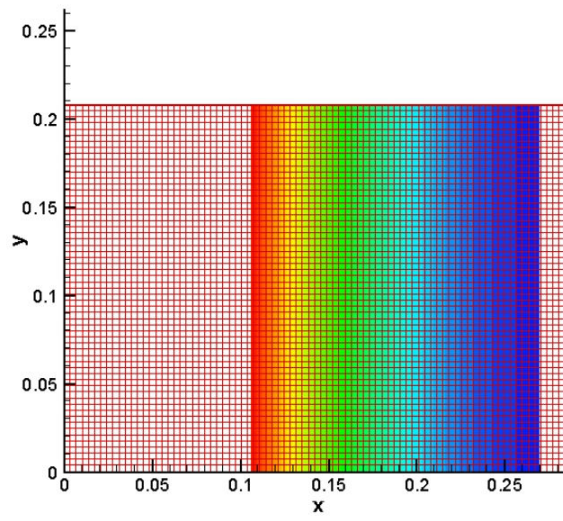**Figure B.7: Contour plot of Ls for 18 oz/yd^2 stitched E-glass experiment a. Ls/L = 0.927.**

Figure B.8: Contour plot of Ls for 18 oz/yd^2 stitched E-glass experiment b. Ls/L = 0.566.

Appendix C

ANALYTICAL MODEL*

*Developed by Fuping Zhou. The complete details are available in [31].

The tow saturation rate is the key component to be evaluated, since it is the mechanism that is drawing fluid from the macro flow region into the fiber tows during the partially-saturated zone. The simplest model would assume this rate to be constant. But, in order to accurately quantify the impregnation, the rate must be dependent on the pressure, which is inherently a function of time:

$$\frac{ds}{dt} = C \cdot p \, , \tag{C.1}$$

where ds/dt is the saturation rate, C is a constant, and p is the pressure. If the partially-saturated zone is set from 1% to 99%, then:

$$C = \frac{a \cdot K_{tow}}{t_{tow}^2 \cdot (1 - V_f^{tow}) \cdot \mu} \, , \tag{C.2}$$

where t_{tow} is the thickness of the fiber tow and where a is the inverse of average saturation, which is determined by the solution derived in Appendix A of [31].

Compacted tows will not necessarily retain the oblong shape with which they begin. Thus, the shape of the tow into which the fluid is moving is assumed to be rectangular for this model, just as is assumed in LIMS; this garners simplifications, since no radial geometries need to be incorporated into the analysis. This is also not far from reality, as most fiber tows under compaction do flatten out to very high aspect ratio ellipses.

Regions (i), (ii), and (iii) of Figure 2.7 can be analyzed analytically, where the pressure distribution due to the non-linear partially-saturated zone (ii) is particularly of interest. The minimum experimental requirement that the constant partially-saturated length zone (iii) is achieved is assumed to be met. In region (ii), the applicable set of governing equations is:

$$\frac{d\langle v_d \rangle}{dx} = -V_f^{tows\ in\ EV} \cdot (1 - V_f^{tow}) \cdot \frac{ds}{dt}$$

$$\langle v_d \rangle = -\frac{K}{\mu}\frac{dp}{dx}$$

(C.3)

which reduce to:

$$\frac{d\langle v_d \rangle}{dx} = 0$$

$$\langle v_d \rangle = -\frac{K}{\mu}\frac{dp}{dx}$$

(C.4)

in region (iii).

A non-dimensional analysis is first conducted, which yields the set of dimensionless variables that are used throughout the solution procedure:

$$\langle \hat{v}_d \rangle = \frac{\langle v_d \rangle}{\overline{\langle v_d \rangle}} \qquad where\ \overline{\langle v_d \rangle} = \frac{Q}{A}$$

$$\hat{t} = \frac{t}{\overline{t}} \qquad where\ \overline{t} = \frac{LA}{Q}$$

$$\hat{x} = \frac{x}{\overline{x}} \qquad where\ \overline{x} = L$$

$$\hat{p} = \frac{p}{\overline{p}} \qquad where\ \overline{p} = \frac{Q\mu L}{AK}$$

(C.5)

When the parameters are applied to the governing equations in the partially-saturated zone (C.3), the following set of equations results:

$$\langle \hat{v}_d \rangle = -\frac{d\hat{p}}{d\hat{x}}$$

$$\frac{d^2\hat{p}}{d\hat{x}^2} - k_1^2 \hat{p} = 0 \qquad where\ k_1^2 = \frac{V_f^{tows\ in\ EV} \cdot (1 - V_f^{tow}) \cdot C \cdot \mu \cdot L^2}{K_{bulk}}$$

$$\frac{d\hat{s}}{d\hat{t}} = k_2 \hat{p} \qquad where\ k_2 = \frac{k_1^2}{V_f^{tows\ in\ EV} \cdot (1 - V_f^{tow})}$$

(C.6)

When the parameters are applied to the remaining governing equations in the constant partially-saturated length zone (C.4), the resulting set of equations is dramatically simplified:

$$\langle \hat{v}_d \rangle = -\frac{d\hat{p}}{d\hat{x}}$$
$$\frac{d\langle \hat{v}_d \rangle}{d\hat{x}} = 0 \qquad\qquad\qquad\qquad \text{(C.7)}$$

The general pressure distribution which results in region (ii) is:

$$\hat{p} = A\cosh(k_1\hat{x}) + B\sinh(k_1\hat{x}), \qquad\qquad \text{(C.8)}$$

where A and B are constants that must be determined by the boundary conditions. The resulting inlet pressure profile when applying the conditions $\dfrac{d\hat{p}}{d\hat{x}} = -1 \; at \; \hat{x} = 0$ and $\hat{p} = 0 \; at \; \hat{x} = \hat{L}_1$, where $\hat{L}_1$ is the developing partially-saturated length, is:

$$\hat{p} = \frac{1}{k_1}(\tanh(k_1\hat{L}_1)\cosh(k_1\hat{x}) - \sinh(k_1\hat{x})), \qquad\qquad \text{(C.9)}$$

where the applied boundary conditions are depicted in Figure C.1.
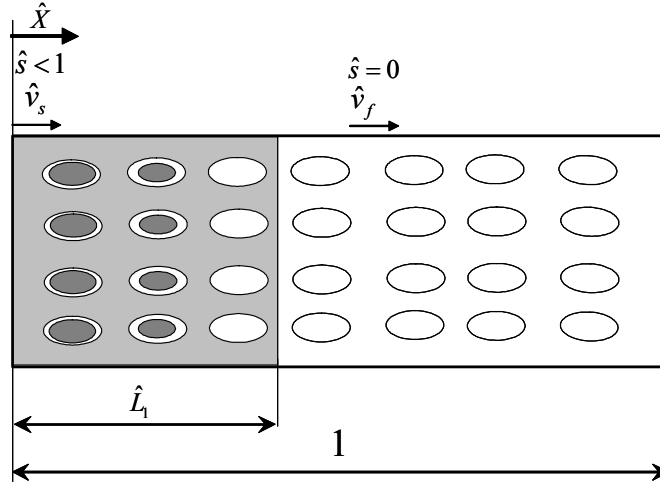
Figure C.1: $\hat{L}_1$ represents the partially-saturated zone from the injection location. When $\hat{t} = \hat{t}_s$, $\hat{L}_1 = \hat{L}_{us}$ and the $\hat{s}$ at injection location will be 1. The mold length is non-dimensionalized to unity (1).

The inlet pressure and the saturation rate can then be expressed in terms of the parameters k_1 and k_2 as follows:

$$\hat{p}_{inlet} = \frac{\tanh(k_1 \hat{L}_1)}{k_1} = \frac{\hat{t}}{\phi_t \sqrt{1 + (k_1 \hat{t} / \phi_t)^2}} \, , \qquad (C.10)$$

$$\frac{\partial \hat{s}}{\partial \hat{t}} = k_2 \hat{p}_{inlet} = \frac{k_2 \hat{t}}{\phi_t \sqrt{1 + (k_1 \hat{t} / \phi_t)^2}} \, . \qquad (C.11)$$

Integrating Equation (C.11), the time needed for the preform at the inlet to become fully-saturated, $\hat{t}_s$, which occurs when $\hat{s} = 1$, is determined:

$$\hat{t}_s = \frac{\sqrt{k_1^2 + 2\phi_t k_2}}{k_2} \, . \qquad (C.12)$$

The corresponding time needed for the flow front to reach the end of the mold is:

$$\hat{t}_1 = \phi_f (1 - \hat{L}_{us}) + \hat{t}_s \, , \qquad (C.13)$$

126

where

$$\hat{L}_{us} = \frac{1}{k_1} \sinh^{-1}\left(\frac{k_1\sqrt{(k_1^2 + 2\phi_t k_2)}}{k_2 \phi_t} \right).$$ (C.14)

The pressure distributions in the different regions can then be summarized:

$$\hat{p}_{inlet1} = \frac{\tanh(k_1 \hat{L}_1)}{k_1} = \frac{\hat{t}}{\phi_t \sqrt{1 + (k_1 \hat{t} / \phi_t)^2}} \qquad 0 \le \hat{t} \le \hat{t}_s$$

$$\hat{p}_{inlet2} = \frac{\tanh(k_1 \hat{L}_{us})}{k_1} + \hat{L}_s = \frac{\hat{t}_s}{\phi_t \sqrt{1 + (k_1 \hat{t}_s / \phi_t)^2}} + \hat{L}_s \qquad \hat{t}_s \le \hat{t} \le \hat{t}_1$$

(C.15)

where

$$\hat{L}_s = (\hat{t} - \hat{t}_s) / \phi_f.$$ (C.16)

When $\hat{t} \ge \hat{t}_s$, the length of the partially-saturated zone will not change until the flow front reaches the end of the mold. This phenomenon is proven in the Appendix of [31].